Investigation of microcrystalline silicon emitters and DC sputtered ZnO:Al as front contact in silicon heterojunction solar cells

Omid Madani Ghahfarokhi

geboren 17.May 1983

Tehran

Erstgutachter: Prof. Dr. Carsten Agert

Zweitgutachter: Prof. Dr. Jürgen Parisi

weiteres Mitglied: Dr. Lars Korte

Tag der Disputation: 17.04.2014

Abstract

The main focus of this work is to investigate microcrystalline silicon (μc-Si:H) films as a novel emitter layer in combination with DC sputtered aluminum doped zinc oxide (ZnO:Al) as an alternative transparent conductive oxide (TCO) for silicon heterojunction (SHJ) solar cells.

The great advantage of heterojunction solar cells, consisting of single crystal and amorphous silicon, is the higher efficiency in comparison to the traditional diffused solar cells. In the diffused crystalline silicon (c-Si) solar cells, highly recombination-active metal contacts at the surface of cells lead to a medium module efficiency (14-16%). However, c-Si based solar cells have the potential to achieve higher conversion efficiencies. An elegant solution is the heterojunction structure, where a wide band-gap semiconductor is deposited on c-Si, which simultaneously fulfills the passivation and contacting roles. As the lateral conductivity of the silicon thin film layer which forms the emitter in a SHJ solar cell is low, a TCO layer must be deposited to enhance the carrier collection. So far, the most frequently applied TCO for the SHJ structure is indium tin oxide (ITO). However, ITO has several drawbacks such as being toxic, untexturable and expensive.

This study investigates the use of a ZnO:Al layer as an alternative TCO layer for SHJ solar cells. The effect of ZnO:Al deposition parameters on the electrical properties of fabricated SHJ solar cells and an optimum deposition window for each process parameter to satisfy the TCO requirements were addressed. In comparison to ITO, ZnO:Al offers several advantages such as a better texturability, abundance and environmental compatibility. For the successful implementation of the ZnO:Al layer, it is highly important that the Schottky barrier at TCO/emitter to be suppressed due to the low work function of ZnO:Al layer. To satisfy the abovementioned requirements, an μc-Si:H layer was used as emitter material. Moreover, by implementing such a layer, the passivation at the intrinsic amorphous silicon (a-Si:H)/c-Si interface improves. Due to the low absorption coefficient of the μc-Si:H layer, the emitter absorption reduces what leads to a higher J_{SC}. Additionally, by employing a ZnO:Al/Ag/ZnO:Al multilayer structure, the effect of the vertical conductivity component of the ZnO:Al layer on the electrical properties of the fabricated SHJ solar cells and its contribution to the total series resistance was investigated.

Finally, a SHJ solar cell with the conversion efficiency of 19.2% ($V_{OC} = 0.708$ V, FF = 0.791, $J_{SC} = 34.35$ mAcm^{-2}, on flat c-Si substrate) using a μc-Si:H emitter and ZnO:Al as TCO was demonstrated.

Keywords: silicon heterojunction, ZnO:Al, μc-Si:H emitter, Schottky barrier, vertical conduction component, solar cell

Kurzbeschreibung

Der Fokus dieser Arbeit liegt auf der Untersuchung von mikrokristallinen Silizium-Emitterschichten (µc-Si:H) und DC gesputterten transparenten und transparent leitfähigen Oxidschichten (TCO), bestehend aus Aluminium-dotierten Zink-Oxid (ZnO:Al), zur Anwendung in Silizium-Heterostruktur-Solarzellen (SHJ).

In herkömmlichen kristallinen Silizium (c-Si) Solarzellen führt die Kontaktierung der Solarzelle durch Metallkontakte zu hohen Oberflächenrekombinationsverlusten und damit zu moderaten Modulwirkungsgraden. Jedoch haben Solarzellen auf Basis von c-Si das Potential höhere Umwandlung Wirkungsgrade zu erreichen. Eine elegante Lösung zur Effizienzsteigerung ist die Verwendung von Heteroübergängen von Halbleitern mit aufgeweiteter optischer Bandlücke, welche gleichzeitig als Passivierungs- und Kontaktschicht wirken. Weil in SHJ-Solarzellen die laterale Leitfähigkeit des Emitters niedrig ist, sollte die abgeschiedene TCO-Schicht die Sammlung der Ladungsträger verbessern. Das am häufigsten verwendete TCO für SHJ-Strukturen ist Indium-Zinn-Oxid (ITO). Allerdings ist ITO toxisch, nicht strukturierbar und kostenintensiv.

In dieser Arbeit wurde der Einsatz von DC-gesputtertem ZnO:Al als eine alternative TCO-Schicht in SHJ Solarzellen beleuchtet. Der Einfluss von verschiedenen Prozessparametern auf die elektrischen Eigenschaften von ZnO:Al-Schichten und SHJ-Solarzellen wurde untersucht, um optimale Abscheidebedingungen für die SHJ-Solarzelle zu ermitteln. Das ZnO:Al hat mehrere Vorteile im Vergleich zu ITO, wie etwa eine größere Verfügbarkeit, Umweltfreundlichkeit und Strukturierbarkeit. Aufgrund der hohen Austrittsarbeit der ZnO:Al-Schicht ist eine hochleitende Emitterschicht erforderlich, um den Einfluss der Schottky-Barriere zu minimieren. Zur Erfüllung der zuvor genannten Eigenschaften wurde als Ersatz für eine dotierte amorphe Silizium-Emitterschicht (a-Si:H) eine hochleitfähige µc-Si:H Emitterschicht entwickelt und untersucht. Unter Verwendung der µc-Si:H Emitterschicht konnte die Passivierung der c-Si Oberfläche durch die intrinsische a-Si:H Schicht verbessert werden. Aufgrund des niedrigeren Absorptionskoeffizienten von µc-Si:H im, Vergleich zu a-Si:H erhöht sich auch die Absorption in der Solarzellenbasis. Zudem weist der µc-Si:H/ZnO:Al-Übergang, im Vergleich zum a-Si:H/ZnO:Al-Übergang eine geringere Schottky Barriere auf, was zu erhöhten Füllfaktoren führt. Darüber hinaus wurden TCO/Metall/TCO-Mehrfachschichten hergestellt, um den Effekt der vertikalen Leitfähigkeitskomponente der ZnO:Al-Schichten sowie ihren Beitrag zum Serienwiderstand auf hergestellten SHJ-Solarzellen zu untersuchen.

Schließlich konnten SHJ Solarzellen mit einem Wirkungsgrad von 19,2 % ($V_{OC} = 0.708$ V, FF = 0.791, $J_{SC} = 34.35$ mA/cm^{-2}) auf flachen c-Si Wafern mit einer ZnO:Al-TCO-Schicht hergestellt werden.

Stichworte: Silizium-Heterostruktur, ZnO:Al, µc-Si-Emitter, Schottky-Barriere, vertikale Leitfähigkeit, Serienwiderstand, Solarzelle

Table of Contents

Chapter 1

1 Introduction

The conversion of solar light energy into electricity, photovoltaics effect, was discovered by A. E. Becquerel in 1839 [1]. Several years later, the first conversion efficiency of 6% was achieved by Chapin *et al.* at the Bell laboratories in 1954 [2]. Since that time, solar cell devices have gained considerable interest for the space application purpose. In 1970's, the increase in fossil fuel price drew significant attention to the solar energy again as a complementary source of energy. Since then, solar energy has gradually found its share in the energy basket of various countries around the world.

1.1 Motivation and objective

Around 90% of the photovoltaics (PV) market is dominated by wafer-based silicon solar cells. The main reason is the abundance of silicon material and its well-established technology. Figure 1.1(a) and (b) show the schematic illustration of a traditional diffused solar cell and its band diagram respectively. In fact, the presence of metal contacts on the surface of crystalline Si (c-Si) is the main efficiency-limiting factor for traditional diffused solar cells since the metal/semiconductor junction acts as highly recombination-active center. Despite the considerable energy required for the fabrication of these traditional diffused solar cells, the obtained efficiency is still rather low (~15-17%).
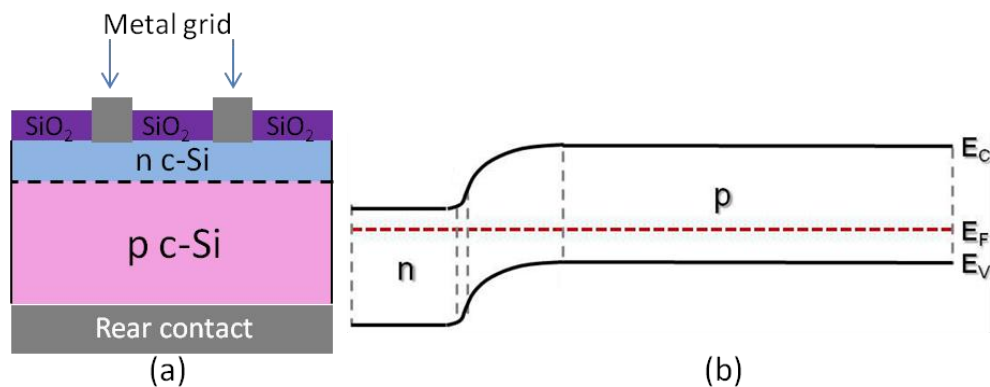

Figure 1.1 *Schematic illustration of (a) a traditional diffused solar cell (b) band diagram of the p-n junction of a traditional diffused solar cell.*

An elegant solution for the abovementioned issue is obtained by fabricating semiconducting heterostructure devices, where the passivation layer simultaneously fulfills

both, the passivation and contact roles. The schematic illustration of a silicon hetrojunction (SHJ) solar cell and its band diagram are shown in figure 1.2(a) and (b) respectively.
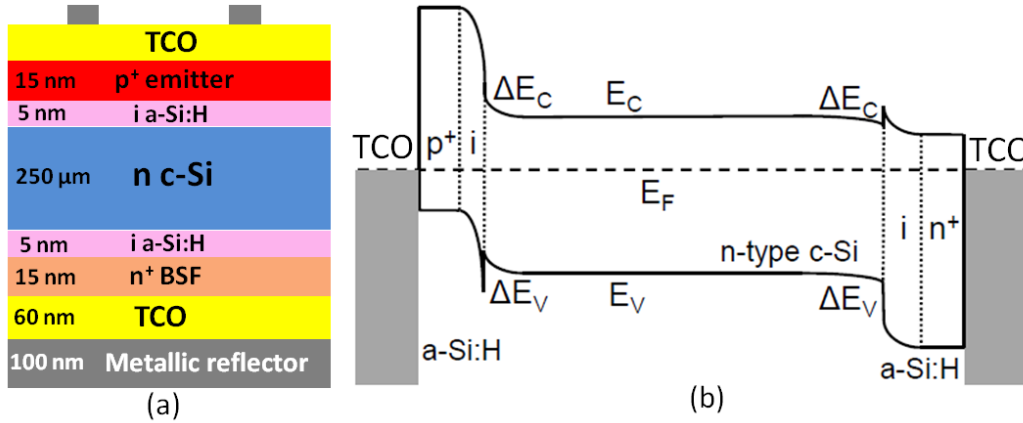

Figure 1.2 *Schematic illustration of (a) SHJ solar cell and (b) the band diagram of a SHJ solar cell.*

The key point of heterojunction structure is to displace highly recombination-active contacts from the silicon surface by the inserting a wide bandgap (E_g) semiconductor layer. In order to increase the efficiency, the interface defect density needs to be as low as possible. The hydrogenated amorphous silicon (a-Si:H) is a good candidate, as its E_g is higher than c-Si and can also reduce the c-Si surface state density by hydrogenation. Moreover, a-Si:H layer can easily be doped (either p- or n-type) by using the low temperature fabrication techniques such as the plasma enhanced chemical vapor deposition (PECVD) technique.

In 1990, the Company Sanyo started to research the Si heterojunction field. The company launched mass production of the so-called "Heterojunction with Intrinsic Thin-layer" (HIT) solar cells in 1997 [3,4]. As the electronic passivation of the doped a-Si:H films is inferior compared to the intrinsic counterpart [5,6], Sanyo inserted a few nanometers of an intrinsic a-Si:H layer between the c-Si absorber and the doped layer [4]. Thanks to the excellent surface passivation achieved by the HIT structure, Sanyo could demonstrate an outstanding conversion efficiency of 19% on the cell and 17% on the module level in production on 100.5 cm^2 substrate [7]. Also, a record open circuit voltage (V_{OC}) as high as 750 mV on the silicon substrate with energy conversion efficiency of 24.7% was reported [8]. Such a high V_{OC} values are virtually out of reach for the standard c-Si solar cell processing since the passivation layer (deposited on top of the diffused emitter) has to be locally opened. Theoretical simulation has demonstrated that a conversion efficiency of 27% could be achieved [9].

SHJ solar cells offer several other technological advantages, compared to the diffused counterpart. Among these advantages, one is the low temperature fabrication process which could reduce the production costs and also allows to use very thin wafers (~90 μm thickness) without any warping issues. From the technological point of view, employing thinner wafers allows higher V_{OC} values, as thinner wafers have a lower bulk defect density [7]. Moreover, the SHJ solar cell has a lower temperature coefficient compared to the diffused solar cells which makes the HIT solar cell modules suitable for tropical regions [10].

However, the main drawback of the SHJ solar cell is the need to deposit transparent conductive oxide (TCO) layers for carrier collection. As the lateral conductivity of doped a-

Si:H layer which forms the emitter of SHJ solar cell is poor, TCO layers must be inserted on top of the emitter layer for transporting the charge carriers to the device terminals. Moreover, the TCO layer acts as an antireflection coating by refractive index matching between air and Si absorber. So far, the mostly applied TCO material for SHJ solar cells is indium tin oxide (ITO). Nevertheless, ITO has some disadvantages. First of all, the costs of ITO are very high compared to other TCO materials, replacing it by a cheaper TCO is one of the ways to reduce the production cost of SHJ solar cells. The second issue is the scarcity of indium (In) which could increase its price even more in future with growing demand [11]. Another issue is the toxicity of indium which mostly causes ITO to be a toxic compound as well [12]. Therefore, replacing ITO with a cheaper, more abundant and environmental-friendly material with texturing capability seems to be a promising approach to further improve the efficiency and reduce the costs of future SHJ solar cells.

In this thesis, we investigate direct current (DC) sputtered aluminum doped zinc oxide (ZnO:Al) material as an alternative TCO material for the SHJ solar cell structure. The ZnO:Al has several advantages such as being an abundant and environmental-friendly material with texturing capability. For a successful implementation, understanding the correlation between the process parameters and opto-electrical properties of the obtained ZnO:Al layers and properties of the obtained SHJ solar cells (using ZnO:Al layer) is necessary and is addressed in this study. Apart from the requirement satisfied by ZnO:Al layer, the properties of the TCO/emitter interface play a significant role in the performance of the obtained SHJ solar cells. In this regard, we study microcrystalline silicon (μc-Si:H) films as an emitter layer for the SHJ solar cell geometry. This thesis addressed several advantages of this emitter layer as well.

1.2 Structure of the document

This thesis is divided into six chapters. Chapter 1 presents the motivation and objective of the thesis. Chapter 2 explains all the characterization tools and measurement techniques used in this study. Also, all experimental details of the fabrication process of the SHJ solar cells are presented. The advanced reader may skip chapter 2 and refer, if needed.

Chapter 3 reviews various ways of surface passivation including chemical and field-effect passivation. The chapter provides further explanation of the correlation between the PECVD process parameters and the obtained a-Si:H passivation properties. To get insight into the a-Si:H passivation mechanism, the recombination process is modeled and compared with the obtained experimental results.

The first section of chapter 4 explains various emitter roles in the SHJ solar cell structure. Moreover, effect of the emitter conductivity on the electrical properties of the obtained SHJ solar cells is studied. In addition, the use of the μc-Si:H layer (as an emitter layer) is introduced and its advantages are addressed.

Chapter 5 addresses the effect of sputtering process parameters on the opto-electrical properties of the obtained ZnO:Al films as well as the properties of fabricated SHJ solar cells.

In addition, the effect of the vertical conductivity component of ZnO:Al layers on the FF and total series resistance is presented.

Finally, the main findings of this thesis together with an outlook are shortly summarized in chapter 6.

1.3 Contribution of this work to the research field

During the last decades, a significant progress has been made in the field of the SHJ solar cells. In fact, the SHJ solar cells have proven to be the most promising Si-based type of solar cells for the future. However, there is still plenty of room left to further improve their performance.

This thesis aims to advance the developed SHJ solar cells one step further by studying a new emitter and TCO. The thesis mainly focuses on investigating μc-Si:H emitter and ZnO:Al as a front contact in SHJ solar cells. The novelties and significances of this PhD thesis are listed as follows:

- The ZnO:Al is introduced, as an alternative transparent conductive oxide for SHJ solar cell geometry. The correlation between DC sputtered ZnO:Al process parameters and the properties of fabricated SHJ solar cell is addressed. The optimum window for each sputtering process parameter including O_2 partial pressure, power density, deposition time and deposition temperature is presented.
- The texturing capability of the ZnO:Al for additional light confinement in the SHJ is discussed.
- The effect of emitter conductivity on the electrical properties of obtained SHJ solar cells is investigated with our novel approach. In our approach, we have varied the emitter conductivity by taking advantage of an improved conductivity resulting from the crystallinity evolution within the μc-Si:H film thickness.
- The μc-Si:H layers are introduced as a novel emitter layer for achieving higher conductivities. Several advantages of this emitter layers, such as a suppressed Schottky barrier at the TCO/emitter interface, reduced emitter absorption and an enhanced a-Si:H/c-Si interface passivation, are addressed.
- The effect of pressure on the nucleation of the μc-Si:H layers is investigated, indicating faster nucleation at a low pressure deposition. In addition, we demonstrate that at low pressures, the passivation degradation by ion bombardment is reversible and hence can be used for the emitter deposition.
- An approach to separate the vertical from the lateral conduction component of the TCO layers is presented, for the first time. Also, the effect of vertical conductivity component of the ZnO:Al layers on the electrical properties of obtained SHJ solar cells and its contribution to the total series resistance is studied.

- By utilizing both, the µc-Si:H emitter and the ZnO:Al TCO, we demonstrate an a-Si:H/c-Si solar cell with the following electrical properties on a flat c-Si substrate: Efficiency = 19.2%, $V_{OC} = 0.708$ V, FF = 0.791, $J_{SC} = 34.35$ mAcm^{-2}.

Chapter 2

2 Experimental details & theory

This chapter presents the basics of all methods (used in this thesis) including fabrication, simulation and various measurement techniques such as optical and electrical characterization. This chapter presents the principles of the different characterization techniques used in this study in order to assist readers to comprehend the discussions in the following chapters.

Section 2.1 reviews all measurement technique including electrical, optical and compositional of the individual developed layers and also the fabricated SHJ solar cells. Section 2.2, first, addresses the need for the passivation of the c-Si wafer-based solar cells. Secondly, various passivation approaches are introduced including the field effect passivation and the chemical passivation of the interface. Afterwards, the concept of recombination model, which is used to simulate recombination at the a-Si:H/c-Si interface, is presented. Section 2.3 studies the fabrication process flow, starting with the Si wafer cleaning until the final fabrication step.

2.1 Measurement techniques

The SHJ solar cells studied in this thesis consist of several layers such as thin-film Si passivation layers, emitter and back surface field (BSF) layersas well as ZnO:Al TCO layers, as shown in figure 1.2(a). To individually characterize these layers, such as measuring the deposition rate, they were firstly deposited on a glass substrate (Corning Eagle XG). On the one hand, this offers simpler processing and sample handling and on the other hand, not all electronic and optical measurements can be done on the c-Si wafers because the substrate could mask the signals generated from these thin layers.

2.1.1 Film thickness

The layer thickness is measured by using an alpha-step profiler (Veeco Dektak 150) allowing to measure a thickness as thin as 2 nm. But for the thin layers, it is mandatory to have a sharp edge. To create such a sharp edge on a glass or on flat c-Si, using a marker is a fast method. The substrate is marked with a marker before layer deposition. After that the marked areas together with the deposited layer on top of that are removed with an acetone solution and as a result sharp edge is obtained. By measuring the substrate at different positions, information about the homogeneity of plasma and conformal deposition can be

obtained. The growth rate of a deposited layer is determined by dividing the measured thickness by the deposition time. Moreover, by comparing the deposition rate over time, the stability of system can be estimated. For more accurate thickness measurement (which is time consuming), Ellipsometry can be used [13]. In this study, we also evaluated the thickness of passivation layer with Ellipsometry (SENTECH SE850-ST), from time to time.

2.1.2 Optical measurements: transmission, reflection and absorption of the thin films

The total wavelength (λ, nm) dependency of transmission (T, %) and reflection (R, %) was measured by using a double UV-VIS-NIR photospectrometer (VARIAN CARY 5000) with an integrating sphere. Layers deposited on glass were measured with the layer surface facing towards the incoming light beam. The absorption (A, %) is then calculated via equation 2.1.

$$A\,(\lambda) = 1 - (T(\lambda) + R(\lambda)) \tag{2.1}$$

Figure 2.1 shows such measured optical transmission, reflection and calculated absorption of 85 nm ZnO:Al layer deposited on glass.
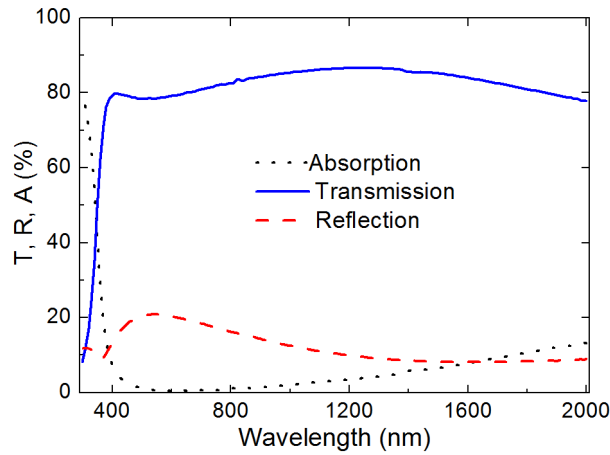
Figure 2.1 *measured transmission (T), reflection (R) and calculated absorption (A) ZnO:Al deposited on glass and measured from the layer side.*

The absorption coefficient α (cm^{-1}) as a function of wavelength for large values of α can be determined by transmission and reflection measurement for a known thickness via equation 2.2:

$$I(x) = I_0 e^{-\alpha x} \rightarrow T = (1 - R)e^{-\alpha x} \tag{2.2}$$

Where x is the distance from the incident surface, I_0 (mWcm^{-2}) is the light intensity at the surface. The sub-bandgap absorption can be determined by other techniques such as photothermal deflection spectroscopy (PDS) [14] or by the constant photocurrent method (CPM) [15]. Figure 2.2 summarizes the wavelength dependent absorption coefficients of a-Si:H, μc-Si:H and c-Si. Therefore, the light penetration depth is therefore the inverse of the absorption coefficient (α), and is plotted on the right-hand ordinate of figure 2.2.
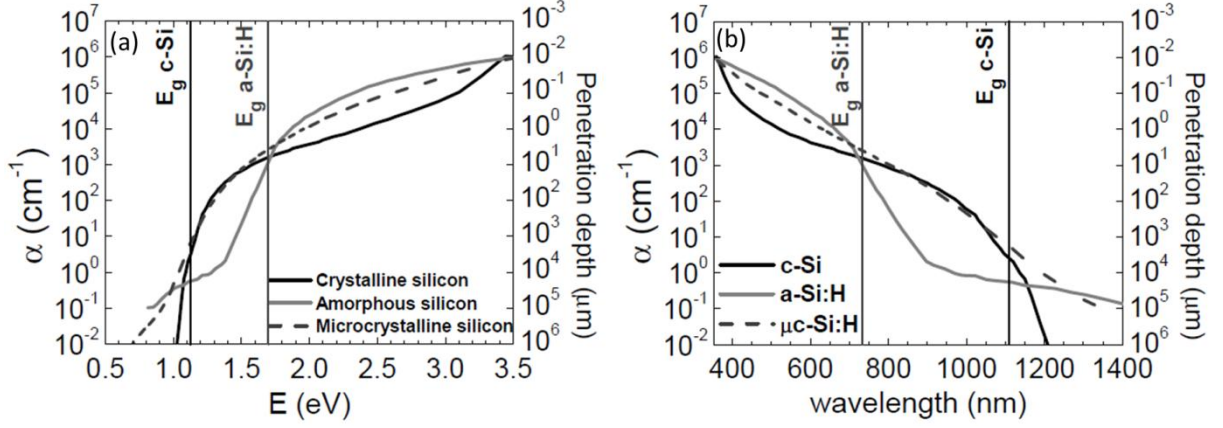
Figure 2.2 *Absorption coefficient of amorphous, microcrystalline and crystalline silicon as a function of a) the photon energy and b) the wavelength [16]. The right axis shows the penetration depth of light in the different Si-materials. The E_g of c-Si and a-Si:H is indicated by the solid vertical line. Microcrystalline silicon has a lower absorption coefficient than the amorphous counterpart.*

2.1.3 Electrical conductivity

The coplanar conductivity of ZnO:Al layers is measured by a four point probe setup (Jandel RM3-AR). The four probes are arranged in a line, the current passes through the two outer probes and the two inter probes measuring the drop voltage. The sheet resistance is obtained by drop voltage over passing through current.

For measuring the conductivity of Si thin-films, ohmic contacts, consisting of 200 nm silver, are sputtered afterwards the conductivity is measured under dark condition. The dark-conductivity activation energy E_{act} (eV), which is the energy difference between the Fermi level and the current transporting energy band (valence band for p-type and conduction band for n-type semiconductor), can be calculated with the following equation:

$$\sigma(T) = \sigma_0 e^{\frac{-E_{act}}{kT}} \tag{2.3}$$

Where the σ (Scm^{-1}) is the dark conductivity, T is the temperature and k is the Boltzmann constant. The plot $ln\sigma(T)$ vs. $\frac{1}{T}$ is used to extract E_{act}.

2.1.4 Film crystallinity

The µc-Si:H is composed of conglomerates of crystalline grains embedded in a a-Si:H tissue [17,18]. To get an insight into the crystallinity fraction of µc-Si:H, we have characterized Si thin-film layers with micro-Raman spectroscopy. It should be highlighted that the calculated Raman fraction is different from the crystalline volume fraction and is a representative of the crystalline volume fraction [19]. In micro-Raman spectroscopy, monochromatic light is focused on the layer through a conventional microscope. The microscope also collects the backscattered light. Most of the scattered photons have the same energy as the incident light (same wavelength as source laser), elastic scattering. But a very small fraction of scattered photons (~1×10^{-6}) interacts inelastically with vibrational modes and

thus loses or gains energy [20]. The frequency shift observed in Raman depends on the characteristic of material. For the characterization, we use a laser excitation light with wavelength of 488 nm and a Bruker SENTERRA Raman microscope.
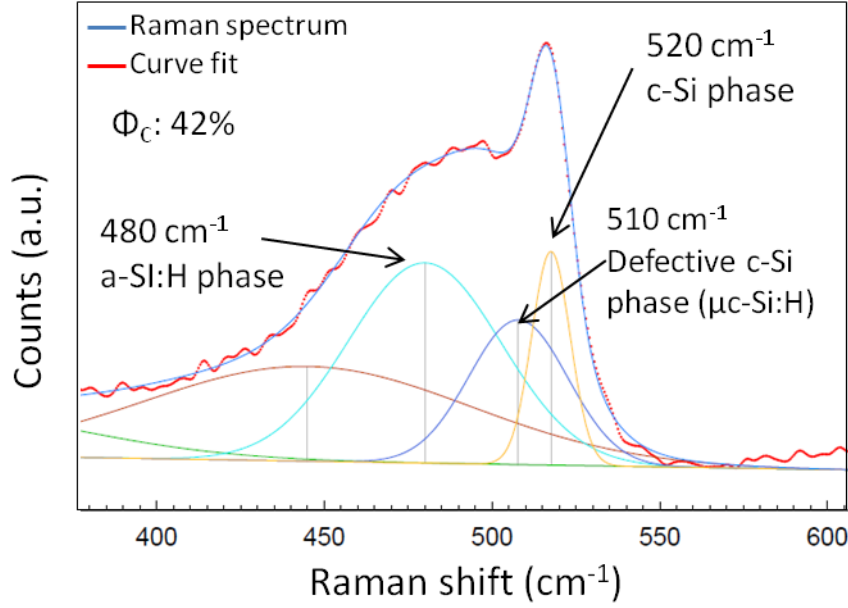
Figure 2.3 *Evaluation of the Raman crystalline fraction of a Si thin-film layer (5 nm i a-Si:H + 18 nm μc-Si:H) by deconvolution of the Raman spectrum into Gaussian peaks, a-Si:H (480 cm^{-1}), μc-Si:H (510 cm^{-1}) and c-Si (520 cm^{-1}).*

Figure 2.3 shows the Raman spectrum of 5 nm i a-Si:H together with an 18 nm p μc-Si:H deposited on glass. The Raman spectrum can be deconvoluted into Gaussian peaks in which the area of each Gaussian curve is proportional to the corresponding phase concentrations as the follows: the peak at 480 cm^{-1} is the characteristic of the transverse optical (TO) mode of a-Si:H, the peak centered at ~510 cm^{-1} is attributed to the defective part of the crystalline phase such as the nano-crystalline phase and the peak located at 520 cm^{-1} is related to the TO mode in c-Si. The Raman crystallinity fraction is defined as the ratio of sum of the area correspondent to the crystalline parts over the area of silicon related peaks (equation 2.4):

$$\Phi_C = \frac{I_{520} + I_{510}}{I_{520} + I_{510} + I_{480}} \tag{2.4}$$

As mentioned above, the calculated crystallinity fraction via equation 2.4 is not the actual crystalline volume fraction. When using blue laser excitation light (488 nm wavelength), the crystallinity of layers, with a thickness as thin as 10 nm, can be evaluated due to the blue light's high absorption coefficient in both: a-Si:H and μc-si:H. The penetration depth at 488 nm is ~45 nm for a-Si:H and 90-150 nm for μc-Si:H as described in figure 2.2(b).

2.1.5 Current-voltage characteristics

To evaluate the maximum output power, the current-voltage characteristics (J-V curve) of solar cell are measured under standard test condition. The standard test condition consists of a light intensity of 1000 W/m^2 under a light spectrum which is called AM1.5G and 25°C

temperature. In this study, for performing a J-V measurement, we used a class AAA dual lamp sun simulator (WACOM).

Figure 2.4 shows a typical J-V curve characteristic of a SHJ solar cell indicating the parameters that can be determined by this measurement.
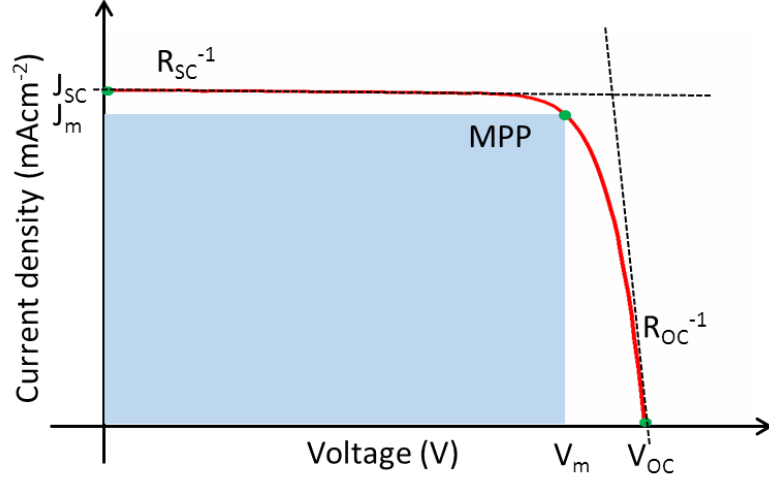
Figure 2.4 *Typical current-voltage curve a of SHJ solar cell. V_{OC}, J_{SC} and MPP are indicated on the figure.*

The open-circuit voltage (V_{OC}) and short-circuit current density (J_{SC}) are the maximum voltage and current a solar cell provides. The V_m and J_m represent the voltage and the current density where the output power is at maximum, referred to as the maximum power point (MPP). The fill factor is defined as a ratio of this actual maximum obtainable power to the theoretical (not actually obtainable) power, as follows:

$$FF = \frac{V_m \times J_m}{V_{OC} \times J_{SC}} \tag{2.5}$$

The efficiency is the maximum fraction of the incident sunlight ($I_L = 1000 \ Wm^{-2}$) that is converted to electrical power ($P_m \ mWcm^{-2}$) by a solar cell:

$$\eta = \frac{P_m}{I_L} = \frac{FF \times V_{OC} \times J_{SC}}{I_L} \tag{2.6}$$

The slope of the JV-characteristic at the V_{OC} and J_{SC} points is given by $R_{OC} = (\frac{\partial J}{\partial V})^{-1}_{J=0}$ ($m\Omega cm^{-2}$) and $R_{SC} = (\frac{\partial J}{\partial V})^{-1}_{V=0}$ ($m\Omega cm^{-2}$). In a first approximation, they are close to the values of the series resistance (R_S) and the parallel resistance R_P. The precise values of R_S and R_P are obtained at high illumination (10 suns) and low illumination (0.04 suns), respectively.

2.1.6 Suns V_{OC} measurement

The Suns-V_{OC} set-up (Sinton WCT 120) measures the solar cell Voc as a function of the light intensity that is monitored by a photodiode (see figure 2.5(a)). An implied terminal current (J_{impl} ($mAcm^{-2}$)) is determined for each V_{OC} from the normalized light intensity (I_L/I_L (1 sun)) and from the provided J_{SC} (triangle data points Figure 2.5(b)). The incident light

intensity that penetrates the sample is assumed to be proportional to the luminous intensity under these considerations:

$$J_{impl}(V_{OC}) = J_{sc}(1 - \frac{I_L(V_{OC})}{I_L(1\ sun)})$$

(2.7)

This way the series resistance (R_S) has no effect on the J-V curve since no current is drawn from the solar cell. In other words, the J-V curve can be obtained without the effect of series resistance. The calculated pseudo fill factor (PFF) (which is the fill factor without the effect of series resistance) of this J-V curve indicates how the real FF has been affected by series resistance.
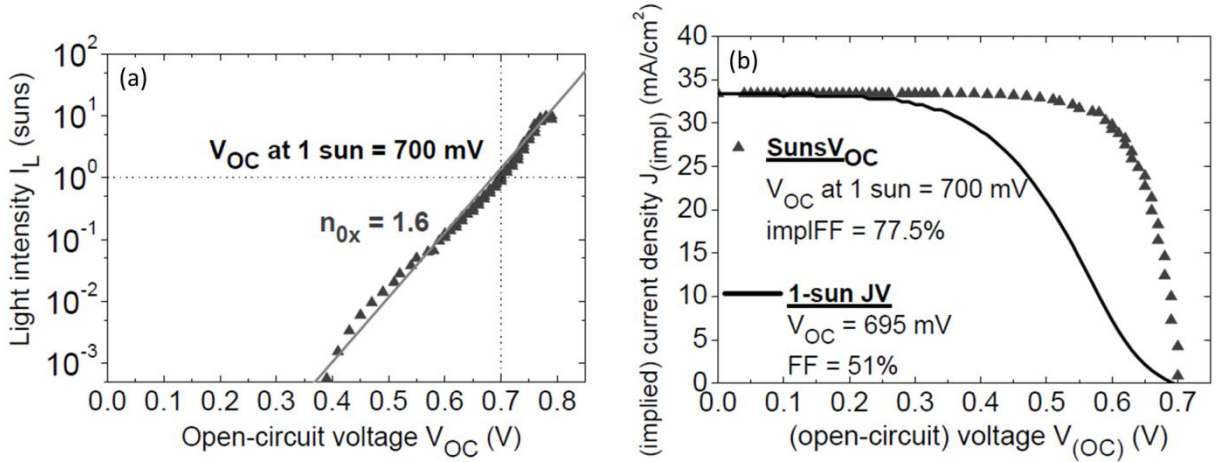
Figure 2.5 *(a) Suns-V_{OC} measurement and (b) implied JV-curve calculated from Suns-V_{OC} in (a) (triangles) compared to the actual JV-curve of the solar cell measured under 1 sun (line) [69].*

2.1.7 External and internal quantum efficiency

The external quantum efficiency (EQE) measurement shows the percentage of the incident photons that has been converted to electron-hole pairs and has been collected at the contacts. In other words, EQE shows the efficiency of a solar cell at each wavelength to produce electrical current. Figure 2.6 shows a typical EQE curve of a SHJ solar cell with 80 nm ZnO:Al. In this work, EQE measurements are performed between 380 and 1100 nm are performed (measured at 0 V except when stated otherwise). By extracting the cell reflection from the EQE curve, the internal quantum efficiency is obtained which indicates the probability of a photon to yield an electron in the external circuit.
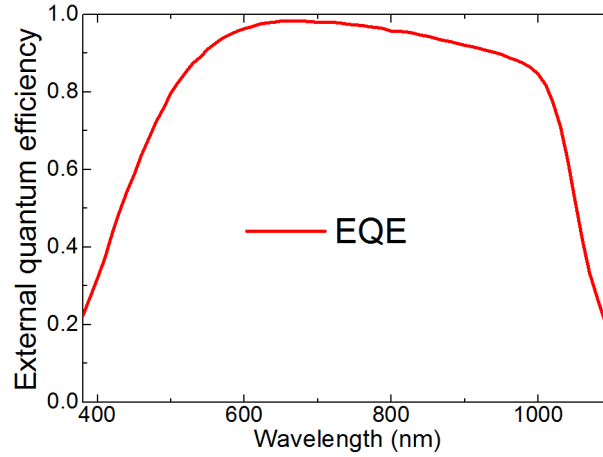
Figure2.6 *External quantum efficiency (EQE) measurement of a SHJ solar cell with 80 nm ZnO:Al*

Apart from the J-V measurement (the exact cell area is necessary to be known to obtain J_{SC}), the short-circuit current density (J_{SC}) could also be obtained by a given quantum efficiency (QE) curve via:

$$J_{SC} = q \int_0^\infty \Phi_{AM1.5G} (\lambda) QE(\lambda) d\lambda \qquad (2.8)$$

where $\Phi_{AM1.5G} (\lambda)$ cm^{-2}s^{-1} is the photon flux related to the spectral AM1.5G and q is the electron charge. The advantage of obtaining short-circuit current by QE is that the exact cell area is not necessary to be known.

The EQE can also be defined as the product of internal quantum efficiency (IQE) and optical losses due to the solar cell's total external reflection (R_{cell}), as shown in equation 2.9:

$$EQE = IQE \ (100 - R_{cell})/100 \qquad (2.9)$$

Thus, the IQE gives the probability of a photon to enter the solar cell and to yield an electron in the external solar cell current circuit. As the front surface reflection is abstracted in the IQE curve, IQEs of the solar cells can be used as an example for comparing a flat and a textured solar cell consisting of the same layers. Parasitic absorption in the TCO, emitter layer and the back contact are still contained in IQE.

2.2 The c-Si passivation by a-Si:H

The c-Si bulk material is a well-ordered semiconductor with a diamond crystal structure, containing 8 atoms of silicon per unit cell. Figure 2.7(a) and (b) show the unit cell of the diamond crystal structure and an arrangement of the silicon atoms in a unit cell respectively. Unlike the well-arranged atoms in c-Si bulk material, the surface contains broken bonds (broken covalent *sp³* hybrid bonds), so-called dangling bonds (DB). The DB density depends on the crystal surface orientation [21]. For the c-Si wafer-based solar cells, the most common surface orientations are Si(100) for flat wafers and Si(111) which appears after alkaline solution texturing of the (100)-type surfaces. The number of broken bonds per atom is two for Si(100) and one for Si(111) surface orientation [22].

These DBs introduce some energy levels in the E_g and hence cause the carriers to recombine. In order to minimize the surface recombination, it is of great importance to properly passivate the surface of a Si wafer. Such carrier recombination takes place in many optoelectronic semiconductor devices such as light emitting diodes (LEDs) [23], lasers [24], photodiodes [25], photovoltaic devices [26], as well as Si-based solar cells. [27-29]. Therefore, passivation of the semiconductor interfaces is of extreme importance for improving the device performance.
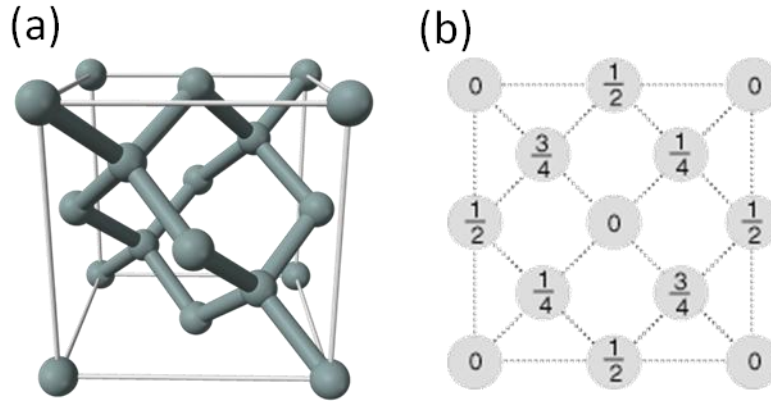
Figure 2.7: *(a)The unit cell of silicon (diamond cubic crystal structure) (b) the arrangement of the silicon atoms in a unit cell, with the numbers indicating the height of the atom (from top view) as a fraction of the cell dimension [30].*

A variety of semiconductor passivation layers is available. Most of them have been historically developed for microelectronics. Among them, the most known passivation layer for the c-Si is thermally grown silicon-dioxide (SiO_2) which has been developed as a gate oxide for the metal-oxide-semiconductor field-effect transistor (MOSFET) [31]. By employing such an optimum passivation layer, the highest ever reached conversion efficiency of 25% for the c-Si wafer-based solar cells has been achieved [32,33] under standard test conditions: air mass 1.5 global (AM 1.5 G), 25°C. Efficient Si-based light emitting devices are another example of good passivation of thermally grown SiO_2 layers [34]. However, the requirement for thinner passivation layers and more importantly the costs of high temperature processing [35] requires alternative passivation layers.

Wet-thermal oxides grown at low temperatures [36], amorphous silicon-nitride (a-SiN_x:H) [37], SiO_2/a-SiN_x:H stacks [38] and aluminum-oxide (Al_2O_3) layers [39,40] were introduced as replacement for the thermally grown SiO_2 layers. However, the main issue for these passivation layers is that, since these passivation layers are not conductive, one needs to pattern some openings on the passivation layer surface to locally contact the metal grids to the absorber (in the traditional c-Si-based solar cells). Moreover, the presence of the highly recombination-active metal contacts is an important loss channel for such dielectrically passivated solar cells (see figure 1.1(a)).

A solution for separating the recombination-active metal contacts from the c-Si surface are semiconducting heterostructure contacts (see figure 1.2(a)). In principal, such a structure can be fabricated by insertion of wide E_g semiconducting layer which simultaneously fulfills both the passivation and the contact roles.

The a-Si:H film appears to be a good candidate to fulfill the abovementioned requirements, as it has a wider Eg (~1.7 eV) than the c-Si (1.1 eV) and also can effectively passivate the surface by hydrogenation [41]. In addition, the a-Si:H film can be fabricated at a relatively low temperature (~200°C) by the PECVD technique which is another advantage of this material. Moreover, the a-Si:H film can easily be doped to form the required n- and p-type semiconductors [42].

2.2.1 Passivation mechanisms

In a recombination (carrier generation) process, electron-hole pairs are eliminated (produced). For the recombination process, two factors are essential: (i) the presence of both electron and hole, (ii) the existence of an energy level where the electron and the hole can get together. Hence, to suppress the surface recombination, two fundamental approaches can be taken: (i) reduction of the surface density of one carrier type i.e. repelling either electrons or holes from the surface. As the recombination process involves one electron and one hole, the recombination is highest when the surface electron and the hole densities are equal. As electrons and holes carry electrical charges, the formation of an internal electrical field, below the semiconductor surface, reduces the surface density of one charge carrier type. This approach is called field effect passivation. The schematic illustration of field effect passivation is shown by Figure 2.8(b). (ii) The second approach is to reduce the density of surface states by chemical passivation which suppresses the recombination. Figure 2.8(c) shows the schematic illustration of the surface chemical passivation.
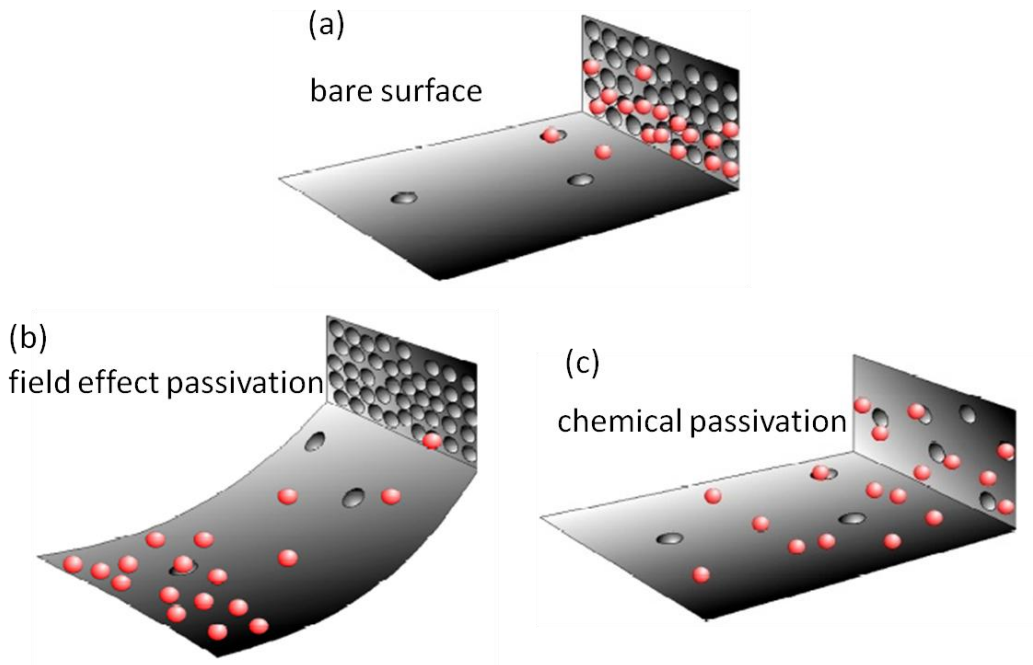

Figure 2.8: *The schematic illustration of (a) a bare surface (b) field effect passivation by repelling one of the carrier types by an electric field and (c) the chemical passivation of the surface states (reduction of surface state density), [Courtesy of S. De Wolf].*

2.2.2 Passivation evaluation, Sinton lifetime tester

Photogenerated carriers in c-Si absorber recombine in the c-Si bulk as well as at the c-Si surfaces. Assuming a high-quality c-Si wafer like float zone (FZ) grown wafers, the main recombination channels are the surfaces which form interfaces with a-Si:H. To determine the minority carrier lifetime, several techniques, such as infrared (IR) transmission or emission [43], photoluminescence (PL) [44], eddy-current [45] and photoconductance (PC) [46], have been developed. Among them, the PC technique, measured by an induction coil, developed by Sinton Instruments, is the most widely used, since it is contactless, fast and the obtained results are of low uncertainty [46]. Moreover, the measurement is sensitive and a bulk defect density as low as 10^9-10^{11}cm^{-3} in a straightforward measurement can be detected [47]. In this study, for evaluating the electronic properties of silicon wafers and their surfaces, the photoconductance decay (PCD) was used extensively (Sinton WCT-120).

In the experimental setup of photoconductance decay, the excess charge carriers are generated with a flash lamp. A filter which cuts off all wavelengths shorter than 700 nm is mounted to make sure that homogeneous charge is generated throughout the whole wafer bulk. The induced conductivity by photogenerated carriers is given by:

$$\Delta\sigma = q(\Delta n_{av}\mu_n + \Delta p_{av}\mu_p)W \tag{2.10}$$

where $n_{av} = p_{av}$ (cm^{-3}) is the average excess carrier density, W (cm) is the wafer thickness, μ_n, μ_p (cm^{2}V^{-1}s^{-1}) are the electron and hole mobility in c-Si (which are well-known) respectively.

The conductivity change of the wafer is continuously measured by an induction coil and a RF bridge. As shown by Nagel *et al.* [48] the lifetime can be calculated via equation 2.11:

$$\tau_{eff} = \frac{\Delta n}{G - \frac{d\Delta n}{dt}} \tag{2.11}$$

where G is generation rate (cm^{-3}s^{-1}), Δn is the excess carrier density (cm^{-3}) and τ_{eff} is the effective lifetime.

The measurements can be performed in two different modes: Quasi-Steady-State (QSS) or transient. In the QSS mode, the decay of flash light (~2 ms) is at least 10 times slower than the carrier lifetime. Thus, the excess carrier populations are always in steady-state or very close to it. So the lifetime can simply be calculated via:

$$\tau_{eff} = \frac{\Delta n}{G} \tag{2.12}$$

During the measurement a calibrated light sensor (photodetector) measures the light intensity I_L (mW/cm^{-2}) via photon flux density Φ_L (cm^{-2}s^{-1}), [$\Phi_L = \frac{\lambda}{hc}I_L$] and the generation rate G_L (cm^{-3}s^{-1}) can be calculated via:

$$G_L = \Phi_L \frac{F}{W} \tag{2.13}$$

where W is the wafer thickness and F is the optical constant which indicates the fraction of the incident light that is absorbed in c-Si.

In the transient PCD measurement mode, the c-Si conductivity is measured vs. time after an intense light pulse. I.e. in the transient mode, the initial generation is done by a very short and intensive light pulse without generation afterwards. Therefore, the lifetime (equation 2.11) is reduced to equation 2.14:

$$\tau_{eff} = \frac{-\Delta n}{\frac{d\Delta n}{dt}} \tag{2.14}$$

The transient mode is only appropriate for a lifetime longer than the flash duration time (which is ~100 µs). The transient mode has two advantages in comparison to the QSS mode. First, as for the transient mode, the generation rate should not be measured, the optical constant (the parameter that defines the fraction of incident light that is absorbed in the wafer) is not necessary to be defined. Second, there is much less uncertainty in the measured τ_{eff} in the transient mode compared to QSS analyses. I.e. the transient mode is influenced by fewer uncertainties (such as uncertainty in photoconductance calibration constants and coil's output voltage) than QSS analyses [49]. However, the transient measurement has one drawback being it is only valid when the lifetime of photogenrated carriers is significantly higher than the flash duration time (i.e. the lifetime should at least be greater than 100 µs).

It should be mentioned here, that the lifetime which is measured by means of the PC technique is the effective lifetime and we indicate it by the (eff) subscript. There are several sources of recombination in a device such as extrinsic bulk recombination (defects in crystal structure and impurities in the bulk), intrinsic bulk recombination (Auger and radiative recombination) and surface recombination. The τ_{eff} represents the combined impact of all these recombination channels and is defined via equation 2.15:

$$\frac{1}{\tau_{eff}} = \frac{1}{\tau_{bulk}} + \frac{1}{\tau_{surface}} \tag{2.15}$$

In case of the bulk lifetime is high (i.e. the recombination in the bulk could be neglected as an example for float zone (FZ) wafers) and with identical passivation layers on both wafer surfaces, the effective surface recombination velocity (S$_{eff}$), which describes two-directional recombination, can be calculated via equation 2.16:

$$S_{eff} \leq \frac{W}{2\,\tau_{eff}} \tag{2.16}$$

where W is the wafer thickness. We should highlight that the obtained value for S_{eff} by equation 2.16 is overestimated, since it is supposed that all recombination take place at the interface. Moreover, this calculation is not valid at a high excess carrier density where the Auger and radiative recombination in the bulk could be significantly high even for an indirect E_g semiconductor. The advantage of representing S_{eff} rather than τ_{eff} is the easier direct comparison of interface recombination on all sorts of c-Si wafers and passivation material without the effect of wafer thickness and bulk recombination.

The maximum V_{OC} value of a final device is given by splitting of the quasi-Fermi levels. By knowing the excess carrier density with lifetime tester, the implied V_{OC} (impl V_{OC}) can be calculated via equation 2.17:

$$implV_{OC} = \frac{kT}{q} \ln \left(\frac{(n_0 + \Delta n)(p_0 + \Delta p)}{n_i^2} \right) \qquad (2.17)$$

Where n_0 and p_0 are the electron and the hole densities at thermal equilibrium and n_i is the intrinsic carrier density.

2.2.3 a-Si:H/c-Si interface recombination modeling

So far, we have discussed how to evaluate the passivation performance of a-Si:H layers deposited on c-Si wafers. In this section, we introduce the concept of a recombination model developed by Olibet *et al* [50] to simulate recombination at a-Si:H/c-Si interface. Using this model, enabled us to gain insight in the a-Si:H passivation mechanism and to obtain a quantitative value of the interface state density (N_s) of rough c-Si wafers passivated by different a-Si:H layers.

The Schockley-Read-Hall (SRH) recombination model [51] is the most applied model for recombination via defects in a semiconductor material. In this model, a recombination takes place through a discrete energy level which is located in the middle of the E_g. The defective energy level has only two charge states; either capture an electron or a hole. However, in an amorphous semiconductor, such as a-Si:H film, a continuous distribution of energy levels exist within the E_g. Moreover, the dangling bonds, which are the most likely recombination centers, could have three charge states. Depending on the Fermi level position, a dangling bond is occupied with zero, one, or two electrons. According to the number of trapped electrons by a Si$_3$ site, three different states could be defined as follows:

(1) D$^+$, is referred to the state that dangling bond (or Si$_3$ site) has zero electron
(2) D^0, is referred to the state that dangling bond (or Si$_3$ site) has one electron
(3) D$^-$, is referred to the state that dangling bond (or Si$_3$ site) has two electrons

In the SRH recombination model, only one recombination path exists. However, at a-Si:H/c-Si interface, two recombination paths exist due to the amphoteric nature of dangling bounds, as written below.

(1) D^0 + e $\rightarrow$ D$^-$ (capture cross-section σ_n^0) then followed by D$^-$ + h $\rightarrow$ D^0 (capture cross-section σ_p^-)
(2) D^0 + h $\rightarrow$ D$^+$ (capture cross-section σ_p^0) then followed by D$^+$ + e $\rightarrow$ D^0 (capture cross-section σ_n^+)
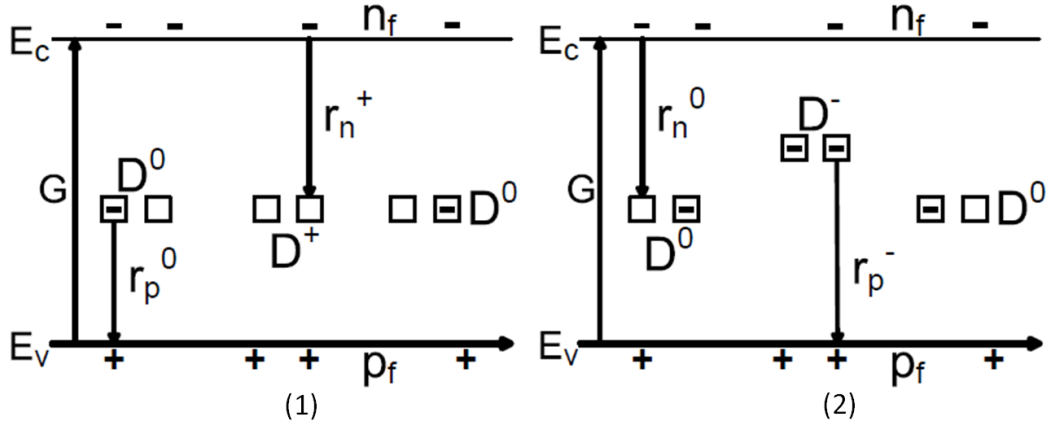
Figure 2.9 *Successive capture events leading to electron-hole recombination through DB. Two recombination paths co-exist: (1) D^0 capturing one hole followed by capturing one electron. (2) D^0 capturing one electron followed by capturing one hole. n_f and p_f are the free carrier densities, D^0, D^+ and D^- are the neutrally, positively, and negatively charged conditions of the DBs. r_p^0, r_n^+, r_n^0 and r_p^- are the corresponding capture rates [50].*

These paths which form by successive capturing of charge carriers are also shown in figure 2.9. Taylor and Simmons extended the SRH recombination model for disordered semiconductor materials where continued distribution of energy levels exist in the E_g [52]. By considering some assumptions, Hubin introduced a closed-form recombination rate which only depends on the total density of dangling bounds (N_{DB}) where the exact shape of the energy states distribution is not required [53]. Based on the Hubin study, Olibet showed that the recombination via dangling bounds in a-Si:H bulk can be used to describe the recombination at the a-Si:H/c-Si interface [50]. The recombination rate at a-Si:H/c-Si interface can be defined via equation 2.18 [50]:

$$R_s = R_{DB}(n_s, p_s) = \frac{n_s \sigma_n^0 + p_s \sigma_p^0}{\frac{p_s \sigma_p^0}{n_s \sigma_n^+} + 1 + \frac{n_s \sigma_n^0}{p_s \sigma_p^-}} v_{th} N_s, \tag{2.18}$$

where v_{th} (cm/s) is the thermal velocity, n_s and p_s are the density of electrons and holes at the interface (cm^{-3}), respectively, N_s (cm^{-2}) is the interface state density, σ_n^0 and σ_p^0 (cm^{-2}) are the capture cross-section of the neutral states. σ_n^+ and σ_p^- (cm^{-2}) are the capture cross-section of the charged states.

The parameters governing the interface recombination (similar to the extended SRH model) are:

- The capture cross-sections σ_n and σ_p which ratio $\frac{\sigma_n}{\sigma_p}$ describes the effectiveness of a recombination center to capture an electron or a hole.
- The total density of the interface recombination centers N_s [cm^{-2}] indicating the quality of the passivation
- The surface charge density Qs, representative of the magnitude of field-effect passivation.

It should be noted that, in the recombination rate equation (equation 2.18), the exact distribution of dangling bond states (i.e. N$_s$ as function of energy (N(E)) is not required. The

shape of the continuous distribution of the dangling bond states results from the knowledge of the product of the capture cross-sections and the interface state density over the whole energy range in the E_g [54-56].

The advantage of this closed-form recombination model is that it allows us to simply distinguish between the two different passivation approaches (section 3.2): either field effect passivation or chemical passivation by the reduction of the interface defect density. So, the major model variables are the interface defect density (N$_s$) and the surface charge density (Q$_s$).

In equation 2.18, the interface carrier density (n_s and p_s) is a function of the surface potential ψ_s (which modifies the band bending at the interface) which should be numerically determined. By considering the passivation layer as a small E_g insulator, and assuming that all the quasi-Fermi-levels are constant from the bulk of c-Si wafer to the interface (figure 2.10), the classical drift-diffusion transport equation can be used to determine the effect of ψ_s on the interface carrier density. Hence, n_s and p_s are defined via equation 2.19 and 2.20:

$$n_s = (n_0 + \Delta n)e^{\frac{+q\psi_s}{kT}} \tag{2.19}$$

$$p_s = (p_0 + \Delta n)e^{\frac{-q\psi_s}{kT}} \tag{2.20}$$

To determine the Q$_s$, the charge neutrality condition in the a-Si:H bulk should be considered, given via equation 2.21,

$$n_f + n_t + \rho_{DB}^- + \rho_A^- + p_f + p_t + \rho_{DB}^+ + \rho_D^+ = 0 \tag{2.21}$$

where the n_f (cm^{-3}) is the free electron density in the conduction band, p_f (cm^{-3}) is the free hole density in the valence band, n_t (cm^{-3}) is the localized electron density in the conduction band-tail, p_t (cm^{-3}) is the localized hole density in the valence band-tail, ρ_A^- (cm^{-3}) is the ionized acceptor density, ρ_D^+ (cm-3) is ionized donor density and ρ_{DB}^- and ρ_{DB}^+ (cm^{-3}) are the negatively and the positively charged dangling bond density, respectively.

The localized charge densities in the band-tails are much higher than the density of photogenerated free carriers ($n_t >> n_f$ and $p_t >> p_f$). Moreover, since our passivation layer is not intentionally doped (intrinsic), the ionized acceptor and donor density (ρ_A^- and ρ_D^+) in equation 2.21 could be neglected. So the total image charge density (Q_{Si}), induced in the c-Si wafer (passivated with intrinsic a-Si:H film), is the sum of the net bulk charged dangling bond density and the density of the localized bulk charge. The Q_{Si} is given by the following equation [57],

$$Q_{Si} = \pm(\frac{2kTn_i\epsilon_0\epsilon_{Si}}{q^2}[e^{+\frac{q(\phi_p-\psi_s)}{kT}} - e^{+\frac{q\phi_p}{kT}} + e^{+\frac{q(\psi_s-\phi_n)}{kT}} - e^{-\frac{q\phi_n}{kT}} + \frac{q\psi_s+(p_0+n_0)}{kTn_i}])^{0.5} \tag{2.22}$$

where n_0 and p_0 are the electron and holes density at equilibrium respectively. T, k, ϵ_0 and ϵ_{Si} are the temperature, Boltzmann constant, permittivity, and relative dielectric constant for silicon respectively. ϕ_n and ϕ_p are the quasi-Fermi-level of electrons and holes at the edge of the space charge region, defined in equations 2.23 and 2.24.

$$\phi_n = -\left(\frac{kT}{q}\right)\ln\frac{n_0+\Delta n}{n_i} \tag{2.23}$$

$$\phi_p = -\left(\frac{kT}{q}\right) ln \frac{p_0+\Delta n}{n_i} \tag{2.24}$$

It should be mentioned that the quasi-Fermi-levels (ϕ_n and ϕ_p) depend on the non-equilibrium density of charge carriers and, therefore, are injection level dependent. As mentioned above, we assumed the passivation layer as a small E_g insulator. Hence, the model does not require to take the band offsets between the a-Si:H and c-Si into account in order to keep the number of parameters as low as possible. However, these band offsets have a significant effect on the function of the SHJ solar cells as demonstrated in several simulation and experimental studies [5,58-60]. For the numerical simulation of the SHJ solar cells, the discontinuities in the conduction and valance bands should be considered for a proper modeling of charge transfer from the c-Si absorber to the passivation layer or vice versa.

Another process which occurs in the photogeneration and recombination at a-Si:H/c-Si interface is the thermal emission phenomena. In the closed-form expression for R_{DB} (equation 2.18), suggested by Hubin [53], the thermal emission from the dangling bonds states are neglected (for high enough generations [52]). However, the thermal emission from the recombination centers, located in the E_g of c-Si, cannot be neglected. Hence, the n_s and p_s have to be modified by ($n_s + n_1$) and ($p_s + p_1$) for the extension of the closed-form bulk recombination of disordered semiconductor expression to the surface recombination at a-Si:H/c-Si interface [50,61]. n_1 and p_1 are the thermally emitted carrier densities from recombination centers within the c-Si E_g. Recombination in the bulk of c-Si is modeled by the SRD theory. Therefore, n_1 and p_1 could be defined via the equations 2.25 and 2.26,

$$n_1 = n_i \, e^{\frac{E_t-E_i}{kT}} \tag{2.25}$$

$$n_1 = n_i \, e^{\frac{E_i-E_t}{kT}} \tag{2.26}$$

where E_t is the energy level of the recombination center, located in the middle of c-Si E_g and exactly at the edge of the space charge region in the c-Si wafer (see figure 2.10).
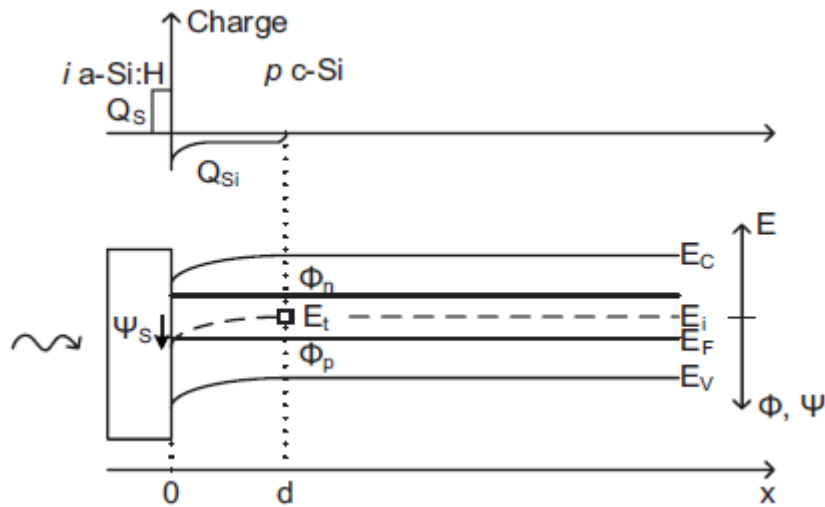

Figure 2.10 *The charge distribution and the band diagram at the p c-Si/i a-Si:H interface under illumination. A unidirectional diffusion current flow from the c-Si into the interface is assumed, affecting the interface DB charge state. The resulting sketch is that of a small E_g insulator [50].*

So far, we have defined the surface recombination through the DBs. The experimentally accessible value (measured by Sinton lifetime tester) is the effective lifetime that is given by bulk and surface recombination (front and back), as shown in equation 2.27.

$$\frac{1}{\tau_{eff}} = \frac{1}{\tau_{bulk}} + \frac{1}{\tau_{surface}}$$

(2.27)

For the float-zone (FZ) wafers, the recombination in the c-Si bulk defects can be neglected [62]. However, in our case (low lifetime CZ wafers), the assumption of the infinite bulk defects lifetime results in a poor fit for the measured injection level dependent lifetime values. Moreover, the bulk lifetime is limited by Auger and radiative recombination at high excess carrier density even for the low bulk defects c-Si wafers. Therefore, for a more accurate fit, these parameters should be considered. In equation 2.27, the bulk lifetime τ_{bulk} could be expressed by the extrinsic and intrinsic lifetimes. Hence, equation 2.27 can be rewritten as:

$$\frac{1}{\tau_{eff}} = \frac{1}{\tau_{bulk}} + \frac{1}{\tau_{surface}} = \frac{1}{\tau_{extrinsic}} + \frac{1}{\tau_{intrinsic}} + \frac{1}{\tau_{surface}}$$

(2.28)

The intrinsic recombination processes for an indirect Eg semiconductor are Auger τ_{Auger} and radiative recombination $\tau_{Radiative}$. Therefore, equation 2.28 can be written as following,

$$\frac{1}{\tau_{eff}} = \frac{1}{\tau_{Defect}} + \frac{1}{\tau_{Auger}} + \frac{1}{\tau_{Radiative}} + \frac{1}{\tau_{Surface}}$$

(2.29)

The surface lifetime $\tau_{surface}$ is related to the surface recombination rate R_{DB} (cm^{-2}s^{-1}),

$$\tau_{surface} = \frac{\Delta n_s}{R_{DB}}$$

(2.30)

where Δn_s is the excess carrier density at the interface. So by replacing equation 2.30 by equation 2.29, we can rewrite τ_{eff} , as shown in equation 2.31.

$$\frac{1}{\tau_{eff}} = \frac{1}{\tau_{Defect}} + \frac{1}{\tau_{Auger}} + \frac{1}{\tau_{Radiative}} + \frac{R_{DB}}{\Delta n_s}$$

(2.31)

In the Auger recombination process, an electron recombines with a hole and the released energy is transferred to another hole or electron. Thus, the Auger recombination involves three charge carriers. Higher c-Si wafer doping (higher generated excess carrier density) results in higher Auger recombination rate. In a high quality c-Si wafer with an excellent surface passivation, the Auger recombination becomes the dominant recombination process at high excess carrier density.

In our modeling, we used the Auger recombination rate suggested by Kerr and Cuevas [63] as it is valid for a variety of experimental results. Thus, τ_{Auger} (s) in equation 2.31 can be replaced by equation 2.32,

$$\tau_{Auger} = \frac{\Delta n}{R_{Auger}} = \frac{\Delta n}{np(1.8\times10^{-24}n_0^{0.65}+6\times10^{-25}p_0^{0.65}+3\times10^{-27}\Delta n^{0.8})} \qquad (2.32)$$

where $n = n_0 + \Delta n$ (cm^{-3}) is the electron density and $p = p_0 + \Delta n$ (cm^{-3}) is the hole density, n_0 and p_0 are the electron and hole densities at equilibrium condition respectively. $\Delta n = \Delta p$ (cm^{-3}) is the excess carrier density. The n_0 and p_0 are determined from the product of the carrier densities at thermal equilibrium by law of mass-action, $n_0 \times p_0 = n_i^2$, where n_i is the intrinsic carrier density.

The last parameter which should be defined in equation 2.31 is $\tau_{Radiative}$. In the radiative recombination, an electron from the conduction band annihilates with the hole in the valence band, releasing the excess energy by emitting a photon with an energy close to E_g of c-Si. Hence, it could be said that radiative recombination is the reversed process of the optical generation process. The radiative lifetime $\tau_{Radiative}$ (s) is given via equation 2.33 [64].

$$\tau_{Radiative} = \frac{\Delta n}{R_{Radiation}} = \frac{\Delta n}{9.5\times10^{-15}np} \qquad (2.33)$$

It should be mentioned that in an indirect E_g semiconductor like c-Si, a phonon must be simultaneously emitted with a photon in order to conserve energy and momentum. Hence, such a four-particle process most probably does not occur in the c-Si wafer. Similar to the Auger recombination, the efficiency of radiative recombination depends on the excess carrier density and the wafer doping [54,64].

2.3 a-Si:H/c-Si heterostructure processing

This part describes the fabrication process starting with taking a c-Si wafer from its box to a finished SHJ solar cell. The whole process can be divided into two phases, wafer preparation and SHJ solar cell fabrication. The performance of the SHJ solar cells strongly depends on the c-Si surface condition. In contrast to the high-temperature passivation, such as SiO$_2$, no cleaning is needed for as-purchased polished c-Si wafers, due to the low temperature fabrication process the surface contaminants probably remain inactive. However, for a textured wafer with KOH solution, RCA cleaning is unavoidable.

2.3.1 Native oxide removal

In ambient air, the c-Si surface rapidly oxidizes forming a native oxide of a few nm thicknesses. Contrary to the thermally grown oxide, this native oxide has a very low quality and yields no surface passivation. Moreover, the native oxide acts as an insulator at the a-Si:H/c-Si interface and hinders the charge carriers transportation. Hydrofluoric acid (HF) efficiently removes the native oxide from the c-Si surface. After HF immersion hydrogen covers the silicon surface and a hydrophobic surface is obtained. Due to the safety classification of our chemical lab, we chose a HF dilution of 1 % with a dip-time of 3 min to assure the complete native oxide removal. For all double side polished (DSP) wafers that were purchased, the HF immersion is sufficient as a cleaning step. The passivation provided by the HF-dip is not stable over time and the lifetime decreases rapidly in ambient air. Figure 2.11 shows the lifetime of the bare c-Si wafer with <100> surface orientation before and after the

HF immersion. A rapid reduction in lifetime is observed after exposing to ambient air. Hence, it is necessary to load the c-Si as soon as possible into the load-lock of the deposition chamber under vacuum condition.
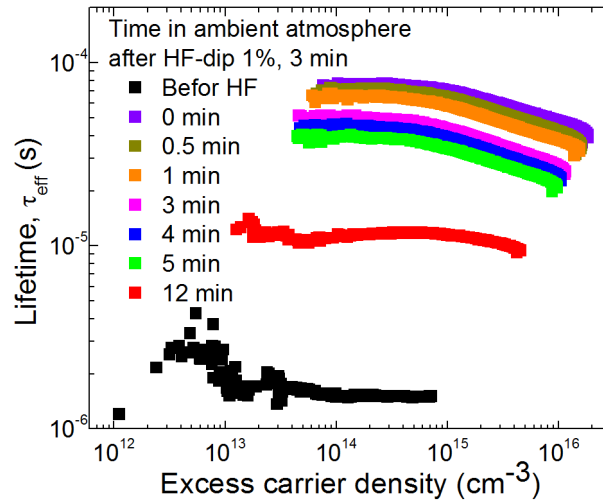
Figure 2.11 *c-Si <100> lifetime before and after HF immersion (1%, 3 min) for different periods of exposing to ambient air. Lifetime decreases rapidly in ambient air after HF-dip due to the reoxidation.*

2.3.2 SHJ solar cell fabrication process

There are several fabrication techniques for the deposition of thin-film silicon layers. Among them, the hot wire chemical vapor deposition (HWCVD) technique yields high quality layer properties but is disadvantageous for industrial use [65,66]. The most widespread deposition technique is the plasma enhanced chemical vapor deposition (PECVD). Indeed in the PECVD technique the gases are decomposed by plasma and are deposited on the substrate. In this study, we used the conventional parallel plate PECVD with the excitation frequency of 13.56 MHz. Doped and intrinsic layers were fabricated in separate chambers (with a cluster PECVD system made by VON ARDENNE) without breaking the vacuum during transportation. In our system, the lower electrode is the grounded electrode which contains the substrate holder. The upper electrode is fed by a generator at a frequency of 13.56 MHz where an automatically adjusted match box ensures a maximal power injection into the plasma. The process gas flux is injected from the shower head upper electrode and a butterfly valve is used for pressure regulation.

```
┌─────────────────────────────────────────┐
│              c-Si wafer                  │
└─────────────────────────────────────────┘
                    ↓
┌─────────────────────────────────────────┐
│        HF (1%, 3 min) immersion          │
└─────────────────────────────────────────┘
                    ↓
┌─────────────────────────────────────────┐
│        i/n layers PECVD deposition       │
└─────────────────────────────────────────┘
                    ↓
┌─────────────────────────────────────────┐
│        HF (1%, 3 min) immersion          │
└─────────────────────────────────────────┘
                    ↓
┌─────────────────────────────────────────┐
│        i/p layers PECVD deposition       │
└─────────────────────────────────────────┘
                    ↓
┌─────────────────────────────────────────┐
│   Leave one piece for lifetime measurement │
└─────────────────────────────────────────┘
                    ↓
┌─────────────────────────────────────────┐
│       Structuring into individual cells  │
└─────────────────────────────────────────┘
                    ↓
┌─────────────────────────────────────────┐
│          Front ZnO:Al deposition         │
└─────────────────────────────────────────┘
                    ↓
┌─────────────────────────────────────────┐
│   Back ZnO:Al and Al reflector deposition │
└─────────────────────────────────────────┘
                    ↓
┌─────────────────────────────────────────┐
│             Characterization             │
└─────────────────────────────────────────┘
```
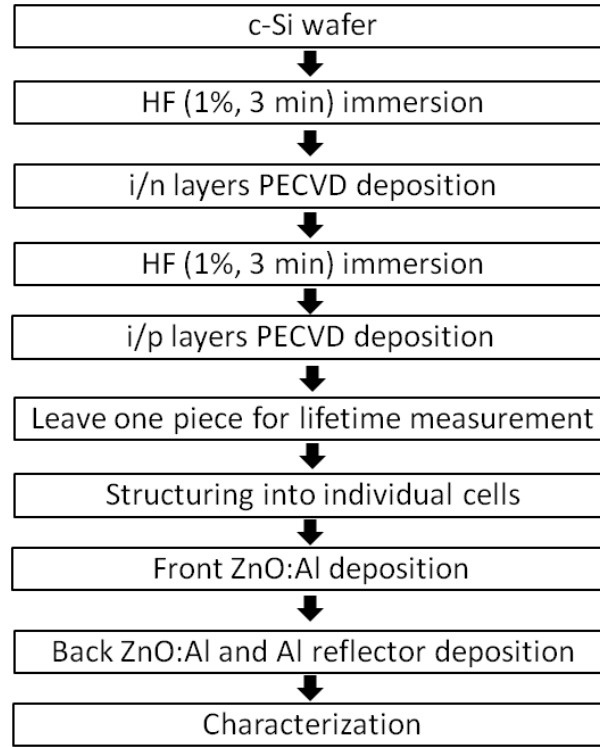
Figure 2.12 *Fabrication process of a SHJ solar cell*

The fabrication process of a SHJ solar cell is shown in figure 2.12. For the fabrication of SHJ solar cells, we purchased double side polished float zone (FZ) 100 mm diameter wafers with <100> surface orientation (with the resistivity of 1-5 Ω.cm) from Topsil company. Usually, half of the wafer was used for each SHJ solar cell. After HF-dip (1%, 3 min), the c-Si was transferred into the vacuum as fast as possible to prevent reoxidation. For the back side, 5 nm i a-Si:H and 15 nm n-type a-Si:H (BSF) were deposited. A second HF-dip was carried out before growing the passivation and emitter layer. After that, the sample was divided into two parts to keep one half for lifetime measurement. On the other part, individual solar cells were separated by a marker. After the deposition of the front transparent conductive oxide (TCO), the sample was turned and full area TCO/Ag layers were deposited as back contact (figure 4.1(a)). The marker together with the film on top of that was dissolved in acetone. Then the JV, EQE and Suns-V_{OC} measurements were performed. A detailed description of the used process parameters is given in the corresponding sections.

Chapter 3

3 a-Si:H/c-Si interface passivation: experiment & modeling

In this chapter, first the effect of PECVD process parameters including hydrogen flow, temperature and power on the passivation performance of the obtained a-Si:H layers are studied (section 3.1). Furthermore, section 3.1 demonstrates that post-deposition annealing is an effective treatment to improve the passivation quality. In section 3.2, the recombination at a-Si:H/c-Si interface is modeled based on the amphoteric nature of silicon dangling bonds and the modeling results are compared with the experimental results. The intrinsic a-Si:H passivation mechanism is addressed. Finally, the effect of each passivation mechanism on the injection level dependent lifetime is presented.

3.1 Influence of PECVD parameters on passivation

The compositional structure of the a-Si:H film depends on the plasma condition, affected by the incorporation of hydrogen atoms in the plasma and in the film during the growth [67]. The properties of a-Si:H/c-Si interface and the quality of passivation layer also strongly depend on the hydrogen content and the compositional structure of a-Si:H passivation layer [68]. Hence, the quality of the passivation layer is extremely important for the performance of fabricated SHJ solar cells. In this section, we address the effect of PECVD process parameters including hydrogen flow, power and temperature on the passivation performance of the intrinsic a-Si:H layers.

For the passivation study, n-type non-polished CZ wafers with a resistivity and a thickness in the range of 4-8 Ω·cm and 180±30 μm were used, respectively. The Fraunhofer ISE institute performed saw damage removal on the wafers in order to remove the kerf damage. It should be noted that no additional polishing or texturing was performed. To remove native oxide from the c-Si surface, we immersed the substrates in HF solution (1%) for 2 minutes,

prior to the deposition of each passivation layer. Figure 3.1 (a) and (b) show SEM micrographs of c-Si surface before saw damage removal and after saw damage removal ((c) and (d)). We measured the τ_{eff} in both QSS and transient mode (generalized condition) of the PC technique.

As mentioned in section 2.1.5, for the measurement in QSS mode, an optical constant should be defined which indicates the fraction of incident light that is absorbed in the wafer under test. A bare polished flat c-Si wafer has an optical constant of ~0.7. An optical constant of 1 is translated to a photogenerated current density of 38 mA/cm^2 at 1 sun in the Sinton QSS photo-conductance tool [69]. In order to determine the optical constant of our un-polished and un-textured c-Si substrate, we compared its reflection with the flat polished c-Si wafers. Figure 3.2 shows the measured reflection (solid lines) and transmission (dashed lines) of a bare polished flat c-Si wafer (red color), an unpolished untextured c-Si after saw damage removal (blue color) and a textured c-Si wafer (green color). The SEM micrographs of c-Si wafer before saw damage removal, after saw damage removal and after texturing are shown in figure 3.1(a), (c) and figure 5.6(f) respectively. As demonstrated by figure 3.2, the unpolished untextured c-Si wafer has almost the same reflection and transmission as the polished flat c-Si wafer. This suggests that an optical constant equal to the polished flat c-Si should be considered for such a substrate.
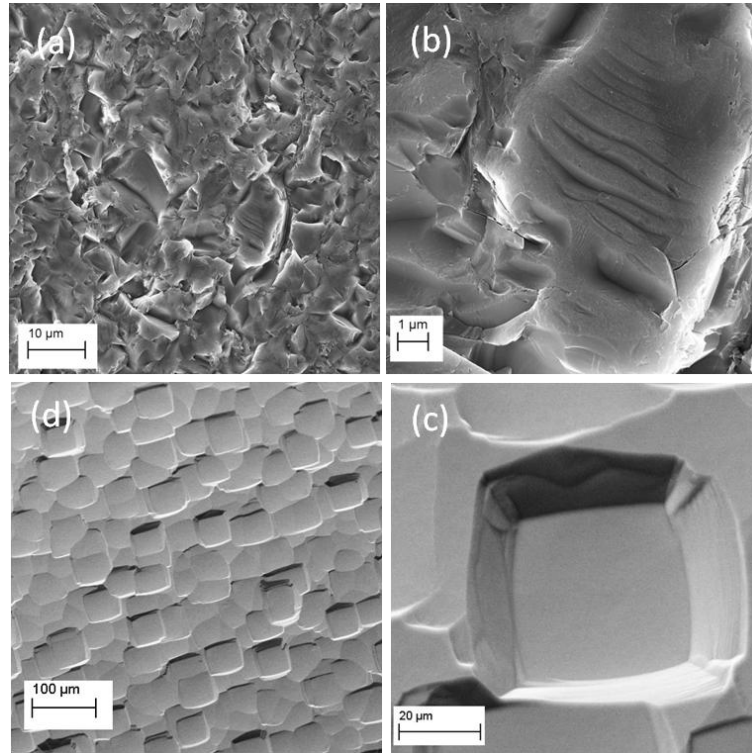

Figure 3.1: *SEM micropgraphs of (a) and (b) c-Si surface before saw damage removal and (c) and (d) after saw damage removal.*
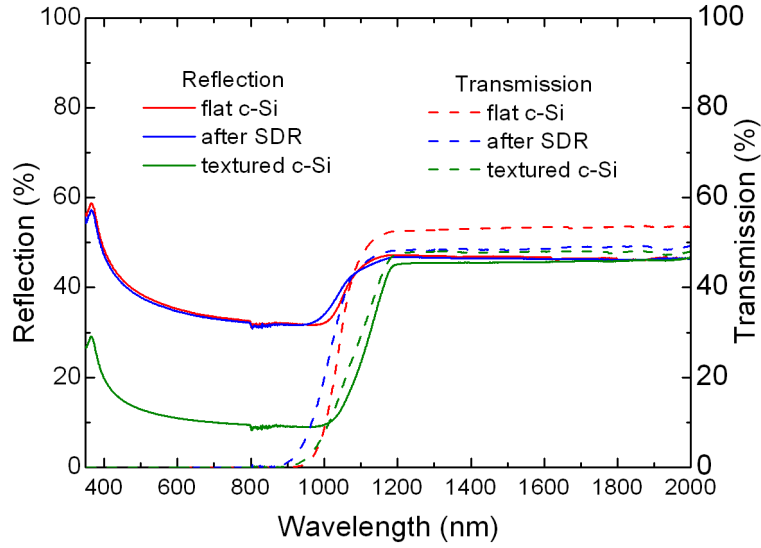
Figure 3.2: *Reflection (solid lines) and transmission (dashed lines) of a bare polished flat c-Si (red color), an unpolished and an untextured c-Si after saw damage removal (SDR) (blue color), and a textured wafer (green color), indicating that the bare polished flat wafer and the textured wafer have similar reflection and transmission.*

3.1.1 Hydrogen dilution and power effects

Figure 3.3(a) and (b) show the measured τ_{eff} of c-Si wafers passivated by the a-Si:H layer (deposited thickness of 18±3 nm) with various H_2 flows in the range of 0-300 sccm, corresponding to various hydrogen dilutions $H_{dil} = \frac{[H_2]}{[SiH_4]}$ in the range of 0-7.5, for two different powers of 15 and 25 W respectively. The other PECVD parameters are kept constant (reported in table 3.1).

The effective minority carrier lifetimes of the samples were evaluated in both, QSS and transient mode (generalized condition), immediately after deposition and after a post-deposition annealing for 60 min at 190 °C in air ambient. The values for τ_{eff} are reported at minority excess carrier density (Δn) of 10^{15} cm^{-3}. As shown in both figure 3.3(a) and (b), the measured values before the post-annealing process do not show any significant improvement with increasing the H_2 flow. The measured τ_{eff} values (open symbols) for as-deposited samples only change from 16 to 97 μs and 16 to 58 μs for deposition power of 15 and 25 W respectively. Due to the poor passivation of as-deposited a-Si:H films, the measurement in the transient mode is meaningless as the measured τ_{eff} in this mode is only valid with a lifetime higher than 100 μs [69].

After the post-deposition annealing, two significantly different τ_{eff} behaviors have been observed. For 15 W series, τ_{eff} of samples, deposited with 100 sccm H_2 flow (H_{dil}: 2.5) or less H_2 flows, significantly improves after a post-deposition annealing. Similarly, the same improvement in τ_{eff} could be observed for 25 W series deposited with H_2 flow up to 200 sccm (H_{dil}: 5). However, the above, H_{dil} of 2.5 for the 15 W series (H_{dil} of 5 for the 25 W series), QSS lifetime values were less than the as-deposited values. In a study by De Wolf *et al*, it has been shown that the drop in the QSS lifetime after post-deposition annealing treatment indicates the epitaxial growth at a-Si:H/c-Si interface [70]. Thus, the reduction of the QSS lifetime value (after post-deposition annealing) could most probably be attributed to the formation of the epitaxial growth due to the high hydrogen dilution. The observed drop in

QSS lifetime values, at higher hydrogen dilution (H_{dil}: 5) for 25 W series compared to 15 W series (H_{dil}: 2.5), could also be related to higher silane depletion fraction with increasing power [68]. This could shift the onset of the epitaxial growth for the 25 W series to higher dilution values, since the drop in QSS lifetime, after the post-deposition annealing, was observed at higher hydrogen dilutions. By increasing the H_2 flow, (till 100 sccm for 15 W series and 200 sccm for 25 W series) the lifetime increases. The increase in lifetime could be attributed to the dependence of the a-Si:H film microstructure and the a-Si:H/c-Si interface on the plasma hydrogen content [67]. It has been shown that the a-Si:H/c-Si interface does not have unique electronic properties and its properties are governed by the a-Si:H bulk passivation layer [71]. The deposition of a-Si:H layers with higher hydrogen dilution values leads to a lower defect density (dangling bond density) in the a-Si:H network and hence, results in a higher passivation quality at the a-Si:H/c-Si interface [71].

Table 3.1: *Process parameters used for the fabrication of the intrinsic a-Si:H passivation layers with various hydrogen flows.*

Silane flow (sccm)	Deposition temp. (°C)	Pressure (mbar)	Electrode distance (mm)
40	200	1	20

Apart from the hydrogen flow effect, we observed a drop in the QSS lifetime (after post-deposition annealing) at the same hydrogen dilution for polished and unpolished c-Si wafers. This may indicate that the micrometer roughness of the unpolished c-Si wafers does not have any effect on the onset of epitaxial growth. The formation of the epitaxial growth at higher hydrogen dilution could be related to the hydrogen coverage [72]. Thus, the diffusion length of silane species increases and the crystalline grains form [72]. Moreover, it has been shown that the doping level and pre-treatments of the c-Si wafers affect such a epitaxial growth [73].

An abrupt atomically sharp a-Si:H/c-Si interface is mandatory to reach a high surface passivation and lifetime [70]. This condition is not satisfied in the case of epitaxial growth. Hence, the epitaxial growth deteriorates the passivation quality and the solar cell performance suffers from a low V_{OC} [74,75]. The reduction in the QSS lifetime (for samples likely with epitaxial growth) after the annealing step is attributed to an increased defect density at the interface. In as-deposited epitaxial films, most of the H_2 atoms are not bonded but are present in the form of atomic H^+ in a way that the annealing causes them to diffuse away from the interface. As a result of their increased interface defect density, losses in passivation can be observed [70].
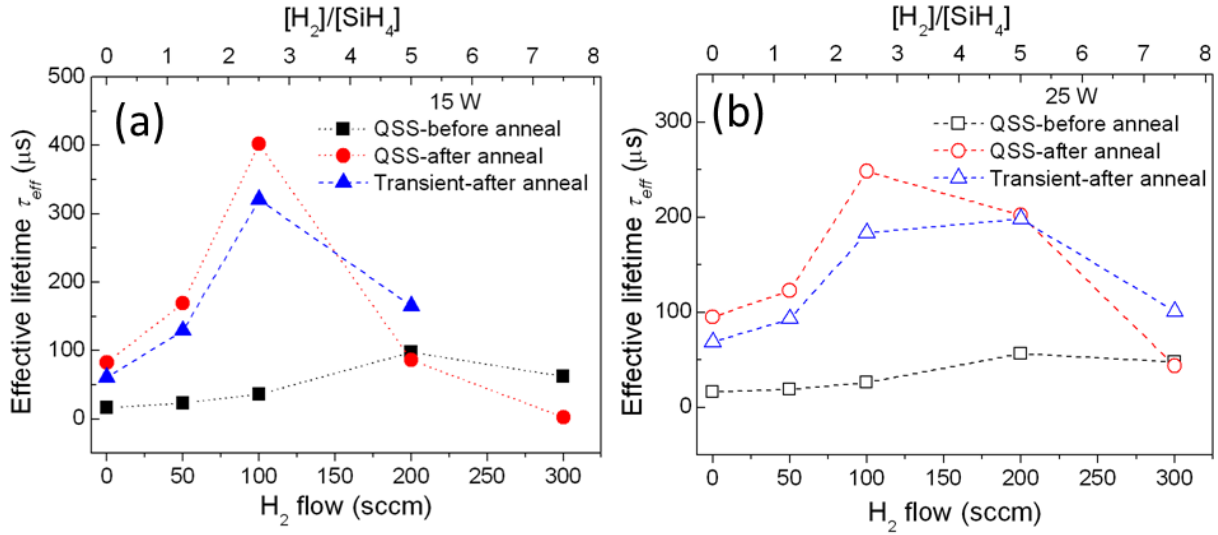
Figure 3.3: *The variation of the τ_{eff} (Δn:10^{15} cm^{-3}) with respect to the H_2 flow for two different powers of (a) 15 and (b) 25 W. The measurements were done as-deposited as well as after a post-deposition annealing (60 min, 190°C in air ambient) in both the QSS and transient modes (generalized condition) of the photoconductance technique.*

A general trend exsists for all the samples shown in figure 3.3 (except those deposited without H_2 flow), indicating lower τ_{eff} for 25 W series compared to the 15 W series. This could be attributed to the increased DB density due to the higher ion bombardment at higher power [76,77]. For samples deposited without H_2 flow, almost the same τ_{eff} were measured for both series: 15 and 25 W. This similar τ_{eff} could be attributed to the high defect density in these samples which is not affected by the higher ion bombardment at higher power.

Additionally, for the both power series samples shown in figure 3.3 (all epitaxial-free samples), higher lifetime were measured in the QSS mode than the transient mode. Moreover, by improving the quality of the passivation layers, the increase in the QSS lifetime is higher than the transient lifetime. The higher measured lifetime in the QSS could be explained by the high recombination rate that exists in the bulk of the low quality CZ c-Si wafers used and by the different interface thicknesses monitored in each mode [78]. However, further investigation is required regarding the interface thickness monitored in each mode.

It should be noted that the electrical properties of the thin a-Si:H layers (~5 nm) are different from the thick samples (~40 nm). The thickness of the deposited a-Si:H layers strongly affects the τ_{eff} value. The surface recombination velocity decreases with an increasing a-Si:H thickness up to ~40 nm. It has been shown that the optimum thickness for film relaxation is ~40 nm [77]. With layers thicker than 40 nm, the surface recombination velocity increases again, probably due to the mechanical stress [79]. Due to the strong dependency of the a-Si:H/c-Si interface properties on the bulk properties of a-Si:H passivation layers [71], the deposited thickness should be considered for optimization of the a-Si:H passivation layers. In other words, an optimized recipe for a thick layer may not result in SHJ solar cells with a high V_{OC} when it is used for deposition of a thin a-Si:H film (~5 nm). Last but not the least, the reactor condition before deposition for example cross contamination, base vacuum level and the history of previous depositions also influence the passivation quality [68].

3.1.2 Post-deposition annealing treatment

Unlike the observed drop (figure 3.3) in the lifetime of samples deposited at hydrogen dilution higher than 2.5 for the 15 W series (hydrogen dilution of 5 for the 25 W series), the post-deposition annealing improves the passivation of the samples deposited at hydrogen dilution of 2.5 or lower for the 15 W series (hydrogen dilution of 5 for the 25 W series). In a good agreement with the increase in H_2 flow, a higher lifetime (for both the QSS and the transient mode) is measured after the post-deposition annealing for the samples, deposited at higher hydrogen dilutions. The lifetime improvement, after the post-deposition annealing, is attributed to the relaxation of the a-Si:H network. By restructuring the amorphous network, a new network forms consisting of more bonding states and reduced strained Si-Si bonds [57,80].

Moreover, by the diffusion of hydrogen atoms from the amorphous network to the a-Si:H/c-Si interface, the DB density reduces at the interface [80]. It should be noted that such a post-deposition annealing of intrinsic a-Si:H passivation layers is systematically performed during the fabrication of the SHJ solar cells. Considering the SHJ solar cell fabrication steps (see figure 2.12), the substrate is kept at a high temperature for the deposition of the emitter and the BSF layers after the deposition of the intrinsic a-Si:H passivation layers. In addition, the solar cell precursor is exposed to a high temperature (~300°C) during the deposition of front and back TCO layers (when ZnO TCO layer is used).

3.1.3 Deposition temperature effect

The deposition temperature of a-Si:H film is another important parameter which determines its microstructure and therefore affects the a-Si:H/c-Si interface passivation and the corresponding V_{OC} value. Figure 3.4 shows the dependence of τ_{eff} on the deposition temperature of the a-Si:H passivation layers in the range of 150-240°C. The other deposition parameters are kept constant, as reported in table 3.2.

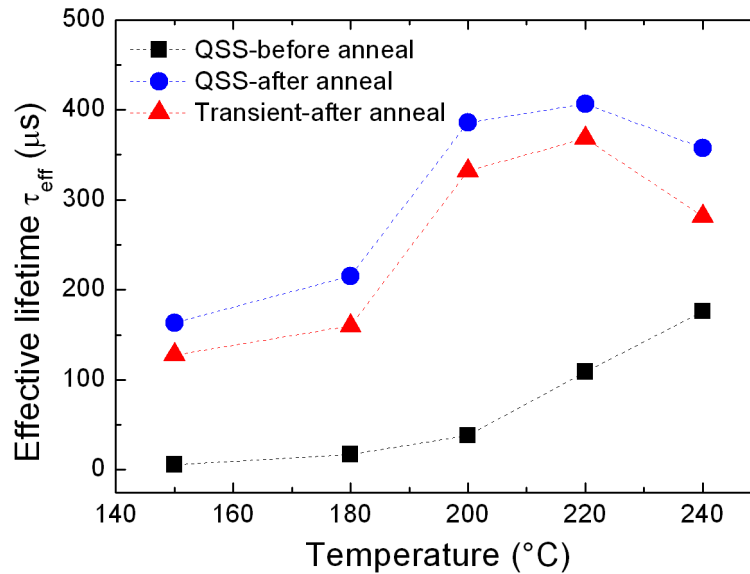**Figure 3.4:** *The τ_{eff} (at Δn: $10^{15} cm^{-3}$) for CZ c-Si wafers deposited with a-Si:H films at various temperatures. The respective square and circle data series correspond to the QSS lifetime (in generalized condition) before and after the post-deposition annealing. The triangle data series shows the transient mode lifetime (in generalized condition) after the annealing process.*

As the data suggests, as-deposited QSS lifetime increases with the deposition temperature (black data series in figure 3.4). This shows that the deposition temperature could significantly affect the quality of the grown a-Si:H passivation layers. Indeed, the deposition temperature affects the mobility of plasma species reaching to the surface and more importantly (for a-Si:H films), the diffusivity of hydrogen atoms [81]. Deposition at low temperatures results in a-Si:H layers with a high density of unsaturated bonds and hence, a higher defect density [62,81]. The highest τ_{eff} is obtained for sample deposited at 220°C. Although the highest as-deposited τ_{eff} was measured for the sample deposited at 240°C, the obtained lifetime improvement for this sample is much lower than other samples deposited at 200 and 220°C after post-deposition annealing treatment. These results agree with the study of Bahardoust *et al.*[57]. Indeed, deposition at temperatures higher than 220°C could result in a poor passivation layer, due to the effusion of hydrogen atoms and the defect creation at the interface [57,82]. Moreover, it has been shown that deposition at higher temperatures could result in partial epitaxial growth [83]. In our case, the lower achieved gain in τ_{eff} (after post-deposition annealing) in sample deposited at 240°C (compared to the ones deposited at 200 and 220°C) is probably due to the lower hydrogen content in the film, most likely due to the escape of hydrogen atoms during fabrication. The improved τ_{eff} after the post-deposition annealing (observed for both the QSS and the transient mode) is a good indication that the epitaxial growth improbably happens.

Table 3.2: *Process parameters for the a-Si:H passivation layers deposited at various deposition temperatures.*

SiH$_4$ flow (sccm)	H$_2$ flow (sccm)	Pressure (mbar)	Electrode distance (mm)	Power (W)
40	100	1	17	15

The blue and red data series in figure 3.4 show τ_{eff} after the post-deposition annealing process for both the QSS and the transient mode, respectively. As already discussed, the post-deposition annealing significantly improves the layer passivation most probably due to the hydrogen diffusion to the interface and relaxation of the a-Si:H network. The passivation improvement (similar to the hydrogen dilution study) strongly depends on the initial quality of the a-Si:H films. In other words, for all samples (except those deposited at 240°C), more gain is observed for samples with higher as-deposited τ_{eff}. As an example, ~158 µs gain is observed for the sample deposited at 150°C (in the QSS mode), whereas ~298 µs gain is observed for the sample deposited at 220°C. Similar to the hydrogen dilution series study, the lifetime measured in the transient mode (red data series) is lower than the lifetime measured in the QSS mode (blue data series). The difference between the values measured in the transient mode and the QSS mode increases with the passivation layer quality improvement. The higher gain obtained (after the post-deposition annealing) for samples with higher as-deposited τ_{eff}, highlights the importance of high quality passivation layer. Although the quality of the deposited passivation layer could be improved by various treatments, such as post-deposition annealing and intermediate/final hydrogen plasma treatment [29,84], a well-functioning passivation could only be obtained for as-deposited high quality layers.

3.2 a-Si:H/c-Si interface recombination modeling results

This section presents the results of recombination modeling at a-Si:H/c-Si interface and compares them with the experimental results. Based on the molding results, the a-Si:H passivation mechanism is addressed. Finally, the effect of each passivation mechanism (addressed in section 2.2.1) on the injection level dependent τ_{eff} is discussed.

3.2.1 Understanding a-Si:H passivation mechanism

It should be noted that the values for N_s and Q_s obtained by our modeling are no absolute values, however, they could be used for a relative comparison of various samples [85]. In our model, we have used the following values, taken from Refs [50,57,86]. The charge velocity at room temperature in Si is $v_{th}(cm/s) = 2.3 \times 10^7$, the neutral electron to hole capture cross section is $\frac{\sigma_n^0}{\sigma_p^0} = 0.05$, the charged to neutral capture cross section is $\frac{\sigma_n^+}{\sigma_n^0} = \frac{\sigma_p^-}{\sigma_p^0} = 550$ and the hole capture cross section is $\sigma_p^0(cm^2) = 1 \times 10^{16}$.
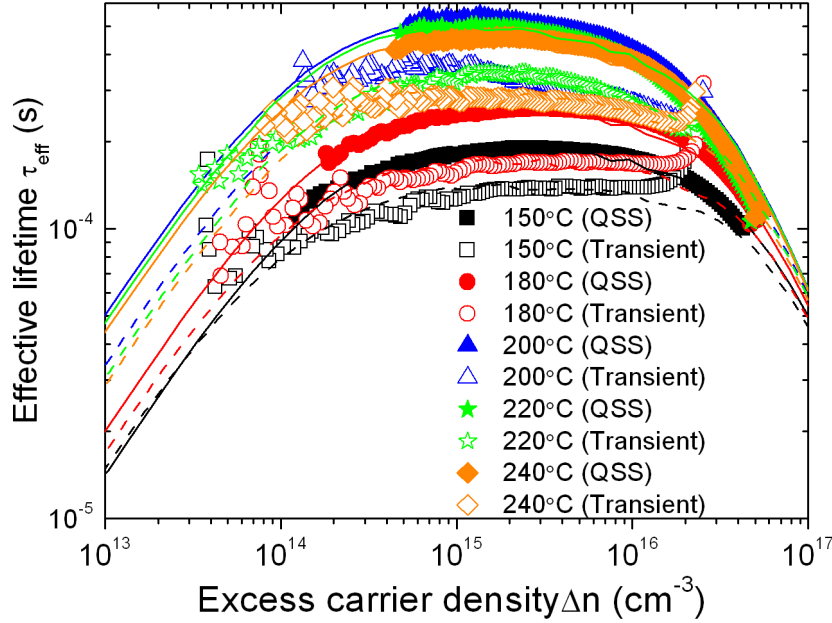
Figure 3.5: *The injection level dependent $\boldsymbol{\tau_{eff}}$ for samples deposited at various temperatures after the post-deposition annealing. The data points represent the experimental results. The solid and dashed lines illustrate the simulation data. The N_s and Q_s values, obtained from our molding are reported in table 3.3.*

Figure 3.5 shows the injection level dependent τ_{eff} for the a-Si:H passivation layers, deposited at various temperatures. The other PECVD parameters are kept constant, as reported in table 3.2. The solid and dashed lines represent the modeling results whereas the data points show the experimental results. As figure 3.5 suggests, the experimental data points are match with the modeling results. The N_s and Q_s values, obtained from our molding are reported in table 3.3.

Table 3.3: *Interface defect density (N_s) and surface charge density (Q_s) extracted from modeling for the a-Si:H passivation layers, deposited at various temperatures.*

Sample	Deposition temperature (°C)	Measurement mode	N_s (10^{10} cm^{-2})	Q_s (10^9 cm^{-2})
X050-1-067	150	QSS	2.7	9
X050-1-067	150	Transient	3.4	7.9
X050-1-068	180	QSS	1.95	9.3
X050-1-068	180	Transient	2.8	8.8
X050-1-066	200	QSS	0.96	9.4
X050-1-066	200	Transient	1.5	9.2
X050-1-070	220	QSS	0.93	9.6
X050-1-070	220	Transient	1.4	9.6
X050-1-071	240	QSS	1.1	9.4
X050-1-071	240	Transient	1.7	9.1

Figure 3.6 demonstrates the N_s value (extracted from our modeling) with respect to the deposition temperature for the QSS mode. While almost similar Q_s values (see table 3.3) are extracted from modeling for all the a-Si:H passivation layers, there is a direct relation between the improved passivation and the reduction in N_s (see figure 3.6). These results suggest that the reduction of the interface defect density is the main mechanism of the surface passivation by using a-Si:H films. Thus, it can be concluded that the a-Si:H passivation mechanism is a chemical passivation.

As mentioned above, the closed-form recombination model allows us to distinguish between the two fundamental approaches for the surface recombination reduction; either reduction of the interface defect density (N_s parameter in the model) or reduction of the surface density of one carrier type (Q_s). In practice, the interface defect density reduction could be achieved by reducing the recombination center density (dangling bonds at a-Si:H/c-Si interface). The reduction of one carrier type is technologically realized by implementing a dopant profile either underneath the c-Si surface or by creating an electric field by means of electrostatic charges with an overlaying doped layer. The injection level dependent τ_{eff} are not equally affected by these passivation approaches.
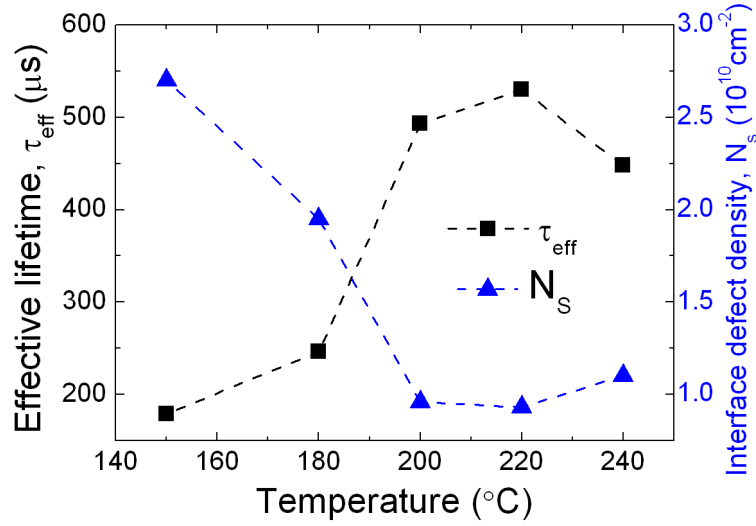
Figure 3.6: *The variation of the measured τ_{eff} (black square) and the interface defect density (N_s) (blue triangle, extracted from modeling) with respect to the deposition temperature of the a-Si:H passivation layers. The improved τ_{eff} with reduction of N_s indicates that passivation formed by using intrinsic a-Si:H films, is a chemical passivation.*

3.2.2 The effect of passivation mechanisms on the injection level dependent lifetime

Figure 3.7(a) shows the modeled injection level dependent τ_{eff} for the set Q_s value of 9.7 $\times 10^9$ (cm^{-2}) and various N_s values. As this graph suggests, the variation of interface defect density (N_s) equally affects all the injection level dependent τ_{eff} values for the injection levels lower than 10^{16}. This can also be deduced from equation 2.18. As the recombination rate R_{DB} is in direct relation with N_s ($R_{DB} \propto N_s$), by reducing Ns, τ_{eff} increases for all the excess carrier densities with the same factor.
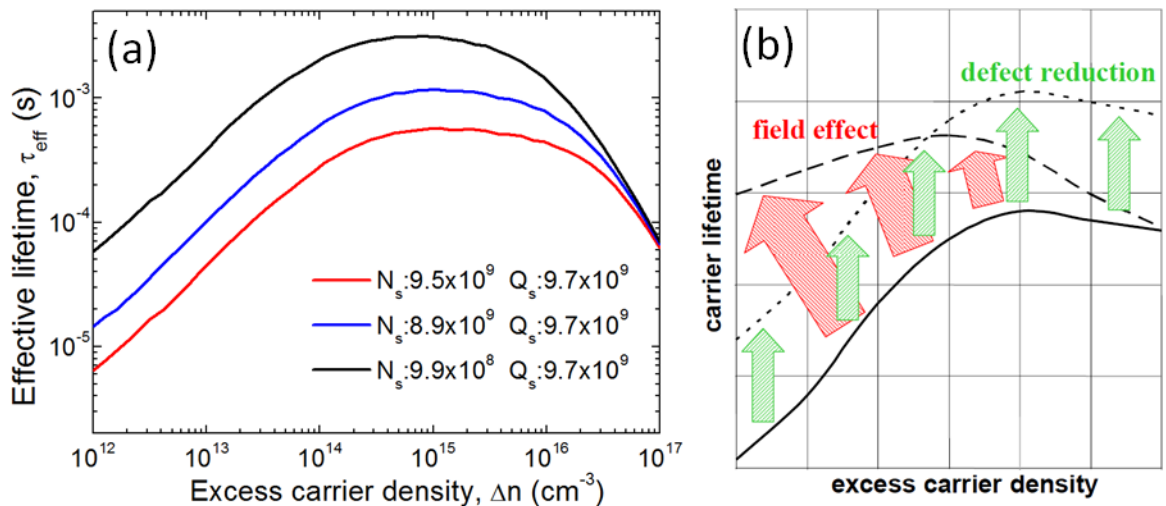
Figure 3.7: (a) *The effect of variation of the interface defect density on the injection level dependent τ_{eff}. The effect of the interface defect density is observed on all injection levels. (b) The effect of the field effect passivation on the injection level dependent τ_{eff} compared to the effect of the interface defect density variation. The influence of the field effect passivation is more weighted at low injection levels [Courtesy of S. Glunz].*

The effect of the field effect passivation on the injection level dependent lifetime is different from the effect of the interface defect density variation. Figure 3.7(b) shows the effect of the field effect passivation on the injection level dependent lifetime compared to the effect of interface defect density variation. As this figure suggests, the effect of the field effect passivation is not the same on all the excess carrier densities and is more weighted at low injection levels [87]. The results of the current section have been used in chapter 4 to explain the passivation mechanism of the μc-Si:H emitter layers where both passivation mechanisms could simultaneously be obtained.

It should be noted that good passivation is the first essential step required for the fabrication of well-functioning SHJ solar cells. The results, presented in chapter 3, are well in-line with already published reports from other groups. The new results and achievements within the framework of this thesis are presented in the following chapters.

3.3 Conclusions on a-Si:H/c-Si interface passivation: experiment & modeling

In order to reduce the recombination through DBs, an excellent passivation is required for SHJ solar cells. The intrinsic a-Si:H film acts as a high performance passivation layer on the c-Si substrate. The most significant advantage of the a-Si:H passivation layer compared to other conventional passivation films such as SiO_2 and SiN_x, is its low temperature fabrication process by using the PECVD technique.

The effect of the PECVD process parameters including hydrogen flow (hydrogen dilution), power and deposition temperature on the a-Si:H passivation performance was studied in section 3.1. Our results show that the passivation improves with increasing the hydrogen flow up to 100 sccm (hydrogen dilution of 2.5) for (100) oriented c-Si wafers. For higher hydrogen dilutions, a reduction in the measured lifetime was observed, most probably due to the partial epitaxial growth.

The deposition power also affects the passivation where by increasing the deposition power, the onset of epitaxial growth shifts to higher dilution values probably due to the higher silane gas dissociation. However, due to the increased ion bombardment at higher power, the higher hydrogen dilution is not beneficial for the passivation. In addition, we studied the effect of post-deposition annealing treatment on the passivation. It was found that the annealing treatment improves the passivation of the epitaxial-free samples. Moreover, it was observed that the lifetime improvement (after post-deposition annealing) is more significant for the a-Si:H passivation layers that were deposited with higher hydrogen flows.

The temperature study showed that the best passivation was achieved for the a-Si:H layers deposited at ~220°C. Moreover, our findings suggest that although some treatments such as post-deposition annealing improve the passivation, it is highly important to start with high quality passivation layers (deposited with optimized PECVD parameters). Furthermore, the gain in the lifetime after post-deposition annealing strongly depends on the initial passivation quality.

In section 3.2, to understand the a-Si:H passivation mechanism, the recombination at the a-Si:H/c-Si interface was modeled by considering the ampotheric nature of the DBs. The modeling results suggest that there is a direct relation between the improved lifetime and the reduced interface defect density. Hence, it was concluded that the passivation mechanism of a-Si:H films is the chemical passivation due to the hydrogenation of DBs.

Finally, the effect of each passivation mechanism on the injection level dependent τ_{eff} was addressed: interface defect density equally affects all injection level dependent τ_{eff} and the effect of the field effect passivation is more weighted at low injection level dependent τ_{eff}.

Chapter 4

4 µc-Si:H layer for SHJ solar cells

In this chapter, first we address the requirements that should be satisfied by the emitter layer in the SHJ solar cell structure (section 4.1). Then, we study the effect of the emitter conductivity on the electrical properties of the SHJ solar cells (section 4.2-4.3). We gradually change the emitter from a lowly doped a-Si:H film to a highly conductive µc-Si:H layer and monitor its impact on the performance of the obtained solar cells as well as on the solar cell precursors. To vary the conductivity of the µc-Si:H layers, we take advantage of the improved conductivity by crystallinity evolution within the thickness. This allows us to study the effect of the emitter conductivity without introducing any additional interrelated parameters such as introducing a higher defect density by varying doping levels.

We introduce the µc-Si:H films as a novel emitter for the SHJ solar cells and address several technological advantages which can be achieved by fabrication of the µc-Si:H emitter layers such as suppressing the Schottky barrier at the emitter/TCO junction and improving the passivation at a-Si:H/c-Si interface (section 4.3). Moreover, the effect of the emitter conductivity on the Schottky barrier at the ZnO:Al/emitter is investigated (section 4.4). Finally, it is demonstrated that deposition at lower pressures results in faster nucleation of the µc-Si:H layer.

4.1 Emitter roles in SHJ solar cells

In order to create a p-n junction, the emitter doping type (either n- or p-type) should be opposite of the c-Si substrate material. In SHJ solar cells, the preferred substrate is the n-type c-Si wafer. The choice of n-type could be explained by several reasons. First, the most impurity transition metal defects (that exist in the c-Si bulk) have a higher electron capture cross-section than hole capture cross-section. Hence, for the same impurity concentration, the bulk minority carrier lifetime is usually higher for the n-type c-Si substrate than for the p-type counterpart [88]. Secondly, the bulk lifetime of the p-type c-Si wafer is detrimentally affected by light-soaking when either oxygen or iron is simultaneously present with boron [89,90]. So far, such effects have not been reported for the n-type c-Si. Thirdly, the dangling bonds at the surface have a higher electron capture cross-section than hole capture cross-section [50],

which makes the p-type c-Si wafer passivation more difficult than the n-type counterpart. Due to the abovementioned reasons and the principle effect of the conduction or valance band offset (depending on the substrate type) [91], most contemporary high-efficiency SHJ solar cells were achieved on n-type c-Si wafers.

To form the p-n junction on the n-type wafers, often 10 to 15 nm p-type a-Si:H is deposited by means of the PECVD technique [92]. From the optical point of view, it is highly important that the absorption in the emitter is kept as low as possible, as the photogenerated carriers in the emitter do not have any contributions to the J_{SC}. Indeed, the emitter is a dead layer [93]. Moreover, the emitter doping level plays a significant role in the performance of the SHJ solar cells. The emitter roles are addressed in several aspects, as follows:

(i) The emitter should be sufficiently doped to provide the required electric field in order to repel the electrons from the emitter/c-Si interface. A high electron density at the emitter/c-Si interface increases the recombination rate at the surface. Consequently, the V_{OC} value decreases in the final device, due to the increased high saturation current density [94].

(ii) Sufficient band bending in the c-Si substrate as well as at the edge of the emitter layer should be created by the emitter to allow tunneling process of the minority carriers [95]. The minority carriers tunneling are inhibited by a lowly doped emitter which results in low FF values [96,97].
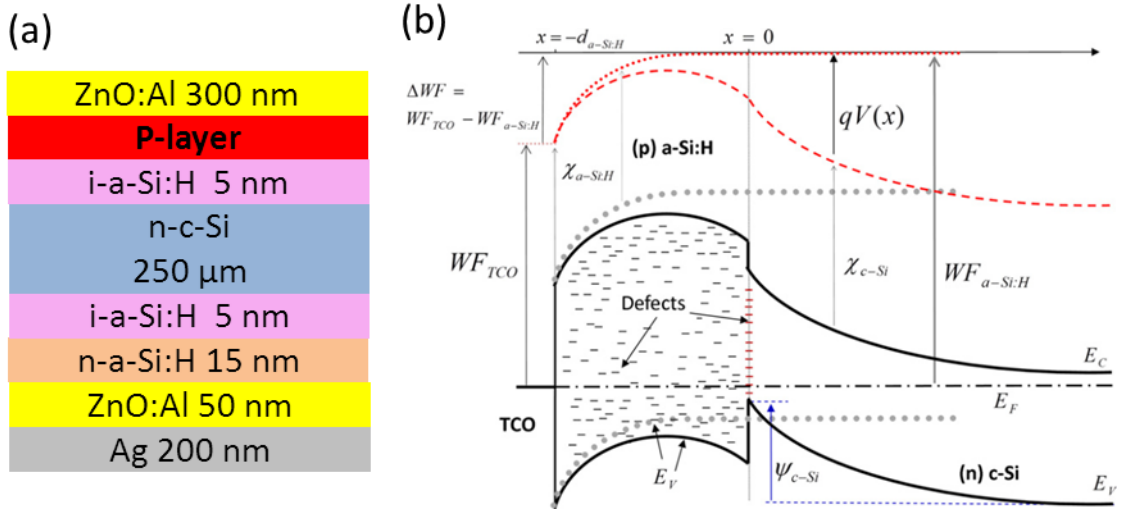

Figure 4.1: *(a) The schematic illustration of the fabricated SHJ solar cells employing ZnO:Al with the corresponding thickness of each layer (drawn not to scale) (b) Band diagram of the TCO/(p)a-Si:H/(n)c-Si heterojunction (solid black lines). The gray points demonstrates the conduction and valence band edges of the (p)a-Si:H for (p)a-Si:H/TCO junction (i.e. infinite (p)a-Si:H layer thickness), only. Red dashed and dotted lines indicate the electrostatic potential for the heterojunction and single junction respectively. The Schottky barrier forms as well, due to the lower TCO work function than a-Si:H film. Figure 4.1 (b) was taken from Ref. 95.*

(iii) In the SHJ solar cells, the lateral conductivity of the a-Si:H films (forming the emitter and BSF layers) is inferior compared to the c-Si counterparts. Therefore, a TCO layer (usually a n-type semiconductor) must be deposited on the emitter layer to improve the carrier collection, as shown in figure 4.1 (a). The work function of the TCO is lower than the work function of a-Si:H or μc-Si:H material. This results in the formation of the Schottky barrier, where the barrier height is governed by the difference between the work function of the emitter and the TCO materials. Hence, a highly conductive emitter layer is required to suppress the Schottky barrier height and push the junction to the ohmic contact-type.

(iv) In SHJ solar cells, the p-type emitter is sandwiched between two n-type semiconductors, the TCO and the c-Si wafers. The formation of the p-n junction at the TCO/emitter and the emitter/c-Si causes the emitter to be depleted from both sides. This condition is shown in figure 4.1 (b). Therefore, the emitter should be sufficiently doped to sustain the flat band in the emitter layer, i.e. the emitter should prevent merging the band bending at the TCO/emitter interface with the band bending at emitter/c-Si interface. Hence, sustaining the flat band in the emitter layer is essential to extract the maximum created built-in-voltage at the emitter/c-Si and thus achieving high V_{OC} values.

All before mentioned requirements combined with the thin emitter layer thickness required make the design of the emitter layer a challenge. Therefore, it is essential to optimize the PECVD process parameters precisely in order to satisfy all these requirements.

4.2 Emitter conductivity effect on SHJ solar cells performance

In this section, we study the effect of the emitter doping level on the electrical properties of the fabricated SHJ solar cells with DC sputtered ZnO:Al. We vary the emitter layer from a lowly doped a-Si:H film to a highly conductive μc-Si:H layer and monitor its effect on the solar cell precursors as well as on the electrical properties of the fabricated solar cells.

Figure 4.1(a) shows the schematic illustration of the SHJ solar cells fabricated with DC sputtered ZnO:Al layers. N-type flat float-zone c-Si <100> wafers with resistivity of 1-5 Ω.cm were used as substrates. The intrinsic a-Si:H passivation layers were deposited with optimized PECVD process parameters illustrated in our previous study (chapter 3). The optimized process parameters are reported in table 3.2. DC sputtered ZnO:Al layers were deposited as TCO material. The deposition parameters are reported in table 5.1. Diborane (B_2H_6) diluted in H_2 with gas flows of 0.5 and 32 sccm were used to obtain two different doping levels for the p-a-Si:H emitter layers. Other PECVD process parameters for the p-type a-Si:H emitter are reported in table 4.1. To vary the conductivity of the μc-Si:H emitter layers, the dopant gas flows were kept constant and the film thickness was varied from 12 to 19 nm. As a result, different conductivities were achieved due to the crystallinity evolution within the thickness.

Table 4.1: *The PECVD process parameters used for deposition of the p-type a-Si:H layers. B_2H_6 with gas flows of 0.5 and 32 sccm were used to obtain two different doping levels*

SiH_4 flow (sccm)	H_2 flow (sccm)	B_2H_6 (sccm)	Pressure (mbar)	Electrode distance (mm)	Power (W)	Temperature (°C)
40	80	0.5 & 32	0.3	30-25	11	200

Figure 4.2 shows the normalized Raman spectra of the 5 nm intrinsic a-Si:H passivation layer together with the p-type a-Si:H emitter layer deposited with two different dopant gas flows (red: 0.5 sccm of B_2H_6 and black: 32 sccm of B_2H_6). Figure 4.2 also demonstrates the

Raman spectra of the μc-Si:H emitter layers (together with 5 nm intrinsic a-Si:H layer) deposited with different deposition times; including brown line for 300 s deposition time (~12 nm), green line for 400 s deposition time (~15 nm) and blue line for 500 s deposition time (~18 nm). For the Micro-Raman measurements, an excitation laser with a wavelength of 488 nm was used. The penetration depth at 488 nm wavelength is ~45 nm for the a-Si:H and 90-150 nm for the μc-Si:H film. As the evaluated thickness of the evaluated films is lower than the penetration depth at the wavelength of 488 nm, the obtained Raman spectra show the bulk film composition. As figure 4.2 suggests, the Raman peak at 510 cm^{-1} (characteristic peak for μc-Si:H material) dominates when increasing the deposition time of the μc-Si:H layer. This indicates a formation of the μc-Si:H layers with a higher crystallinity fraction (Φ_c). The determined crystallinity fraction (Φ_c) increases from 15%, for the μc-Si:H layer deposited for 300 s, to 22% and 37%, for the μc-Si:H layers deposited for 400 and 500 s respectively.
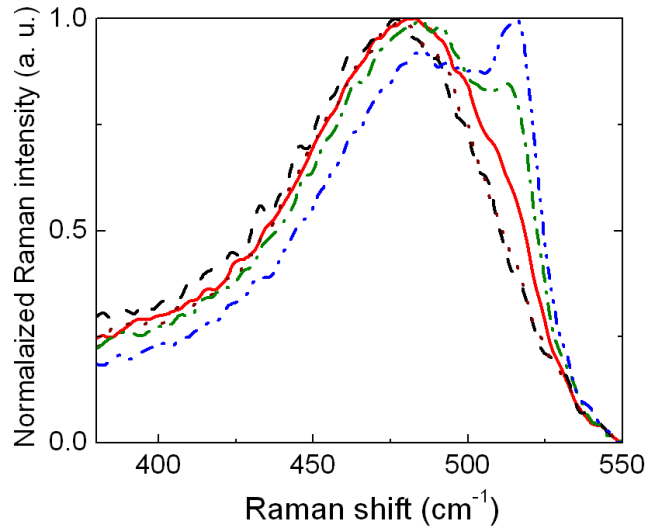
Figure 4.2: *Normalized Raman spectra of a 5 nm i a-Si:H passivation layer together with different emitter layers, red: 15 nm p-a-Si:H (B2H6: 0.5 sccm), black: 15 nm p-a-Si:H (B2H6: 32 sccm), brown: 13 nm p-μc-SiH (300 s deposition time, Φc = 15%) , green: 16 nm p-μc-SiH (400 s deposition time, Φc = 22%) and blue: 18 nm p-μc-SiH (500 s deposition time, Φc = 37%) in co-deposition with the SHJ solar cells on the glass substrate.*

The dark conductivity of the buffer and emitter layers deposited on the glass substrate in co-deposition with the SHJ solar cells is demonstrated in figure 4.3.

Figure 4.3: *The dark conductivity of a 5 nm intrinsic a-Si:H passivation layer together with a p-type a-Si:H layer deposited with different gas flows (open symbols) or p-type µc-Si:H layers deposited with different deposition t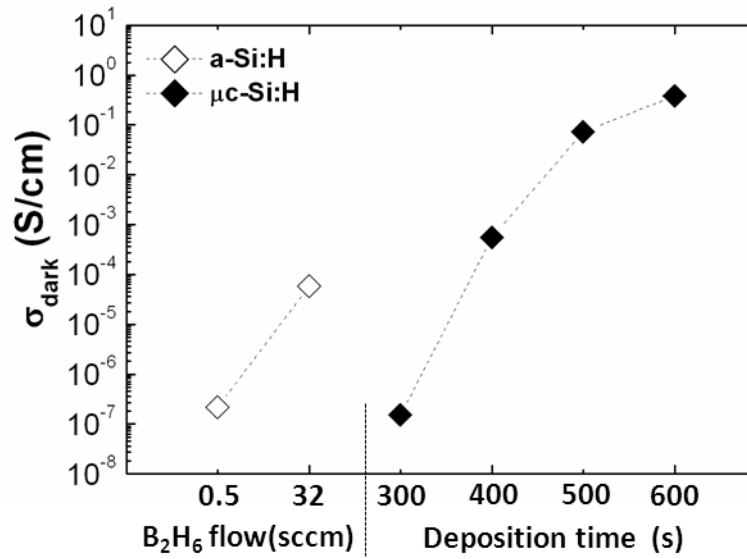imes from 300 to 600 s (filled symbols), resulting in different thicknesses from 12 to 18 nm. The samples were fabricated in co-deposition with the SHJ solar cells on a glass substrate.*

The electrical properties for each emitter layer of the fabricated SHJ solar cells are demonstrated in figure 4.4(a) (V_{OC} and FF) and figure 4.4(b) (J_{SC} and efficiency). As figure 4.3 suggests, the conductivity of the a-Si:H emitter layer improves from 2.1×10^{-7} to 5.9×10^{-5} S/cm by increasing the doping gas flow (from 0.5 to 32 sccm). The corresponding V_{OC} and FF also improve from 599 mV and 60% to 631 mV and 67% respectively. The improved FF is attributed to the reduced Schottky barrier at the ZnO:Al/emitter interface, which will be clarified later in this chapter.

The improved Voc could be attributed to the improved field effect passivation (improved electric field at the emitter/c-Si junction). To test this hypothesis, we measured the τ_{eff} of the solar cell precursors by means of the photoconductance decay technique. The injection level dependent τ_{eff} of the solar cell precursors is illustrated in figure 4.5. As shown in figure 4.5 τ_{eff} improves at low injection-levels of Δn demonstrates by increasing the doping gas flow. However, at high injection levels of Δn, τ_{eff} does not change. Owing to the fact that the effect of the field effect passivation is weighted at a low injection-level dependent τ_{eff} and the effect of the interface defect density (N_s) reduction is weighted at an entire injection-level dependent τ_{eff} [54,87] (section 3.5), we could attribute the improved τ_{eff} to the improved electric field.
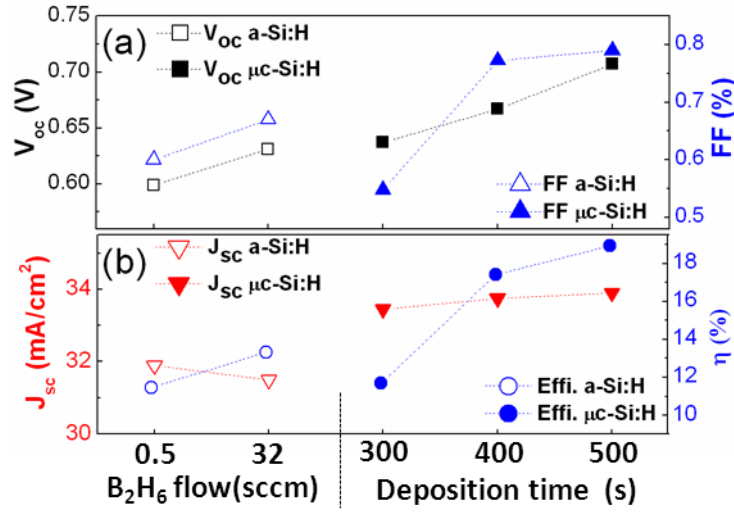
Figure 4.4: *The variation of (a) V_{oc} (open and filled squares) and FF (open and filled upward triangles) (b) J_{sc} (open and filled downward triangles) and efficiency (open and filled circles) for the SHJ solar cells fabricated on flat c-Si wafers with different p-a-Si:H and p-µc-Si:H emitter layer conductivities. The dashed lines are plotted to visualize the trend.*

Comparing the electrical properties of two SHJ solar cells deposited with low and high doped a-Si:H emitter layers, emphasizes the role of the electric field which needs to be satisfied by a sufficiently doped emitter. It should be mentioned that the highly doped a-Si:H layer (32 sccm of B_2H_6) is the optimized p-a-Si:H layer developed for a-Si:H single junction solar cell, resulting in state of the art V_{OC} (above 920 mV) in p-i-n thin film configuration [98]. Thus, the obtained V_{OC} with this p-type a-Si:H emitter layer is only 631 mV which is far below the state of the art value (above 700 mV) for SHJ solar cells.

It should be noted that the doping efficiency of a-Si:H layers are quite poor [99]. In addition, by introducing more doping in a-Si:H layer the dangling-bond density increases [100]. Therefore, a possibility to achieve higher emitter conductivity could be the fabrication of µc-Si:H emitter layers.

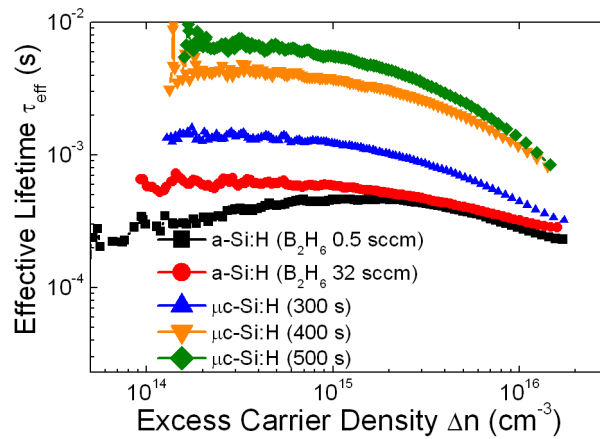

Figure 4.5: *The injection-level dependent effective lifetime for the solar cell precursors with different emitter conductivities, from lowly doped a-Si:H to highly conductive µc-Si:H, measured in the transient mode.*

4.3 μc-Si:H layers as emitter for SHJ solar cells

To satisfy the required emitter conductivity, we suggest to deposit μc-Si:H layers which allow higher conductivity levels compared to the a-Si:H counterpart. Figure 4.3 shows the conductivity of μc-Si:H layers, as a function of the deposition time in the range of 300-600 s (corresponding to the thickness range of ~12-19 nm). The deposition parameters of μc-Si:H emitter layers are shown in table 4.2.

Table 4.2: *The PECVD process parameters used for the deposition of the p-type μc-Si:H emitter layers.*

SiH_4 flow (sccm)	H_2 flow (sccm)	B_2H_6 (sccm)	Pressure (mbar)	Electrode distance (mm)	Power (W)	Temperature (°C)
3	1000	1	0.6	30-20	80	220

Figure 4.3 shows that the conductivity of the μc-Si:H layers significantly improves from 1.5×10^{-7} to 0.3 S/cm with depositing layers that are a few nanometer thicker (~7 nm thicker layers). The most common explanation for this behavior is the crystallinity evolution within the thickness. By depositing thicker films, larger grains form until they merge, giving a constant conductivity [101]. In fact, this μc-Si:H material property allows us to study the effect of the emitter conductivity without introducing any additional interrelated parameters. Comparing figure 4.2 and 4.3 suggests that a highly conductive μc-Si:H layer is achieved after the nucleation (formation of nanometer crystalline grain) phase. For the first 300 s, the conductivity of the μc-Si:H layer is $\sim1.5\times10^{-7}$ (S/cm), only. By increasing the deposition time to 500 s, a higher crystallinity is achieved (see the Raman spectra in figure 4.2). As a consequence, the conductivity significantly improves to 0.3 S/cm. This indicates that the initial a-Si:H phase (incubation phase) of the μc-Si:H film almost does not contribute to the total conductivity of the film. Hence, in order to successfully employ the μc-Si:H emitter layers in the SHJ solar cell structure, it is important to achieve a fast nucleation. As the emitter should be as thin as possible, the PECVD process parameters need to be precisely optimized to achieve the fast nucleation.

One of the PECVD process parameters, which has a significant effect on the crystallinity of the film (and hence conductivity), is the deposition pressure. Indeed, by decreasing the pressure, a faster nucleation takes place and a higher crystallinity is achieved. Figure 4.6 shows the crystallinity fraction of 5 nm a-Si:H and ~15 nm p-type μc-Si:H stack layers deposited at different pressures (0.6-3 mbar). The Raman crystallinity fraction increases from 0 to ~36% for samples that have been deposited at 3 and 0.6 mbar, respectively.
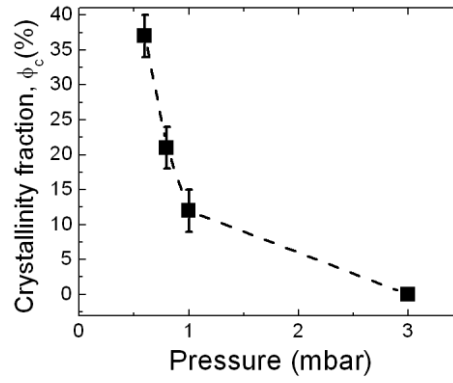
Figure 4.6: *The Raman crystallinity fraction (Φ_C) of 5 nm a-Si:H and ~15 nm p-type µc-SiH stack layers deposited at different pressures (0.6-3 mbar)where the deposition at lower pressures increases the crystalinity fraction.*

Although, decreasing the deposition pressure could speed up the nucleation and result in a higher crystallinity fraction films, the ion bombardment increases at lower pressures [102-104]. Such an increased ion bombardment at low pressures could result in the etching condition, instead of deposition when using highly hydrogen diluted silane plasma [105]. Figure 4.7 (a) shows that the deposition and the etch regime can selectively be achieved by varying the pressure (for highly hydrogen diluted silane plasma). The other PECVD process parameters are reported in table 4.3.

Table 4.3: *PECVD process parameters used for highly hydrogen diluted silane plasma where by varying the deposition pressure, either the etch or the deposition regime could be achieved.*

SiH₄ flow (sccm)	H₂ flow (sccm)	Electrode distance (mm)	Power (W)	Temperature (°C)
3	800	20	30	200

Figure 4.7(b) presents an etched a-Si:H layer, exposed to highly hydrogen diluted silane plasma. A protective layer (in the center of the picture) which has protected that part of the sample against etching shows a different color. The etching with highly hydrogen diluted silane plasma at low pressure is attributed to the high ion bombardment (clarified later in this section) and also the chemical etching by hydrogen [105].

In order to confirm the ion bombardment at low pressures (for highly hydrogen diluted silane plasma), we have introduced a method to evaluate the intensity of the ion bombardment. Indeed, the c-Si substrate passivated with the a-Si:H layers acts like a sensitive sensor to the ion bombardment. By exposing such structure to the plasma, the lifetime variation could show the intensity of the ion bombardment. Figure 4.8 shows the measured injection level dependent τ_{eff} of the FZ c-Si wafer passivated by 27 nm intrinsic a-Si:H after different treatments. The τ_{eff} ($\Delta n = 10^{15}$ cm^{-3}) immediately after deposition is ~60 µs. After post-deposition annealing (190°C, 60 min, ambient air), the τ_{eff} reaches up to ~1.18 ms. However, by exposing the sample to highly hydrogen silane diluted plasma, the lifetime drops to ~219 µs.
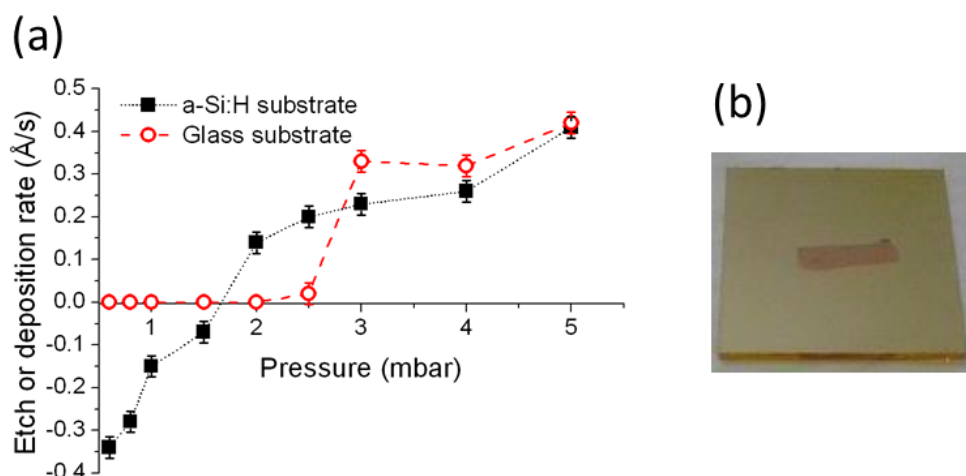
Figure 4.7: (a) *The etch or deposition regime in the highly hydrogen diluted silane plasma could be selected by varying the pressure. The negative values represent the etch region; the positive values refer to the deposition region. The black symbols show the data obtained for the a-Si:H substrates. The open red symbols show the deposition rate on the glass substrate. The lines are introduced to guide the eye. (b) A picture of a-Si:H substrate which has been etched by highly hydrogen diluted silane plasma at 0.6 mbar. A protective layer in the center has protected the very part of the sample against etching where other parts have been etched.*

This trend could be explained by introducing dangling bonds into the a-Si:H network where by re-annealing the lifetime is recovered (see red data points in figure 4.8). We measured a lifetime of ~1.52 ms after exposure to plasma and the re-annealing step. It should be noted that by exposing the sample to highly hydrogen diluted silane plasma, most probably the hydrogen content in the a-Si:H network increases [29]. This might explain the higher lifetime (1.52 vs. 1.18 ms) after the re-annealing most likely due to the penetration of hydrogen atoms into the a-Si:H/c-Si interface [29].

As shown in figure 4.8, the lifetime degradation due to the ion bombardment, is totally reversible. These results indicate that the increased ion bombardment by deposition at lower pressure (in order to speed up the nucleation step) is not detrimental for the final passivation. If guaranteed that the low pressure highly hydrogen diluted silane plasma does not etch the passivation layer, such plasma could be used for the deposition of the µc-Si:H emitter.

SHJ solar cells with p-type µc-Si:H emitter layers which are similar thick as a-Si:H emitter layers (~15 nm) were fabricated by means of fast nucleation due to low deposition pressures (~0.6 mbar). The electrical properties of the fabricated SHJ solar cells with the µc-Si:H emitter layer deposited with different deposition times (300-500 s, corresponding to thickness variation of ~12-17 nm) are demonstrated in figure 4.4. As this figure suggests, the FF increases from 54.8% (300 s sample) to 79% (500 s sample) by improving the conductivity of the µc-Si:H emitter layers (see figure 4.3). The improved FF is attributed to the reduced Schottky barrier height (clarified later in this chapter) and the reduced contact resistance at the emitter/TCO interface [106,107]. Compared to ITO, the effect of the contact resistance is more pronounced for the ZnO:Al layer, as a highly resistive incubation layer forms in the initial phase of the ZnO:Al growth [108]. Such a phase does not exist neither for ITO material nor for p-i-n thin film configuration, as the p-layer is deposited on well-formed crystal gains of the ZnO:Al layers.
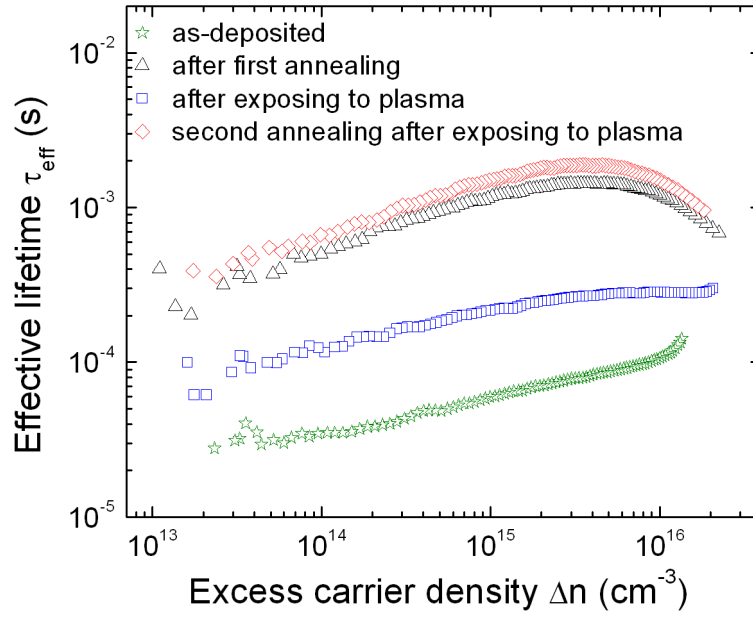
Figure 4.8: *The injection level dependent τ_{eff} of the c-Si wafer passivated with 27 nm intrinsic a-Si:H layers after different treatments. Green stars show the as-deposited lifetime, black triangles show the lifetime after post-deposition annealing (190°C, 60 min, ambient air), blue squares show the lifetime after exposing the sample to highly hydrogen diluted silane plasma at 4mbar (other process parameters were reported in table 4.3) and red diamonds show the lifetime after re-annealing and exposing to plasma . The higher achieved τ_{eff} after the re-annealing compared to the lifetime after the first annealing, indicates that the damage created, due to the exposure to highly hydrogen diluted plasma is reversible.*

Figure 4.4 (a) shows that by improving the conductivity of the µc-Si:H layers, the Voc value increases. The V_{OC} of 667 and 707 mV were measured for the µc-Si:H emitter layers deposited for 400 and 500 s respectively. The V_{OC} improved by deposition of the µc-Si:H emitter layers (in comparison to the a-Si:H counterpart) is attributed to the improved field effect passivation (higher electric field at the emitter/c-Si interface) and reduction in interface defect density. It should be mentioned that at the V_{OC} condition (i.e. high injection level) the effect of the reduced interface defect density is much more significant compared to the improved field effect passivation.

Figure 4.5 shows that higher τ_{eff} were measured at a low injection-level for both µc-Si:H emitter layers with higher conductivity (samples deposited for 400 and 500 s) compared to the µc-Si:H sample deposited for 300 s. This improvement (at a low injection level) is attributed to the improved electric field as all the µc-Si:H layers were deposited with the same recipe but different deposition times. The maximum τ_{eff} (at a low injection level) is achieved for the emitter layer with the maximum conductivity (500 s deposition time).

Apart from the field effect passivation, which is achieved by deposition of higher conductive µc-Si:H emitter layers, the improved V_{OC} (for SHJ solar cells with µc-Si:H emitter) is more related to the reduced interface defect density by improving the passivation at the a-Si:H/c-Si interface. The hydrogen plasma treatment to enhance the passivation at the a-Si:H/c-Si interface has attracted attention. Recent studies [29,84] have shown that the hydrogen plasma treatment can shift the bulk of an intrinsic a-Si:H film to the amorphous-to-crystalline transition regime where the device-grade a-Si:H material could be produced [68]. Indeed, in highly hydrogen diluted silane plasma (condition that silane concentration is below

6% [109]), as well as for the fabrication of the µc-Si:H films, by means of the layer-by-layer deposition technique [110], it has been observed that within the first few seconds (50 s) after the plasma ignition [110], the hydrogen concentration drastically decreases while a hydrogen-rich sub-layer forms simultaneously [111]. The diffusion of hydrogen from this saturated hydrogen sub-layer to the a-Si:H/c-Si has been confirmed by the deuterium treatment and secondary-ion-mass spectroscopy [29,112]. It should be noted that an atomically sharp a-Si:H/c-Si interface is required to obtain a high-quality interface passivation, [70]. In fact, the a-Si:H passivation layer prevents the detrimental epitaxial growth of the samples that were exposed to highly hydrogen diluted silane plasma for the deposition of the µc-Si:H emitter layer. Similar results have also been reported for hydrogen plasma treatment [112].

Figure 4.5 indicates that considerable improvement in τ_{eff} for the samples with µc-Si:H emitter layers has been observed not only at a low injection-level but also at medium and high injection-levels of the excess carrier density. Owing to the fact that the interface defect density affects the τ_{eff} at all injection-levels [50], we could attribute the improved V_{OC} (by deposition of µc-Si:H emitter layer) to the reduced interface defect density. Interestingly, both samples with a-Si:H emitter layers have similar τ_{eff} at medium and high injection-levels of Δn. Compared to the highly doped a-Si:H emitter layer sample, the improved τ_{eff} at all injection-levels for the µc-Si:H emitter layer deposited for 300 s with the lower conductivity indicates that the interface defect density has been reduced (after deposition of the µc-Si:H layer). The reduced interface defect density well explains the similarly measured V_{OC} values for these two samples (highly doped a-Si:H and 300 s µc-Si:H) with more than two orders of magnitude difference in the emitter conductivity values.

The improved passivation at the a-Si:H/c-Si interface by deposition of the µc-Si:H emitter layers suggests that an extra step of hydrogen plasma treatment can be avoided. It should be noted that not well-optimized hydrogen plasma treatment could result in etching of the buffer layer and adversely affect the passivation quality [105,112].

4.4 Schottky barrier at ZnO:Al/p-type emitter

As mentioned in section 4.1, the lateral conductivity of the a-Si:H and µc-Si:H layers is quite poor compared to the c-Si counterpart. Consequently, a TCO layer (often an n-type semiconductor) should be deposited to improve the charge transport to the device contact metal grid. Due to the lower work function of the TCO material (than p-a-Si:H and p-µc-Si:H emitter layers) [113], a Schottky barrier forms at the TCO/ p-type emitter interface. The barrier height, which is governed by the work function mismatch between the TCO and the emitter, plays a critical role on the performance of the fabricated devices [114-117]. Indeed, the barrier height has a significant effect on the hole collection and the FF value [115]. In case of a large work function mismatch (lowly doped emitter and low work function TCO such as (ZnO:Al)), the whole p-layer is driven into depletion and the V_{OC} is affected, as well [117]. The schematic illustration in figure 4.9 shows the Schottky barrier between the p-type a-Si:H and the TCO layer.
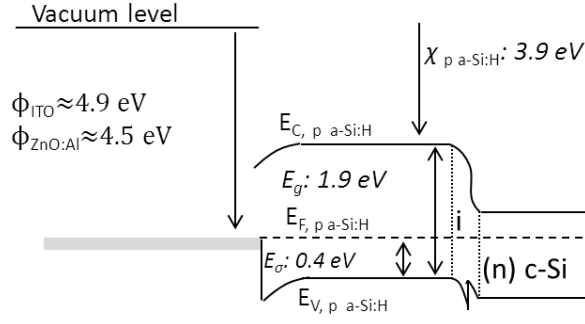
Figure 4.9: *Schematic band diagram of the Schottky barrier at the p-type a-Si:H/TCO interface.*

ITO is the most commonly used TCO material in the SHJ solar cell structure, [92] which has a work function of ~4.9 eV [113,118]. Considering an electron affinity of ~3.9 eV for a-Si:H ($\chi_{a-Si:H}$) [119] with a E_g of a-Si:H ($E_{g\,a-Si:H}$)1.85-1.9 eV and a typical activation energy ($E_{\sigma\,a-Si:H}$) of ~400 meV, the TCO requires a work function of ~5.4eV in order to form an ohmic contact at the p-type a-Si:H/TCO interface ($\Phi_{p\,a-Si:H} = \chi_{a-Si:H} + E_{ga-Si:H} - E_{\sigma\,a-Si:H} = 5.4$ eV). Thus, the ITO/p-a-Si:H junction has a Schottky barrier with a height of ~0.5 eV (barrier height = $\Phi_{p\,a-Si:H} - \Phi_{ITO} = 0.5$ eV). By replacing the ITO with the DC sputtered ZnO:Al layer, which has a lower work function of 4.5 eV [113], the barrier height increases to 0.9 eV (barrier height = $\Phi_{p\,a-Si:H} - \Phi_{ZnO:Al} = 0.9$ eV). Due to the increased Schottky barrier, S shape I-V curves with low FF values are obtained.

It should be noted that in order to replace ITO by another material in order to develop a new TCO for SHJ solar cells, the effect of the work function should be highly considered since no high FF could be obtained with p-type a-Si:H emitter layer without satisfying the required work function. However, as demonstrated in section 4.2 and 4.3, a much more conductive emitter could be achieved by using p-type µc-Si:H material. Moreover, the µc-Si:H material offers a better contact resistance to the ZnO:Al layer [106]. Additionally, it has been demonstrated that a double p-layer structure with µc-Si:H at the interface to the TCO is less sensitive to the front TCO work function (for n-i-p thin film solar cells where a n-type TCO is deposited on a p-type emitter layer similarly to the SHJ solar cells) [120]. It should be noted that as nucleation phase (in the growth of µc-Si:H films) takes place spontaneously, several parallel Schottky junctions could form laterally at the ZnO:Al/p-type µc-Si:H interface. Effectively, the dominant Schottky junction is the lowest Schottky barrier [121].

The electron affinity, the E_g and the activation energy of the doped µc-Si:H are ~4.05, 1.12 and 0.03 eV respectively [122]. Following the same procedure, as we did for calculating the Schottky barrier height for the p-type a-Si:H emitter, results in a work function of ~5.14 eV for the p-type µc-Si:H material ($\Phi_{\mu c-Si:H} = \chi_{\mu c-Si:H} + E_{g\,\mu c-Si:H} - E_{\sigma\,\mu c-Si:H} = 5.14$ eV) and a Schottky barrier height of ~0.64 eV with the ZnO:Al layer (barrier height = $\Phi_{p\,\mu c-Si:H} - \Phi_{ZnO:Al} = 0.64$ eV) which is much lower than the barrier with the a-Si:H emitter layer (0.9 eV).

In practice, the influence of Schottky junction could be observed in the illumination-dependent V_{OC} measurement, performed at high illumination intensities by means of the Suns-V_{OC} setup [123]. The Schottky junction which could be modeled as a Schottky diode parallel to a shunt resistor[124] is demonstrated in figure 4.10.
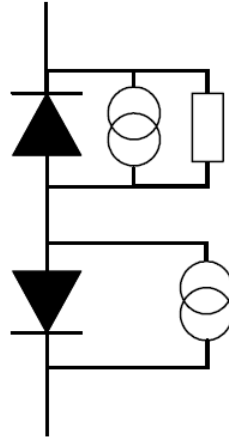
Figure 4.10: *The schematic illustration of the Schottky junction at the TCO/emitter interface modeled with a Schottky diode parallel to a shunt resistor. The p-n junction at the emitter/c-Si is illustrated with opposite diode, as well [139].*

At low illumination densities, the Schottky diode is fully shunted by the resistor. However, at high illumination densities, the Schottky diode cannot be shunted anymore. As a consequence, it generates a voltage opposite to the p-n junction [124]. Therefore, the measured V_{OC} decreases and a reversal in the Suns-V_{OC} curve can be observed (i.e. the voltage decreases with increasing illumination density). The illumination at which the reversal point is reached, is a good parameter to compare the influence of the Schottky barrier [124].
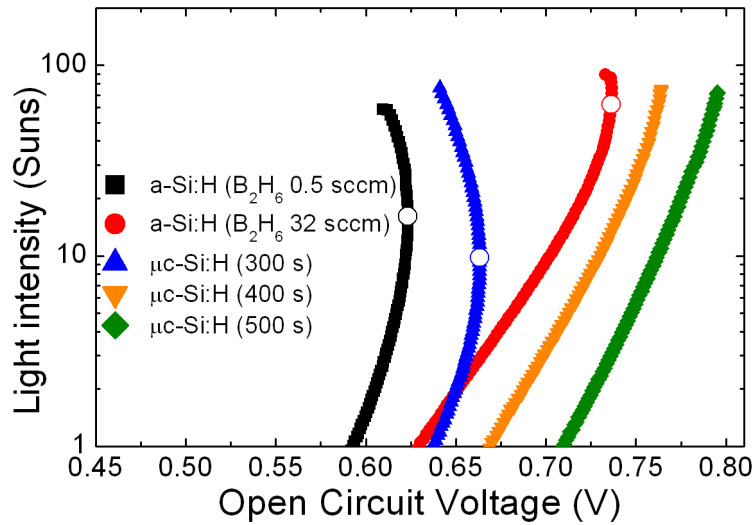
Figure 4.11: *The measured Suns-V_{OC} characteristics of the SHJ solar cells with different p-type a-Si:H and µc-Si:H emitter layers.*

Figure 4.11 shows the Suns-V_{OC} characteristics of the SHJ solar cells fabricated with different p-type a-Si:H and µc-Si:H emitter layers. The electrical parameters were shown in figure 4.4 (a) and (b). As indicated by figure 4.11, increasing the emitter conductivity shifts the reversal point (open symbols in figure 4.11) to higher illumination densities. The reversal points of the two SHJ solar cells using either a lowly doped a-Si:H emitter layer (0.5 sccm B_2H_6) or a µc-Si:H emitter layer (deposited for 300 s) are observed at ~16 and 9.7 suns respectively. The I-V curve of both samples show S shape characteristics and their FF values are low (60% for the lowly doped a-Si:H emitter and 54.8% for the low conductive µc-Si:H emitter layer). The reversal point shifts to 62 suns for the highly doped a-Si:H emitter layer

(FF reaches to 67 %). The reversal point is located at much higher suns for the highly conductive emitters (µc-Si emitter with 400 and 500 s deposition time) and V_{OC} value is not reduced until the maximum investigated illumination density (74 suns) as been reached. Consequently, the high FF of 77.3 and 78.9% is achieved for the µc-Si:H emitter samples with 400 and 500 s deposition time respectively. It should be highlighted that the FF is not only limited by the Schottky barrier at the TCO/emitter interface but also the valence band-offset between i a-Si:H and c-Si plays a role.

The high FF obtained by the ZnO:Al layer which has a much lower work function than ITO, clearly shows that the lower work function of this material is not an obstacle for being used as a TCO for the SHJ solar cell structure. By implementing a well-doped emitter, the higher Schottky barrier at the ZnO:Al/emitter interface compared to the ITO/emitter could be suppressed and the low cost ZnO:Al material could be used as an alternative TCO for SHJ solar cells [125]. The effect of the DC sputtered ZnO:Al deposition parameter on the electrical properties of the SHJ solar cells is addressed in next chapter (chapter 5).

4.5 Reduced emitter absorption

So far, we have shown that employing the µc-Si layer can satisfy the required emitter doping level to obtain well-functioning SHJ solar cells. This allows us the use of low cost and more environmental friendly TCO material such as ZnO:Al. As demonstrated in figure 4.2 and 4.3, a highly conductive µc-Si:H layer can only be reached after a nucleation phase that takes place spontaneously. This means that a few nanometer thicker p-type µc-Si:H layer might be needed compared to the p-type a-Si:H layer counterpart. As the µc-Si:H material is an indirect E_g material and has a much lower absorption coefficient (particularly in the blue and the green internal wavelengths), than the a-Si:H counterpart (see figure 2.2) the J_{SC} will not be affected. As demonstrated by figure 4.4, a higher J_{SC} (~1.9 mA/cm^2) is achieved for the SHJ solar cells with µc-Si:H emitter layers compared to the a-Si:H layers.
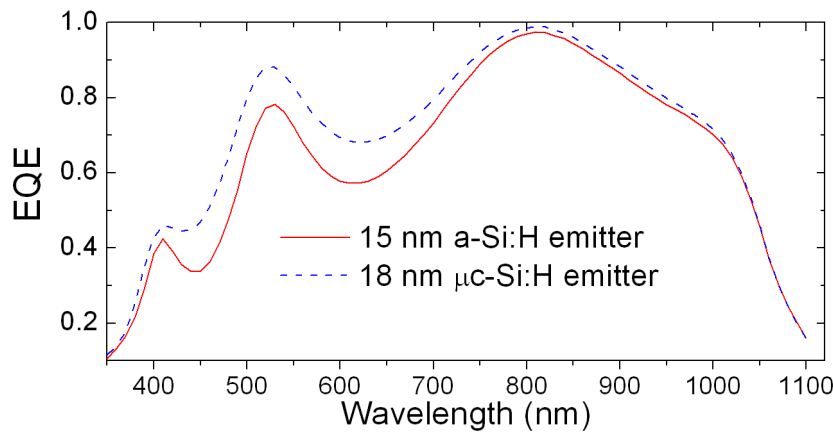
Figure 4.12: *The measured EQE curves for the SHJ solar cell with a 15 nm p-type a-Si:H emitter (red solid line) and an 18 nm p-type µc-Si:H emitter (blue dashed line), indicates an 1.9 mA/cm^2 gain in J_{SC} due to the reduced absorption in blue and green internal wavelengths. Interference fringes form because of the flat DC sputtered ZnO:Al TCO layer (320 nm) and untextured c-Si substrate.*

Figure 4.12 shows the measured EQE curves for the SHJ solar cells with a 15 nm (B$_2$H$_6$: 32 sccm) a-Si:H layer thickness and an 18 nm (500 s deposition time) µc-Si:H emitter layer

thickness. The results indicate that the EQE signal in the blue and green internal wavelength for SHJ solar cells, fabricated with the μc-Si:H emitter layer, has improved. This improved EQE value could be attributed to the reduced absorption in the emitter layer due to the lower absorption coefficient of the μc-Si:H compared to the a-Si:H layer (see figure 2.2).

Moreover, it has been demonstrated that the hydrogen plasma treatment could widen the E_g of the a-Si:H layers [29,84]. The same effect could be expected with highly hydrogen diluted silane plasma, as pushing the valence band edge to lower energy levels (by increasing the hydrogen content of the film) is known to be responsible for the E_g widening [126]. As only 30% of the photogenerated carriers in the intrinsic a-Si:H passivation layer contribute to the J_{SC} [93], the improved J_{SC} could partly be related to the reduced absorption in the a-Si:H passivation layer due to the E_g widening. It should be mentioned that the interference fringes in the EQE signals (figure 4.12) appear as a result of the flat DC sputtered ZnO:Al layer (320 nm) and the flat c-Si substrate.

4.6 Conclusion on µc-Si:H layer for SHJ solar cells

The emitter layer plays several crucial roles in the SHJ solar cell structure such as providing a sufficient electric field (i.e. creation of an inversion region at the emitter/c-Si interface), adequate band bending in c-Si wafers and suppressing the Schottky barrier at the TCO/emitter interface (section 4.1). In section 4.2, the effect of the established electric field by the emitter layer on the performance of the SHJ solar cell was presented by varying the doping level of the a-Si:H emitter layers.

In section 4.3, we proposed µc-Si:H layers to achieve higher conductivity levels, compared to the a-Si:H counterpart. Our findings show that a low pressure plasma condition can be used to speed up the nucleation of the µc-Si:H emitter layer. Although, the ion bombardment increases by decreasing the deposition pressure (formation of more dangling bonds), this is not an issue for passivation since the degraded passivation could totally be recovered by a post-deposition annealing treatment. Furthermore, we studied the effect of the emitter conductivity on the performance of the SHJ solar cells through our novel approach which was varying the emitter conductivity by taking advantage of the improved conductivity due to the crystallinity evolution within the µc-Si:H layers. In addition, we demonstrate that by applying the µc-Si:H layers, the interface defect density at the a-Si:H/c-Si interface decreases and thus the passivation improves. This may allow to avoid an extra step of hydrogen plasma treatment.

Section 4.4 investigated the Schottky barrier at the ZnO:Al/emitter interface. Besides, it was shown that by fabricating µc-Si:H emitter layers, the high Schottky barrier can effectively be suppressed. This way, we demonstrated well-functioning SHJ solar cells with high FF (over 80%) and V_{OC} (above 700 mV) values by using ZnO:Al TCO instead of the commonly used ITO material.

Finally, the fabrication of SHJ solar cells with the µc-Si:H emitter layer showed higher EQE values and ~1.9 mA/cm^2 gain in J_{SC}, compared to a-Si:H counterpart due to the lower absorption coefficient of the µc-Si:H material (section 4.5).

Chapter 5

5 DC sputtered ZnO:Al, an alternative TCO for SHJ solar cells

This chapter firstly addresses the different roles of the TCO layer in the SHJ solar cell structure (section 5.1). Secondly, we introduce the DC sputtered ZnO:Al as an alternative TCO for SHJ solar cells and indicate the advantages, compared to the commonly used TCO material. The effect of ZnO:Al deposition parameters including power, temperature, oxygen flow and deposition time on the electrical properties of the obtained SHJ solar cells is presented in section 5.2. Finally, section 5.3 describes the influence of vertical transportation component of the ZnO:Al layer on the FF and its contribution to the total series resistance of the fabricated SHJ solar cells, using ZnO:Al/Ag/ZnO:Al multilayers to separate the lateral from the vertical conductivity.

5.1 The requirement for TCO in SHJ solar cells

The sheet resistance of the doped Si thin films; which form the emitter and BSF in the SHJ solar cell; is inferior (in the range of 100 KΩ/sq-10 MΩ/sq) compared to the highly doped c-Si emitter of diffused solar cells. Therefore, contacting the SHJ solar cells in the same way as the standard diffused c-Si solar cells, i.e. by direct fabrication of mm-spaced metal fingers (on the emitter), results in high series resistance losses and thus low FF values. The inclusion of the TCO layer before fabricating the metal grid significantly enhances the charge carrier collection and reduces the series resistance losses. The above mentioned argument imposes several requirements for the TCO layer, as follows:

(i) The TCO should simultaneously form a lossless contact to the emitter, the BSF layer, and the metal grid.

(ii) The TCO should be as transparent as possible over the absorption range of the c-Si absorber.

(iii) The TCO layer should act as an antireflection coating layer by refractive index-matching between the c-Si and air (finally Si and encapsulant in the solar module).

Sputtered ITO is the material of choice in order to simultaneously reach a low sheet resistance, a maximal optical transparency and the antireflection behavior. ITO is the most applied TCO for SHJ solar cells [92] due to its good optical and electrical properties [127,128].

For the front TCO, the ITO film with a thickness of ~80 nm could provide the desired lateral conductivity and satisfy the required sheet resistance (less than 80 Ω/sq). Additionally, such thickness acts as quarter-wavelength antireflection coating which is the destructive interference of two reflected beams with 180° phase difference, as shown in figure 5.1. As a general trend for c-Si solar cells, is to minimize the reflectivity at ~650 nm wavelength, where the maximum amount of incident solar energy can be converted into the output power. Thus, to take benefit of the quarter-wavelength antireflection coating at the wavelength of 650 nm, while considering that ITO has a refractive index of ~1.9 (at 650 nm wavelength), the thickness needs to be ~80 nm i.e. $\frac{1}{4} \times \frac{\lambda}{n} = d$, where λ, n and d, are the wavelength, the refractive index and the thickness, respectively. It should be mentioned that quarter-wavelength antireflection considers the reflectivity for a specific wavelength $\lambda(n_r,d)$ where at other wavelengths the reflectivity is still high. One way to minimize the reflection at overall wavelength is to texture the c-Si surface, what will be explained in section 5.2.1.1.
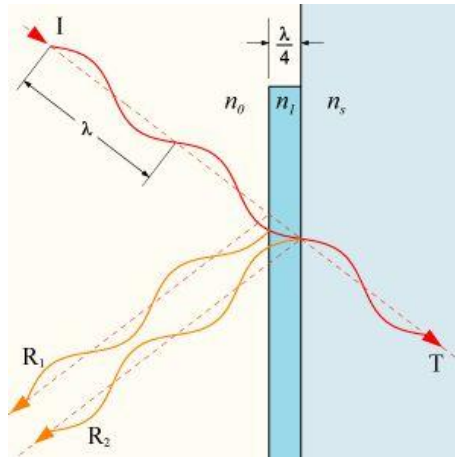
Figure 5.1: *The schematic illustration of the quarter wavelength antireflection coating where two reflected beams (with 180° phase difference) interfere destructively.*

On the one hand, a highly transparent TCO is required to maximize the photogeneration in the absorber in order to achieve high J_{SC} values. On the other hand, a low sheet resistance of TCO is highly important to minimize the series resistance losses and to maximize the FF. Generally, the conductivity σ (S/cm) of the TCO is calculated via equation 5.1,

$$\sigma = N \times \mu \times q \tag{5.1}$$

where N (cm^{-3}) is the free carrier density, μ (cm^2/Vs) is the free carrier mobility and q (C) is the electron charge. As a general trend to improve the conductivity is to increase the mobility instead of the free carrier density [129]. The reason for this is the free carrier absorption and reflection which take place in the near IR or mid-IR range [130]. To further increase the free

carrier mobility in the ITO, the use of hydrogen-doped In_2O_3 has been suggested which provides a high free carrier mobility of up to 120 (cm^2/Vs) and an excellent near-infrared-transparency [131].

Apart from the transparency and conductivity of the TCO (discussed in chapter 4), the TCO work function is another important parameter which is crucial for the performance of SHJ solar cells. The band alignment at the TCO/emitter interface significantly affects the carrier transport [117]. As practically all the TCO materials are n-type, an ohmic contact with n-type a-Si:H or μc-Si:H can easily be achieved. However, the condition is different for the p-type a-Si:H or μc-Si:H emitter layers, where the TCO/emitter interface must allow the efficient band to band tunneling. This means holes that are collected from the c-Si absorber into the p-type emitter layer must recombine with electrons from the TCO [132]. Among various TCO materials, ITO has one of the highest work functions in the range of 4.9-5.6 eV [113,120]. Moreover, appropriate band alignment between the ITO and p-type a-Si:H emitter layer has been demonstrated [92,120].

Nevertheless, ITO has several disadvantages. First of all, the cost of ITO is very high compared to the other TCO materials. Thus, replacing it by the cheaper TCO is one of the ways to reduce the production costs for SHJ solar cells. The second issue is the scarcity of indium (In). With a growing demand, the price will increase even more in the future [11]. In addition, it has been shown that In acts as a toxic element which could result into a toxic ITO compound [12]. Moreover, ITO lacks texturing capability what requires to combine it with the wafer texturing [133]. Therefore, replacing ITO with a cheaper, more abundant and environmental-friendly material including texturing capability seems to be a promising approach to reduce the costs of future SHJ solar cells.

5.2 The effect of ZnO:Al deposition parameters

As stated in section 5.1, replacing ITO with an alternative cheaper and more environmental-friendly material including texturing capabilities is a promising approach to improve future SHJ solar cells. Among the various TCO materials, ZnO:Al is an attractive candidate due to its good opto-electrical properties, the less environmental impact and its well-established technology with Si thin film solar cells [134-136].

During the last years, several deposition techniques such as pulsed laser deposition (PLD) [137], reactive DC sputtering [138,139], low pressure chemical vapor deposition (LPCVD) [140,141], as well as RF and DC magnetron sputtering have been used for fabricating ZnO films. The results of these studies show that the properties of the final films strongly depend on the deposition technique and the deposition parameters. Whereas by reactive DC sputtering 80 nm films with a sheet resistance below 75 Ω/sq can be fabricated [138], the DC magnetron sputtering with such a thickness produces a sheet resistance between 180-1600 Ω/sq, dependent on the flow of oxygen during the sputtering process [125,133]. Magnetron sputtering from an aluminum doped ZnO target is the mostly applied deposition technique for fabricating ZnO:Al layers. Therefore, it is mainly used in the large scale production [142].

Compared to the ITO material, the two main disadvantages of the ZnO:Al film are (i) the high resistivity (2-4×10^{-3} Ω.cm) [125] which is more than one order of magnitude higher than

ITO (5×10^{-4} Ω.cm) and (ii) the low work function (~4.3 eV for the ZnO:Al and ~5.1 eV for ITO). As for the second disadvantage, the high Schottky barrier at the ZnO:Al/emitter interface (ii), we proposed to use a µc-Si:H emitter layer since a higher conductivity can be achieved in comparison to the a-Si:H film. The successfully suppressed Schottky barrier at the ZnO:Al/emitter interface by employing an µc-Si:H emitter and other advantages of the µc-Si:H emitter layers were extensively discussed in chapter 4.

In order to address the first disadvantage (i), we have systematically studied the effect of the ZnO:Al deposition parameters on the opto-electrical properties of the individual ZnO:Al layers as well as the obtained SHJ solar cells. In particular, the effect of the layer thickness, oxygen flow, power density and temperature have been investigated. The main focus of this chapter is to understand the processes occurring by varying each deposition parameter in order to satisfy the required TCO properties for ZnO:Al layers.

5.2.1 Thickness effect

The resistivity of DC sputtered ZnO:Al films (1.3×10^{-3}Ω.cm) is much higher than the one of ITO (5×10^{-4}Ω.cm) [140,143,144]. The ZnO:Al films are polycrystalline material with a c-axis-preferred growth orientation (0002) perpendicular to the substrate [145,146]. Therefore, the structural properties of the ZnO:Al films suggest that an effective way to tune the resistivity is the thickness of the deposited films. In other words, the resistivity strongly depends on the deposited thickness since the formation of larger grains in a thicker film drastically decreases the resistivity [147,148].
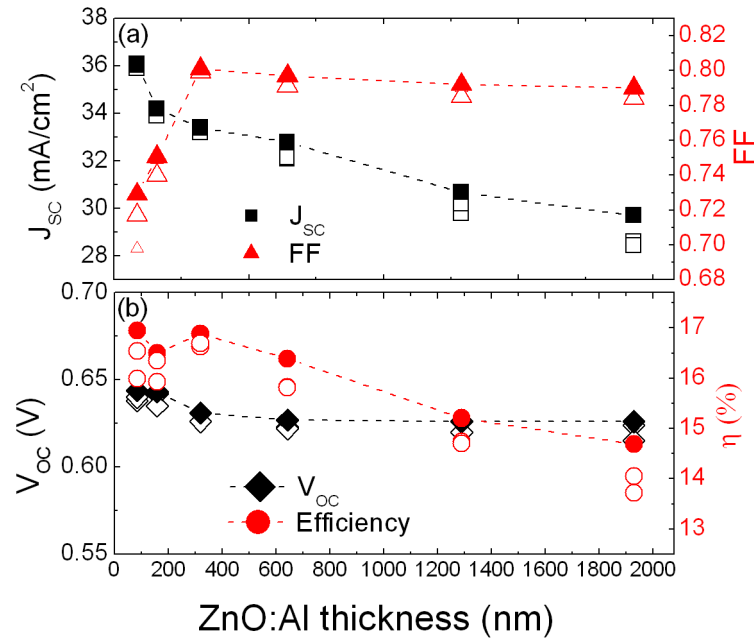
Figure 5.2: *The variation of (a) J_{SC} and FF (b) V_{OC} and η with respect to the ZnO:Al thickness. The ZnO:Al layers were deposited at a constant temperature (220°C), power density (1.9 W/cm2) and oxygen flow (0.5 sccm). For each thickness, the electrical properties of three cells are demonstrated (fabricated on the same substrate). The filled symbols represent the maximum value. The dashed lines connect the maximum measured values and are plotted to visualize the trend.*

Figure 5.2(a) shows the variation of the FF and J_{SC} values of SHJ solar cells with respect to the front contact thickness of the ZnO:Al layer, varied in the range of 80-1930 nm. Three data points (on the same substrate) are shown for each thickness and the maximum value is depicted by the filled symbol. Overall, the measured data points for each thickness are rather similar what indicates the uniformity of the fabricated devices. Figure 5.2(a) suggests a tradeoff between the J_{SC} and the FF. For the 85 nm ZnO:Al layer thickness (the common ITO thickness), the maximum FF value is 72.9 %. By increasing the TCO thickness (up to 320 nm), the FF significantly improves to 80.1 % due to the reduction in the resistivity of the TCO (see figure 5.4). On the other hand, figure 5.2 (a) shows that by increasing the ZnO:Al layer thickness, the J_{SC} reduces from 36.09 mA/cm^2 for 85 nm layer thickness to 29.7 mA/cm^2 for 1.9 µm layer thickness. To understand the J_{SC} reduction in case of thicker ZnO:Al layers, we studied the EQE and the absorption spectra of theses samples. As depicted in figure 5.3, the free carrier absorption is the main reason for the J_{SC} reduction especially in the wavelength range of 700-1100 nm.
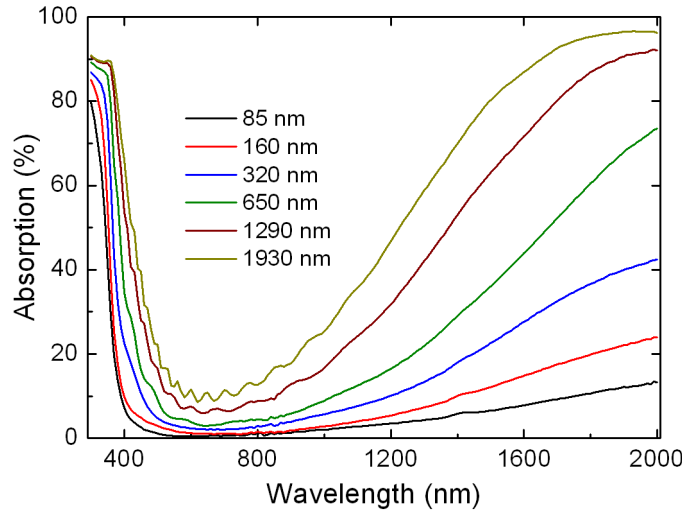
Figure 5.3: *The absorption spectra for ZnO:Al layers with different thicknesses deposited on glass in co-deposition with the front TCO of the SHJ solar cells. The absorption increases particularly in IR with the thickness increase.*

Figure 5.4 demonstrates the Hall measurement results, performed on the single ZnO:Al layer on glass. As this figure suggests the improved mobility (red triangles) is the main reason for the resistivity reduction due to the formation of larger ZnO:Al grains [148]. The carrier density seems to be almost constant for all thicknesses. Comparing figure 5.2 (a) and figure 5.4, it is observed that, although, the resistivity still decreases for the layers thicker than 320 nm, the FF values does not improve. This implies that for the TCO layers thicker than 320 nm, the TCO resistivity does not play a role in the total series resistance of the fabricated SHJ solar cells. Hence, the optimum ZnO:Al layer thickness regarding the series resistance in the cell is ~320 nm. It is to be considered that the electrical values measured for the ZnO:Al films on glass substrates should be treated as effective values due to the film inhomogeneity (presence of the incubation layer in the first few nm thickness of ZnO:Al films).
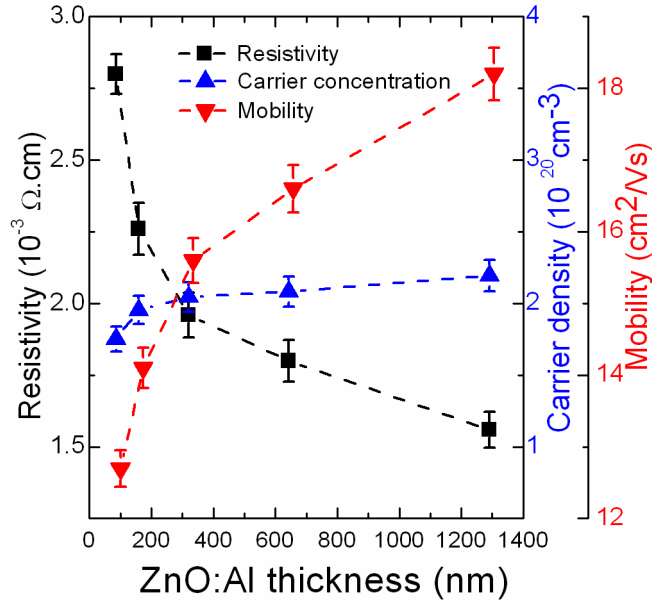
Figure 5.4: *The variation of resistivity, carrier concentration and mobility with respect to the ZnO:Al thickness. The ZnO:Al layers were deposited at a constant temperature (220°C), power density (1.9 W/cm^2) and oxygen flow (0.5 sccm) on glass substrate in co-deposition with SHJ solar cells. The dashed lines are plotted to visualize the trend. The values reported here should be treated as effective values due to the film inhomogeneity.*

Figure 5.2(b) demonstrates the variation of the VOC and the efficiency values with respect to the front ZnO:Al layer thickness. The highest efficiency is obtained for SHJ solar cells with a front electrode thickness of 85 nm (16.94 %) and 320 nm (16.88 %). For the TCO sample with a thickness of 85 nm, the high efficiency is governed by the high JSC, while the improved FF is responsible for the high efficiency of the TCO of 320 nm thickness. The similar efficiency values for these two thicknesses (85 and 320 nm) might suggest that the optimum thickness for the sputtered ZnO:Al is similar to ITO (~85 nm). However, it should be noted that a further efficiency improvement for these thin layers introduces several challenges since further reduction of the resistivity is limited by the material nature. On the other hand, by depositing a thicker TCO layer, the required conductivity is achieved. Moreover, there are several ways to suppress the free carrier absorption (caused by the thick layers) such as tuning the oxygen pressure during sputtering. Additionally, the deposition of thicker layers enables the chemical texturing of the ZnO:Al films, in contrast to the ITO material.

5.2.1.1 Texturing capability of ZnO:Al

One of the advantages of ZnO:Al material (compared to ITO) is its texturing capability. The well-known chemical texturing of the ZnO:Al could provide additional light trapping in the SHJ solar cells. Figure 5.5 shows the EQE of the fabricated SHJ solar cell with 1.3 μm ZnO:Al layer thickness before and after 25 s texturing with 1% HF aqueous solution. The thickness of the ZnO:Al, removed during this etching process is ~160 nm. As presented in figure 5.5, the interference fringes of the flat ZnO:Al layer vanish after the texturing process. Also, after texturing a gain of ~2.9 mA/cm^2 is achieved in the J$_{SC}$ due to the reduced

reflection by texturing. Figure 5.6(a) and (b) demonstrate the SEM micrographs of ZnO:Al layer in the SHJ structure before and after texturing, respectively.
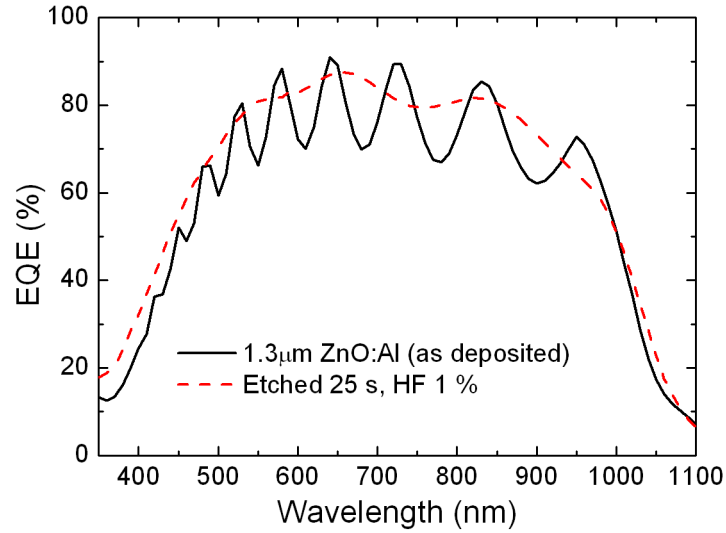
Figure 5.5: *The measured EQE for a SHJ solar cell before (black solid line) and after texturing the front ZnO:Al layer (red dotted line) in HF solution (1%) for 25 s where 2.9 mA/cm² gain was achieved after the texturing process.*
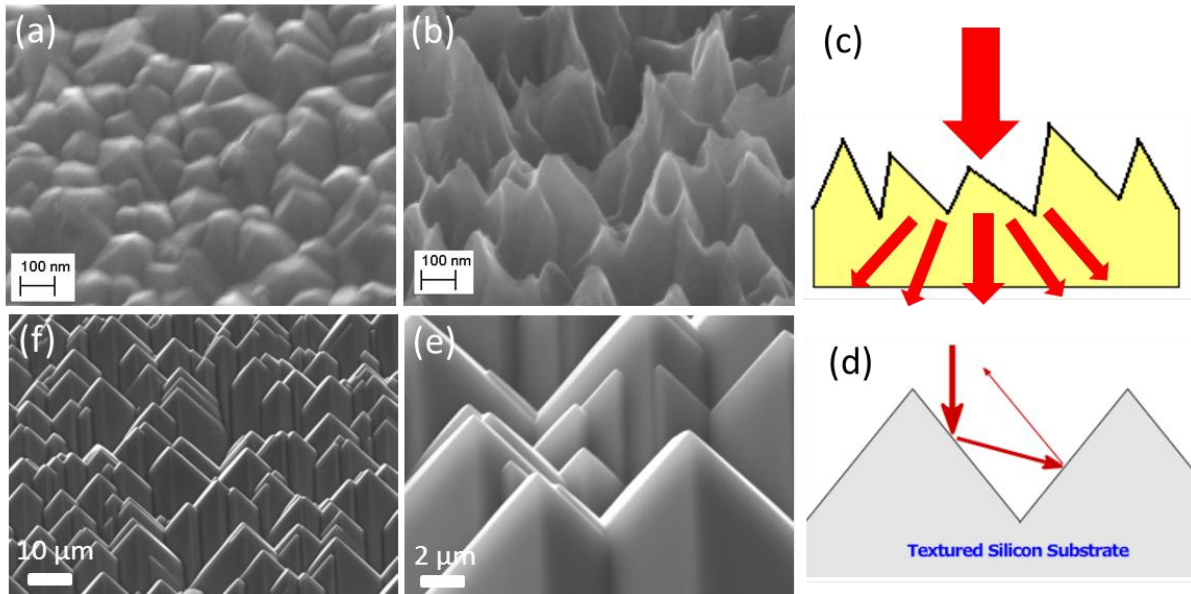
Figure 5.6: *The 45° tilted view SEM micrographs of surface of the ZnO:Al layer in the cell structure (a) before and (b) after the texturing process in HF (1%) for 25 s. The etched thickness is about 160 nm. Schematic illustrations of (c) light randomization by the textured surface (d) reduced reflection on textured c-Si due to the possibility of second refraction. This means that the reflected light can strike the silicon surface again. The reflectivity of bare c-Si reduces from about 35% to around 12% (~(35%)²) for the textured surface. (e) and (f) 45° tilted view SEM micrographs of surface of the textured c-Si with KOH solution.*

It is be highlighted that the mechanism of reflection reduction by chemical texturing of the ZnO:Al is different from random pyramids texturing of the c-Si substrates. In random pyramids texturing of c-Si substrates, the reflection reduces due to the possibility of having a

second refraction (the reflected light can strike the silicon surface again) [149]. Whereas, in case of chemical texturing of the ZnO:Al layers, the reduced reflection is governed by the enhanced scattering due to light randomization with a rough surface [150,151]. As the HIT technology is progressing toward thinner wafers, the light confinement becomes important. Therefore, the texturing capability of the ZnO:Al layers makes this material an even more attractive TCO candidate which could compensate in the J_{SC} reduction by using thinner wafers.

5.2.2 Oxygen flow effect

The opto-electrical properties of the ZnO:Al layers strongly depend on the oxygen content of the deposited layer. Hence, the oxygen pressure during the sputtering process is an effective parameter to tune the transparency and conductivity of the obtained layers. In fact, the oxygen vacancies in the ZnO:Al layers act as donor-type doping [152]. Therefore, low oxygen-content ZnO:Al layers suffer from poor transparency due to the high free carrier absorption. In contrast, oversupply of oxygen results in a formation of films with low conductivity and improved transparency resulting from the increased inactive Al dopant (by incorporation as Al_2O_3) and the reduction of oxygen vacancies [153].
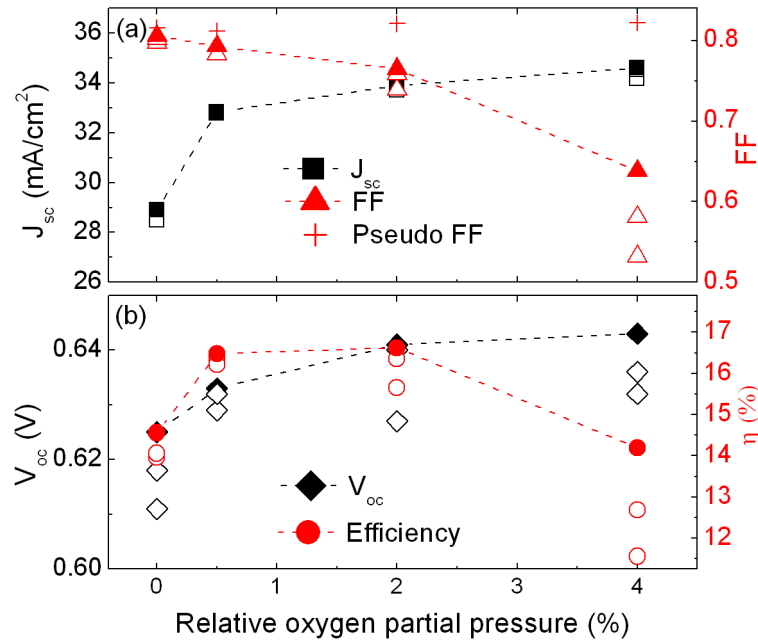
Figure 5.7: *The variation of (a) J_{SC}, FF and pseudo FF (b) V_{OC} and η with respect to the relative oxygen partial pressure. The ZnO:Al layers (~300 nm) were deposited at constant temperature (220°C) and power density (1.9 W/cm^2). In (a) and (b), for each thickness, the electrical properties of three cells are demonstrated (fabricated on the same substrate). The filled symbols represent the maximum value. The dashed lines connect the maximum measured values and are plotted to visualize the trend.*

Figure 5.7(a) and (b) show the variation of the J_{SC}, the FF, the V_{OC} and the efficiency of the SHJ solar cells as a function of the relative oxygen partial pressure. For each oxygen partial pressure, the electrical properties of three cells (on the same substrate) are reported and the

maximum is shown by filled symbols. As illustrated in figure 5.7(a) a tradeoff between the J_{SC} and the FF is observed whereby increasing the oxygen partial pressure, the J_{SC} increases and the FF decreases.
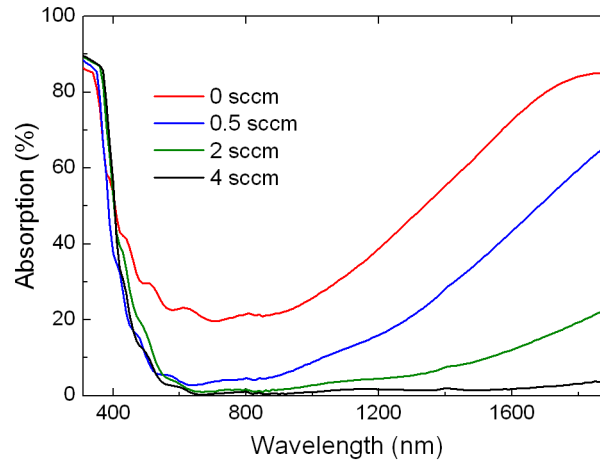
Figure 5.8: *The Absorption spectra of the single ZnO:Al layer deposited on the glass substrates with four different oxygen flows. The respective red, blue, green and black solid lines show the measured spectra for 0, 0.5, 2 and 4 sccm oxygen flows.*

Figure 5.8 shows that, the increased J_{SC} values are related to the reduced absorption of the ZnO:Al layers whereby an overall reduction in the absorption spectrum is observed when increasing the oxygen flow from 0 to 0.5 sccm. By further increasing the oxygen flow, the reduced absorption mainly occurs in the infrared (IR) part of the spectrum, what indicates a reduction in the free carrier concentration [130]. On the other hand, figure 5.7(a) suggests that the FF reduces in samples that have been deposited with higher oxygen partial pressures. The measured pseudo-FF values by Suns-V_{OC} (red crosses) are demonstrated in figure 5.7(a) as well. No significant variation has been observed in the pseudo-FF what suggests that the main reason for the FF reduction is the increased series resistance.

To understand the origin of the reduced conductivity (as a result of the increased O_2 flow), a Hall measurement has been performed. Figure 5.9 shows the variation in the resistivity, the carrier concentration, and the Hall mobility of the individual ZnO:Al layers (deposited on the glass substrates) with respect to the relative oxygen partial pressure in co-deposition with the SHJ solar cells. As indicated by figure 5.9, the increased resistivity of the ZnO:Al layers is related to the reduction in both; the mobility and the carrier concentration. The carrier density reduction has been the subject of several studies and has been associated to three reasons including (1) a lower oxygen vacancy concentration, due to increase in the oxygen flow [130,152-154], (2) an increase in the inactivate Al dopants by formation of the Al_2O_3 compound [155] and (3) the reduction of the interstitial zinc atoms [156]. Apart from the free carrier density reduction, due to the increased oxygen flow, the mobility reduces from 15.8 to 0.6 cm^2/Vs as illustrated in figure 5.9. The mobility reduction is attributed to two electron scattering mechanisms. One is imposed by the grain boundaries (formation of smaller grain by increasing the oxygen flow) [157-159]. The other one originates from the increased Al_2O_3 compound concentration. The higher inactive Al concentration in the layer (either by deposition from a highly doped target or by a higher oxygen flow in the plasma which increases the formation of more Al_2O_3 compound) results in higher scattering and hence lower mobility [155,160,161]. In addition, based on the Petritz model, the deposition at the higher

oxygen flow increases the oxygen chemisorptions in the grain boundaries and hence, reduces the carrier mobility [160,162,163].
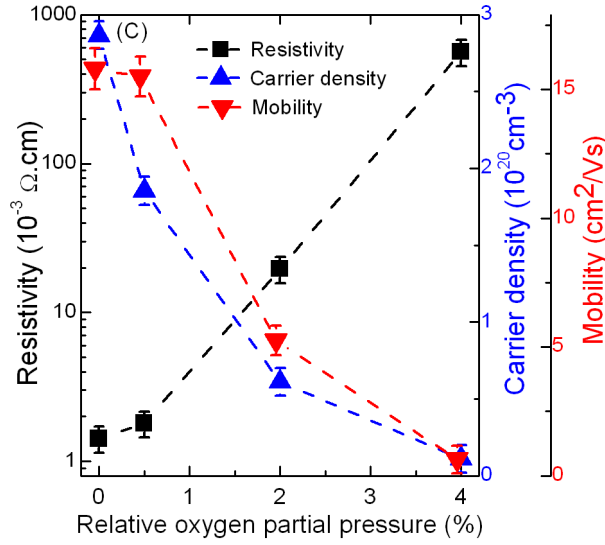

Figure 5.9: *The variation of resistivity, carrier density and mobility with respect to the relative oxygen partial pressure. The dashed lines are plotted to visualize the trend. The values reported here should be treated as effective values due to the film inhomogeneity.*

Figure 5.7 shows that by increasing the oxygen flow, the V_{OC} continuously improves from 0.625 V to 0.643 V for the respective oxygen flows of 0 and 4 sccm. Since it has been demonstrated that sputtering at higher oxygen flow increases the work function of the deposited layers and results in a higher V_{OC} [113,120,153], the gain in the V_{OC} could be attributed to the higher work function of the obtained ZnO:Al layers at higher oxygen partial pressures [120]. It is to be mentioned that since our µc-Si:H emitter layers are highly doped, it is expected that the effect of the TCO work function on the obtained V_{OC} be lower than the reported value for the n-i-p solar cells [120]. Furthermore, a higher photogenerated charge carrier concentration is expected, due to the reduced TCO absorption with higher oxygen flow, which results in a higher splitting in the quasi Fermi level as well as in a higher V_{OC}.

The efficiency results of figure 5.7 indicate that the deposition at 0.5 and 2 sccm oxygen flows results in the highest efficiency of 16.4 and 16.6 % respectively. Although, these two data points show very similar efficiencies, their efficiency factors are different. In case of the 2 sccm oxygen flow, the improved J_{SC} and slightly higher V_{OC} compensates for the FF reduction (FF is 76.5 % for 2 sccm and 79.3 % for 0.5 sccm oxygen flow). Finally, our results suggest that the oxygen partial pressures in the range of 0.5 to 2 sccm are an optimum range to satisfy the tradeoff between the FF and the J_{SC}.

5.2.3 Deposition power effect

During the sputtering process, the surface of the substrate is exposed to a bombardment of TCO species [164]. Therefore, the deposition power affects the passivation of the solar cell precursor and also determines the electrical properties of the obtained ZnO:Al layers as the energy of the species affects the material structure and properties.
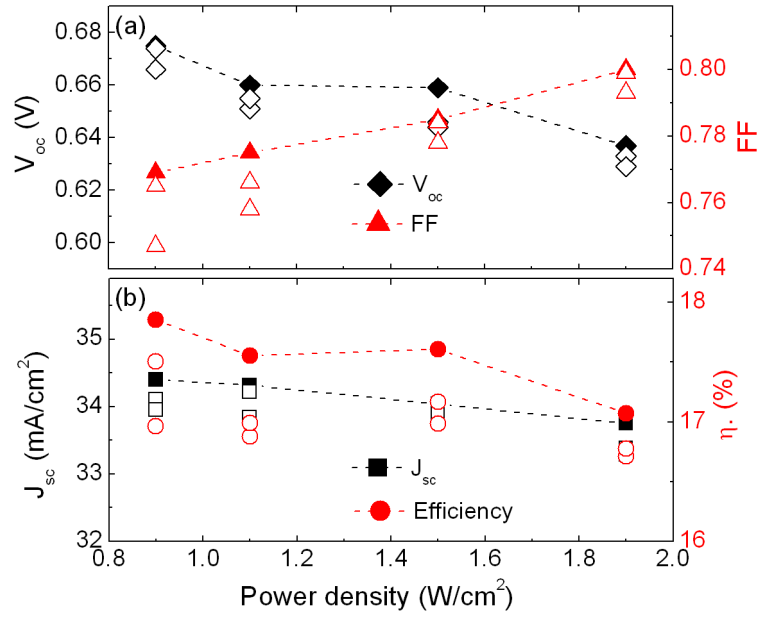
Figure 5.10: *The variation of (a) V_{OC} and FF (b) J_{SC} and η with respect to the deposition power density. The ZnO:Al layers (~320 nm thickness) were deposited at a constant temperature (220 °C) and oxygen flow (0.5 sccm). For each power density, the electrical properties of three cells are demonstrated (fabricated on the same substrate). Filled symbols represent the maximum value. The dashed lines connect the maximum measured values and are plotted to visualize the trend.*

Figure 5.10 (a) illustrates the variation of the V_{OC} and the FF of SHJ solar cells with respect to the deposition power density of the front contact ZnO:Al layers in the range of 0.9-1.9 W/cm^2. Due to the change in the deposition rate with the power density variation, the deposition times were adjusted to obtain a similar layer thickness of ~320 nm for all samples. As demonstrated by figure 5.10 (a), the increase of the sputtering power decreases the V_{OC} values (black diamonds) whereas the FF values (red triangles) increase. The drop in the V_{OC} due to increasing power could be attributed to the increased ion bombardment, as the bombardment adversely affects the wafer passivation [165]. Therefore, the TCO deposition condition should be as soft as possible in order to protect the passivation layers during the sputtering process. It has been shown that post-deposition annealing might recover parts of the degradation due to the ion bombardment during sputtering process [165]. However, this recovery treatment strongly depends on the hydrogen content and the deposition parameters of the passivation layers [78]. Our results show that a gain of ~38 mV is achieved in the V_{OC} when reducing the power density from 1.9 to 0.9 W/cm^2. Zhang *et al* have reported a gain of ~80 mV by using an a-Si:H emitter in the similar power density range [165]. Comparing these two values, it may be stated that the µc-Si:H emitter is more resistant to the ion bombardment process (most probably due to the formation of hydrogen rich sub-layer). However further studies are required.

In addition, figure 5.10 (a) shows that the FF value increases with increased sputtering power (opposite to the V_{OC} trend). This improvement is mainly related to the resistivity reduction of the ZnO:Al layers. Figure 5.11 illustrates that the resistivity of the ZnO:Al layers reduces from 2.5×10^{-3} to 1.97×10^{-3} Ω.cm with increased sputtering power density. Figure 5.11 shows that the reduction in the resistivity is mainly related to the improved mobility (from 13.9 to 15.6 cm^2/Vs) and a slight increase in the carrier concentration. The improved

mobility is attributed to the formation of ZnO:Al layers with larger grains as resulting of the increased species diffusion with the increased power [166].
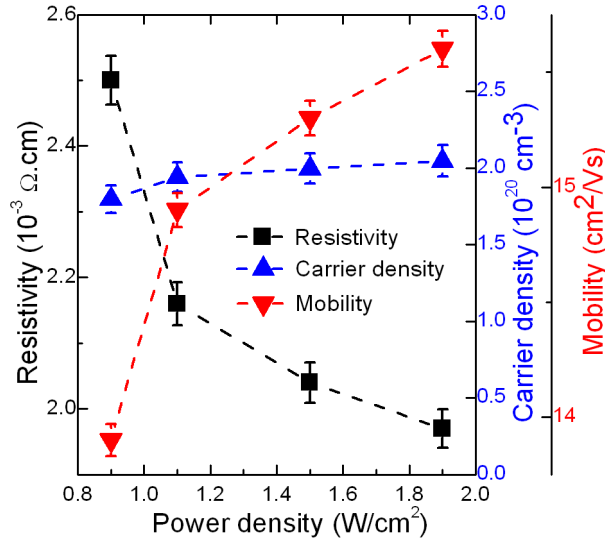
Figure 5.11: *The variation of resistivity, carrier density and mobility with respect to the deposition power density. The ZnO:Al layers (~320 nm) were deposited at a constant temperature (220°C) and oxygen flow (0.5 sccm). The dashed lines are plotted to visualize the trend. The values reported here should be treated as effective values due to the film inhomogeneity.*

Figure 5.10 (b) shows the variation of efficiency with respect to the sputtering power. The maximum efficiency of 17.85 % is achieved for the samples prepared at the lowest sputtering power density of 0.9 W/cm^2. As figure 5.10 suggests, deposition at a lower power is beneficial for the efficiency and the gain in V_{OC} is higher than the loss in the FF. This result indicates that the deposition at a lower sputtering power is more suitable for obtaining a higher efficiency. However, it should be considered that the deposition at a very low power density could cause a highly resistive TCO layer with a higher reduction in the FF than the gain in the V_{OC}.

5.2.4 Deposition temperature effect

The deposition temperature is another important parameter that should be considered for optimizing the ZnO:Al layers since it greatly affects the microstructure of the ZnO:Al layers and its electrical properties. Figure 5.12 shows the resistivity, the carrier concentration and the mobility of the sputtered ZnO:Al layers which have been deposited at various temperatures, ranging from 50 to 300°C and have been fabricated fabricated on the glass substrate in co-deposition with the SHJ solar cells. Figure 5.12 suggests that by increasing the substrate temperature, the resistivity reduces from 3.44×10^{-3} to 1.31×10^{-3} Ω.cm due to the enhanced mobility and the higher carrier concentration. The increase in the mobility can be attributed to the enhanced diffusion of the atoms which results in larger grains [167]. Moreover, higher temperatures favor a higher active Al-content in the ZnO:Al layers what leads to an increased carrier concentration [155].
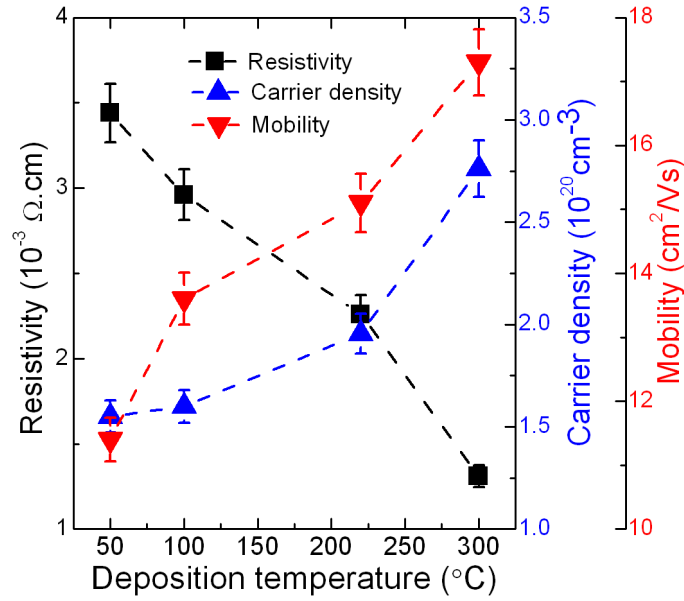
Figure 5.12: *The variation of the resistivity, the carrier density and the mobility with respect to the deposition temperature. The ZnO:Al layers were deposited at a constant power density (1.9 W/cm^2) and oxygen flow (0.5 sccm) in co-deposition with the front TCO of the SHJ solar cells. The dashed lines are plotted to visualize the trend. The values reported here should be treated as effective values due to the film inhomogeneity.*

The variation in the V_{OC}, the FF, the J_{SC}, and the efficiency of the fabricated SHJ solar cells with respect to the deposition temperature of the front contact TCO demonstrated by figure 5.13(a) and (b). As figure 5.13(a) suggests, the FF values (red triangles) improve from 72.7 to 77% at higher deposition temperatures. Almost similar pseudo FF values are obtained for the samples that have been fabricated at various temperatures. The similar pseudo FF values suggest that the main improvement in the FF is mostly due to the reduction in series resistance. Although, it seems that deposition at higher temperatures is an effective way to obtain the desired conductivity of the ZnO:Al layers, it should be considered that, depending on the annealing time (prior to the TCO deposition) and deposition time, some degradation may occur in the passivation.

Figure 5.13 (a) shows the measured V_{OC} of the fabricated SHJ solar cells with respect to the deposition temperature of the ZnO:Al layers. By increasing the temperature from 50 to 100°C, a gain of ~17 mV is obtained in the V_{OC}. This increase can be related to the restructuring of the silicon bonds at the a-Si:H/c-Si interface through diffusion of the hydrogen atoms from the μc-Si:H emitter layer [57,168]. However, at a high temperature regime, a degradation in the passivation could occur [80]. Therefore, the effect of the TCO deposition temperature should be considered for both TCO properties as well as for the solar cell precursor passivation.

Figure 5.13(b) depicts that a deposition at higher temperatures is beneficial for the efficiency due to the improved FF. The maximum efficiency of 17.16 % is obtained for the sample deposited at 300°C. In fact, several studies report a passivation degradation above 240°C deposition temperature for the a-Si:H emitter and BSF layers [57,165,169]. In our work, we have not observed any degradation in the passivation, even at a very high deposition temperature of 300°C. We could attribute this to the highly hydrogen diluted silane plasma that has been used for the fabrication of the μc-Si:H emitter and the BSF layers. As discussed in chapter 4, it is expected that a hydrogen-rich sub layer formsduring the first few seconds of

highly hydrogen diluted silane plasma. During the deposition of the ZnO:Al layer, the hydrogen atoms diffuse most probably to the a-Si:H/c-Si interface which prevents the degradation [84,168]. Therefore, it could be concluded that the deposition of the µc-Si:H emitter and the BSF layers allows to fabricate the ZnO:Al layer at higher temperature than the passivation degradation occurs for an a-Si:H emitter.
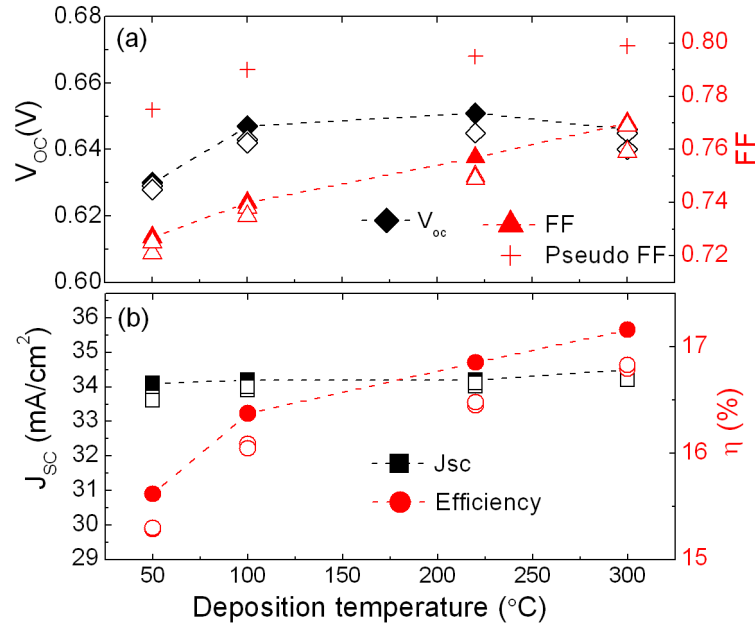
Figure 5.13: *The variation of (a) V_{OC}, FF and pseudo-FF (b) J_{SC} and η with respect to the deposition temperature. The ZnO:Al layers were deposited at a constant power density (1.9 W/cm^2) and oxygen flow (0.5 sccm). The electrical properties of three cells are demonstrated for each deposition temperature, (fabricated on the same substrate). The filled symbols represent the maximum values. The dashed lines connect the maximum measured values and are plotted to visualize the trend.*

5.3 The SHJ solar cells with optimized deposition parameters

In the previous sections (5.2.1- 5.2.4), the effect of each ZnO:Al deposition parameter including thickness, oxygen flow, power and temperature on the electrical properties of the fabricated SHJ solar cells has been studied. In this section, all optimized deposition parameters have been applied in combined with the developed p-type µc-Si:H emitter (chapter 4).

Table 5.1 summarizes all optimized deposition parameters, obtained from section 5.2.1- 5.2.4 where the respective thickness, O$_2$ flow, power density, pressure, temperature and annealing time were 320 nm, 0.5 sccm, 0.75 W/cm^2, 6 µbar, 300°C and 10 min.

Table 5.1: *The optimized ZnO:Al deposition parameters used for the fabrication of the optimized SHJ solar cell.*

Thickness (nm)	O$_2$ flow (sccm)	Power density (W/cm^2)	Pressure (µbar)	Temperature ($^{\circ}$C)	Annealing time (min)
320	0.5	0.75	6	300	10

By applying all optimized deposition parameters (shown in table 5.1) together with the developed p-type μc-Si:H emitter, we obtained SHJ solar cells with a conversion efficiency as high as 19.2%. The electrical properties of the optimized cell are shown in table 5.2. It should be noted that our optimized cell is reproducible.

In fact, the obtained efficiency of 19.2% is among the highest efficiencies for SHJ solar cells with sputtered ZnO:Al layers (on flat c-Si wafer) that have been reported so far. Also, the obtained J_{SC} is one of the highest values achieved on the flat wafer [54]. Therefore, our results demonstrate and confirm the potential of DC sputtered ZnO:Al layers as a promising alternative TCO material for future SHJ solar cells.

Table 5.2: *The electrical properties of the optimized SHJ solar cell, fabricated by using the μc-Si:H emitter in combination with the DC sputtered ZnO:Al TCO on the flat c-Si wafers.*

Designated cell area (cm^2)	J_{SC} (mA/cm^2)	V_{OC} (mV)	FF ($\%$)	η ($\%$)
0.25	34.35	708	79.1	19.2

5.4 ZnO:Al/Ag/ZnO:Al (OMO) structure in SHJ solar cell

In this section, we study the effect of the vertical conductivity component of the ZnO:Al films on the electrical properties of the SHJ solar cells and its influence on the total series resistance. In order to separate the effect of the lateral conduction component from the vertical one, we could take the advantage of embedding a thin metal layer in the ZnO:Al films in the ZnO:Al/Ag/ZnO:Al structure. In general, for the TCO/metal/TCO multilayer structure, it has been demonstrated that the lateral conductivity is only governed by the metal inter-layer, independent on the TCO outer-layers properties [170,171]. Indeed, in the process of the charge carriers collection by the TCO/metal/TCO multilayer structure, only the vertical transportation occurs inside the TCO layers as the lateral one preferably occurs within the metal inter-layer. This unique property of the TCO/metal/TCO multilayer structure allows us to monitor the effect of the vertical conduction component of the TCO layers on the electrical properties of the SHJ solar cells including the total series resistance of the fabricated devices. First we address the opto-electrical properties of the ZnO:Al/Ag/ZnO:Al multilayer structure and compare them with a single ZnO:Al layer. Subsequently, we investigate the role of the vertical conductivity component of the ZnO:Al films on the electrical parameters of SHJ solar cells by fabricating devices with this structure.

It should be noted that the introduced approach to understand the effect of vertical conductivity component of the ZnO:Al films can be applied to other TCOs, as well. This understanding also helps to improve the design of layers where such a one directional transportation takes place as an example in the rear TCO.

5.4.1 ZnO:Al/Ag/ZnO:Al (OMO) properties

Figure 5.14 shows a schematic illustration of the ZnO:Al/Ag/ZnO:Al multilayer structure. The electrical properties of the TCO/metal/TCO multilayer structure can be modeled by parallel resistances. Therefore, the effective resistance (R_{eff}) of the whole structure is expressed as a function of the resistance of single layers parallel coupled [172-174].
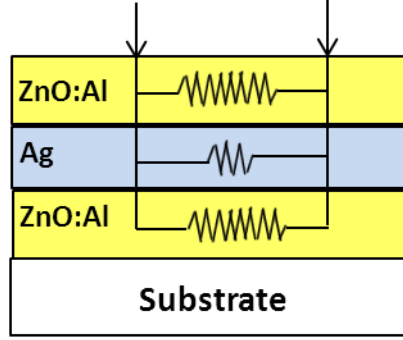
Figure 5.14: *A Schematic illustration of the electrical behavior of the ZnO:Al/Ag/ZnO:Al multilayer structure [173].*

The R_{eff} of the TCO/Metal/TCO can be written via equation 5.2:

$$\frac{1}{R_{eff}} = \frac{1}{R_{TCO,top}} + \frac{1}{R_{Metal}} + \frac{1}{R_{TCO,bot}} = \frac{1}{R_{Metal}} + \frac{2}{R_{TCO}} \tag{5.2}$$

In general, owing to the fact that $R_{TCO} \approx 100R_{Metal}$, the effective resistance is almost equal to the metal resistance ($R_{eff} = 0.98R_{Metal} \approx R_{Metal}$). So, the metal layer is the key element which determines the electrical properties of the TCO/Metal/TCO multilayer structure. Considering the resistivity of various metal elements, Ag is the first choice as it has the lowest resistivity among all metal elements [173].

Figure 5.15 shows the sheet resistance of the ZnO:Al/Ag/ZnO:Al multilayer structure with respect to the Ag inter-layer thickness. The sheet resistance for two single ZnO:Al layers with a thickness of 80 nm (the common ITO thickness for SHJ solar cells [92]) and a thickness of 320 nm (the optimum thickness of ZnO:Al for SHJ solar cells) are illustrated in figure 5.15 as well. It should be noted that the values reported in figure 5.15 should be considered as effective values due to the inhomogeneous films. Figure 5.15 shows that by increasing the Ag inter-layer thickness, the sheet resistance drastically decreases. To investigate the origin of the change in conductivity, we performed Hall measurement. The free carrier density and the charge carrier mobility, as a function of the Ag inter-layer thickness, are plotted in figure 5.15 as well. According to the data, an increase of the Ag inter-layer thickness also increases the free carrier density continuously. The enhanced free carrier density is attributed to the injection of electrons from Ag to the ZnO:Al layers which results in the formation of an accumulation-type contact [170,173]. Due to the increased free carrier density, a red shift in the absorption edge and a narrowing in the optical E_g is observed (figure 5.16). The same phenomenon has been reported for heavily doped ZnO layers where the semiconductor-metal transition takes place [175,176].
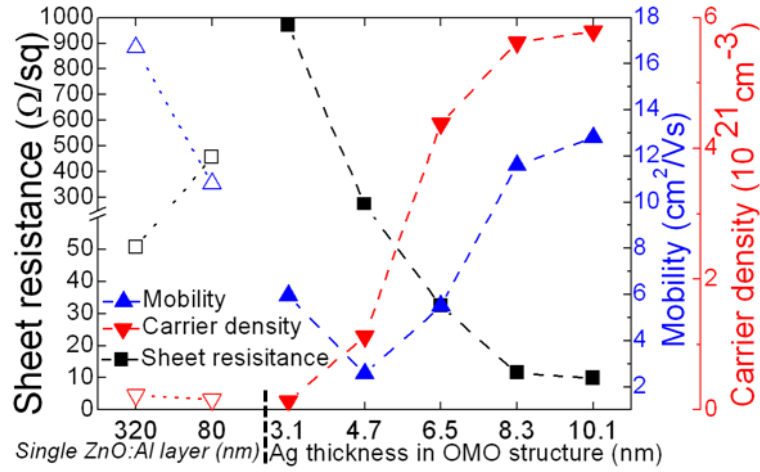
Figure 5.15: *The variation of sheet resistance (filled black squares), mobility (upward blue triangles) and free carrier density (downward red triangles) with respect to the Ag thickness in the ZnO:Al/Ag/ZnO:Al multilayer structure. The corresponding values for the two single ZnO:Al layers (80 and 320 nm layer thicknesses) are illustrated, as well. The dashed lines are plotted to visualize the trend. The values reported here should be treated as effective values due to the inhomogeneous layer stacks.*

In the heavily doped semiconductors, two competing phenomena are dominant in affecting the absorption edge. The first one is the Burstein-Moss band-filling effect which moves the highest occupied levels into the band [177,178]. The second phenomenon is the merged wave function of more closely spaced doping levels with the conduction band edge which results in the E_g shrinkage [175,179,180]. Due to the stronger effect of the second phenomenon (above critical carrier concentration) in degenerated semiconductors, the band edge shifts towards the lower energy levels, by increasing the free carrier density.
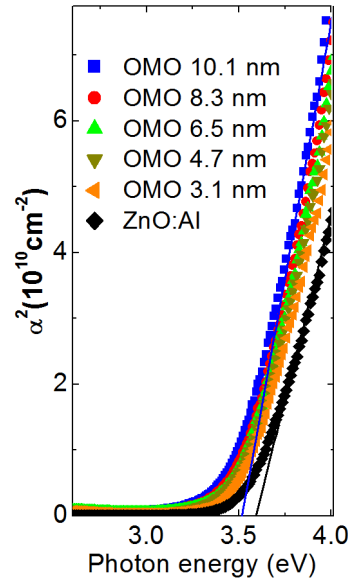
Figure 5.16: *Square of the absorption coefficient (α^2) as a function of the incident photon energy (hv) for the multilayer structure with different Ag inter-layer thicknesses and single ZnO:Al layers. By increasing the thickness of the Ag inter-layer, a red shift can be observed in the absorption edge. The optical $\boldsymbol{E_g}$ energy is extracted by fitting the linear part of the curves through $\alpha^2=A(hv\text{-}\boldsymbol{E_g})$.*

We have used the $\alpha(h\upsilon) = A(h\upsilon - E_g)^{\frac{1}{2}}$ relationship, to determine the optical E_g. Where $h\upsilon$ is the photon energy, α is the absorption coefficient. Subsequently, the optical E_g is deduced from the absorption edge by a linear fit extrapolation of the absorption to zero. As demonstrated by figure 5.16, the obtained E_g of the single ZnO:Al layer is ~3.61 eV and decreases to 3.52 eV for the ZnO:Al/Ag/ZnO:Al multilayer sample with 8.3 nm Ag inter-layer thickness.
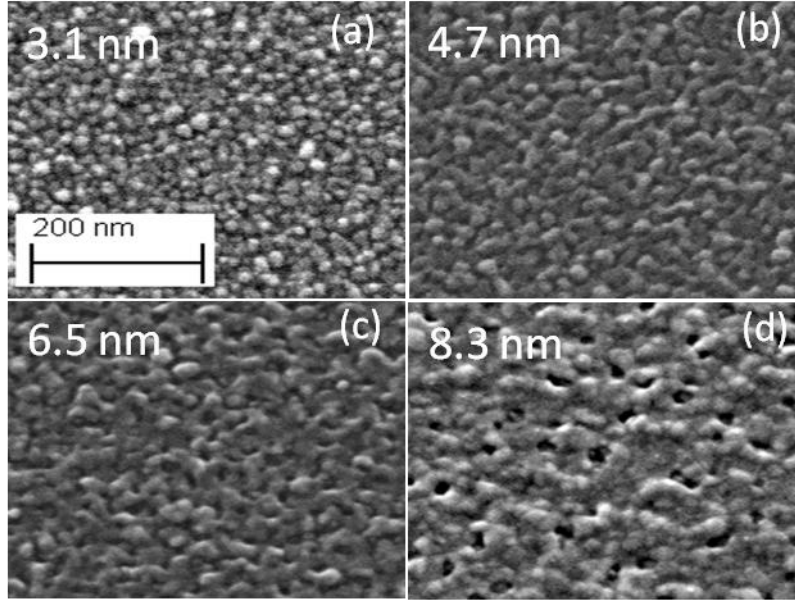
Figure 5.17: *34° tilted SEM micrographs of the ZnO:Al layer surface after the deposition of the Ag film with a thickness of (a) 3.1 nm (b) 4.7 nm (c) 6.5 nm, and (d) 8.3 nm, suggesting the formation of the coalesced Ag layer for a thickness of 8.3 nm.*

For the mobility of the charge carriers, a different trend is observed (compared to the free carrier density). By increasing the Ag interlayer thickness, the mobility decreases first (up to thickness of 4.7 nm) and increases afterwards. Figure 5.17 shows the SEM micrographs of the samples after the deposition of the Ag inter-layer. Indeed, the mobility trend reflects the structural evolution of the Ag inter-layer with the variation in thickness. As figure 5.17 (a) shows Ag metallic nuclei are formed during the initial stage of the Ag growth. By further deposition, the nuclei grow into islands (figure 5.17 (b)), but have not yet coalesced. Due to the increased Ag/ZnO:Al interface resulting from the formation of larger islands (by increasing the Ag thickness from 3.1 to 4.7 nm), the interface scattering increases and thus the mobility decreases from 5.9 to 2.5 cm^2/Vs [170]. By increasing the Ag inter-layer thickness from 4.7 to 6.5, the mobility improves but is still low (5.5 cm^2/Vs), most probably due to the not so well merged islands or still high rough Ag/ZnO:Al interface. Finally, by further increasing the Ag inter-layer thickness to 8.3 nm (figure 5.17 (d)), a significant improvement in the mobility from 5.5 to 11.6 cm^2/Vs is achieved. By further increase in the Ag inter-layer thickness (from 8.3 to 10.1 nm), the mobility and free carrier density increases only slightly.
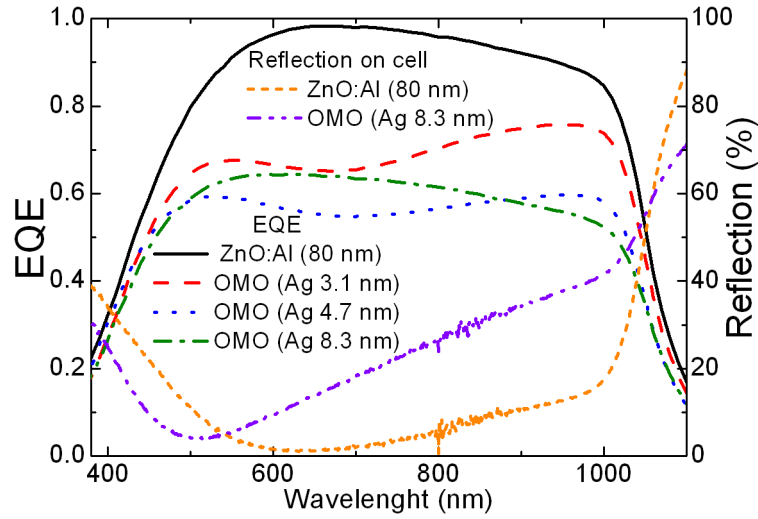
Figure 5.18: *Measured EQE curves of the SHJ solar cells fabricated with 80 nm thick ZnO:Al layer (black solid curve) and with various thicknesses of the Ag inter-layer in the ZnO:Al/Ag/ZnO:Al multilayer structure where by coalesce of the islands into layer, the minima in the EQE curves disappears. The reflection of the SHJ solar cells with 80 nm thick ZnO:Al layer and ZnO:Al/Ag/ZnO:Al multilayer structure with 8.3 nm Ag inter-layer thickness.*

The EQE curves for the SHJ solar cells fabricated with ZnO:Al/Ag/ZnO:Al multilayer structure also indicate the merging of Ag islands and their coalescence into the layer. Figure 5.18 shows the measured EQE curves of the fabricated SHJ solar cells with ZnO:Al/Ag/ZnO:Al multilayers and various Ag inter-layer thicknesses of 3.1, 4.7 and 8.3 nm. There is a minima in the EQE signals of those samples, where the Ag inter-layer film has not coalesced (which could be attributed to the scattering and plasma absorption of the Ag islands [181]). After the coalescence of the Ag islands, the minima in the EQE curves disappears as the continuous Ag layers have a lower absorption [130,181] and hence the absorption of the multilayer structure decreases.

The reflection of the SHJ solar cells with the ZnO:Al single layer (80 nm) and ZnO:Al/Ag/ZnO:Al multilayer structure (with 8.3 nm Ag inter-layer thickness) is plotted in figure 5.18. Due to the higher absorption and the reflection of the ZnO:Al/Ag/ZnO:Al multilayer structure, the EQE values of the SHJ solar cells with such structures have been much lower. As discussed in section 5.1, to develop a new TCO material for the solar cell devices, one aims at improving the mobility instead of the carrier density due to their absorption and reflection (see equation 5.1). The ZnO:Al/Ag/ZnO:Al multilayer structure has a higher carrier density (more than one order of magnitude) compared to the single ZnO:Al layers. Thus, they do not seem to be good candidates (in the current status with planar Ag layer) for solar cell devices whose absorption takes place in the red internal wavelength. The parasitic absorption may be reduced in the blue and green internal wavelengths by optimizing the Al doping concentration in the target. In this case, the ZnO:Al/Ag/ZnO:Al multilayer structure could be used as an alternative for the ITO layer in the a-Si:H single junction and organic solar cells as in these devices the parasitic absorption of free carriers in the red internal wavelength is not an issue. In this regards, Chou *et al* has shown that by structuring a sub-wavelength hole-array, the scattering and transmittance of thin metal layers enhance [182]. It should be noted that the aim of our approach (using ZnO:Al/Ag/ZnO:Al multilayer structure) is to separate the lateral conductivity from the vertical one inside the ZnO:Al layers and the developing of ZnO:Al/Ag/ZnO:Al as TCO is beyond the scope of this study.
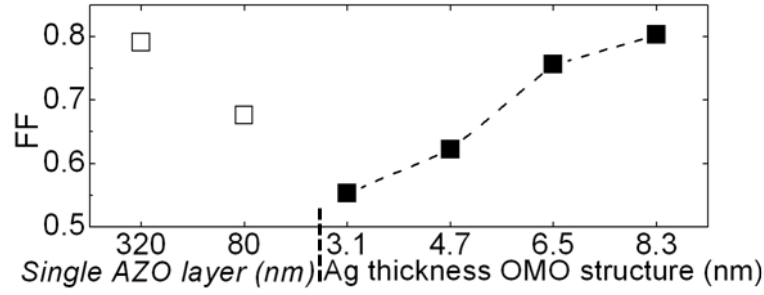
Figure 5.19: *The measured FF (filled black squares) with respect to the Ag inter-layer thickness in the multilayer structure. The FF values (open squares) of the fabricated SHJ solar cells with 80 and 320 nm ZnO:Al layer thicknesses are demonstrated, as well.*

Figure 5.19 shows the FF values of the fabricated SHJ solar cells with a ZnO:Al/Ag/ZnO:Al multilayer structure with respect to the Ag inter-layer thickness. As this graph suggests, by increasing the Ag inter-layer thickness, the FF improves due to the reduced resistivity of the ZnO:Al/Ag/ZnO:Al multilayer structure and hence the reduced series resistance of the fabricated SHJ solar cells. We have obtained a high FF value of 80.3% for the SHJ solar cells with Ag thickness of 8.3 nm. As mentioned before, this thickness corresponds to the sample where the coalescence of Ag islands has taken place. The FF values of the fabricated SHJ solar cells with the single ZnO:Al layers are also demonstrated in figure 5.19, suggesting similar high FF values for the optimized single ZnO:Al layer (320 nm).

5.4.2 Understanding the effect of vertical conductivity component of ZnO:Al

In order to vary the resistivity of the ZnO:Al layers in the ZnO:Al/Ag/ZnO:Al multilayer stack, we have varied the oxygen flow during the sputtering process. Figure 5.20(a) and (b) show the sheet resistance of the ZnO:Al single layers and the ZnO:Al/Ag/ZnO:Al multilayers (with 8.3 nm Ag inter-layer) with respect to the oxygen flow. As discussed in section 5.2.2, the resistivity of the ZnO:Al single layers strongly depends on the oxygen content which increases with the oxygen flow (see figure 5.9 and section 5.2.2).

As shown in figure 5.20 (b), unlike the strong influence of the oxygen flow on the electrical properties of ZnO:Al single layers, the sheet resistance, free carrier density and mobility of the ZnO:Al/Ag/ZnO:Al multilayer structure is independent of the oxygen content of the ZnO:Al outer-layers. We measured an almost constant sheet resistance of ~12.5 Ω/sq, a free carrier density of ~5.4×10^{21} cm^{-3} and a mobility of ~11.5 cm^2/Vs for the investigated oxygen flow range (0.5-6 sccm). This indicates that the electrical properties of the multilayer structure are governed by the Ag inter-layer properties. By employing the multilayer structure in the SHJ solar cell structure, the charge carriers vertically pass through the ZnO:Al outer-layers and only the vertical resistivity component of the ZnO:Al films affects the transportation of the charge carriers (see the effective resistance of the ZnO:Al/Ag/ZnO:Al multilayer structure in equation 5.2). It should be stated that the measured values, shown in figure 5.20, should be considered as effective values due to the inhomogeneous layer stacks.
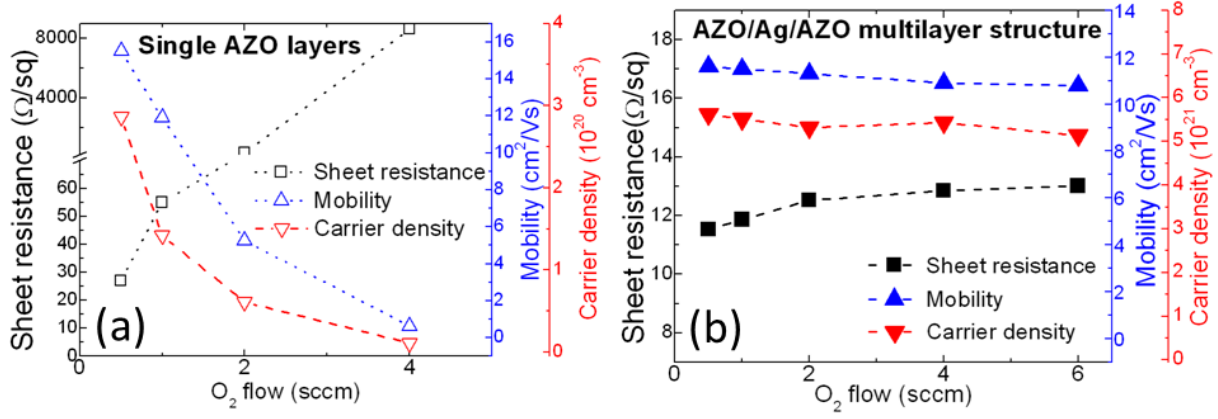
Figure 5.20: *Variation of the sheet resistance (black squares), mobility (upwards triangles) and free carrier density (downwards triangles) with respect to the oxygen flow (a) for the single ZnO:Al layers and (b) for the ZnO:Al/Ag/ZnO:Al multilayer structure. The values reported here should be treated as effective values due to the inhomogeneous layer stacks.*

Figure 5.21 shows the FF values of the SHJ solar cells with single ZnO:Al layers and a ZnO:Al/Ag/ZnO:Al multilayer structure as a function of the oxygen flow. The FF value of the SHJ solar cells with multilayer structure reduces from 0.803 to 0.704 with the increasing oxygen content of the ZnO:Al outer-layers (from 0.5-6 sccm). This reduction results from the increased vertical resistivity component of the ZnO:Al layers. For the SHJ solar cells with single ZnO:Al layers, a significantly higher FF value reduction was measured (open squares in figure 5.21) as both the lateral and the vertical conductivity, affect the charge carrier collection. Figure 5.21 shows the measured pseudo FF values (the FF without the effect of the series resistance) for the SHJ solar cells with a ZnO:Al/Ag/ZnO:Al multilayer structure. We have measured almost the same pseudo FF values of ~0.821 for all samples. This indicates that the reduction of the FF (with an increased oxygen content of the ZnO:Al outer-layers) results from the increased series resistance.
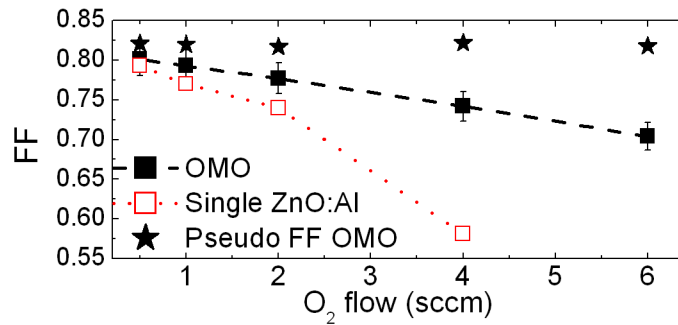
Figure 5.21: *The measured FF of the SHJ solar cells fabricated with the ZnO:Al/Ag/ZnO:Al multilayer structure (filled black squares) and single ZnO:Al layers (open red squares) with respect to the oxygen flow. The measured pseudo FF values of the SHJ solar cells with the ZnO:Al/Ag/ZnO:Al multilayer structure are demonstrated with black filled stars, as well.*

Figure 5.22 demonstrates the measured FF values (black squares) of the fabricated SHJ solar cells with a ZnO:A/Ag/ZnO:Al multilayer structure (for different oxygen flows) as a function of the solar cell series resistance (R_S). The data points for three fabricated SHJ solar cells on the same substrate are demonstrated for each oxygen flow. Indeed the variation of R_S (caused by varying the oxygen flow during sputtering) results from the variation of the vertical resistivity component of the ZnO:Al layers. In other words, figure 5.22 shows the

effect of the vertical resistivity component of the ZnO:Al layers on the FF values of the obtained SHJ solar cells. In figure 5.22, the red line shows a linear fit of the measured data points (black squares). The extrapolated FF_0 value (the FF value with 0 Ω series resistance is shown with green filled circle) of 0.814 from the linear fit (red line) agrees well with the measured pseudo FF values (~0.821). As figure 5.22 suggests, a reduction of ~6% in the FF value per unit increase of vertical resistivity is obtained.
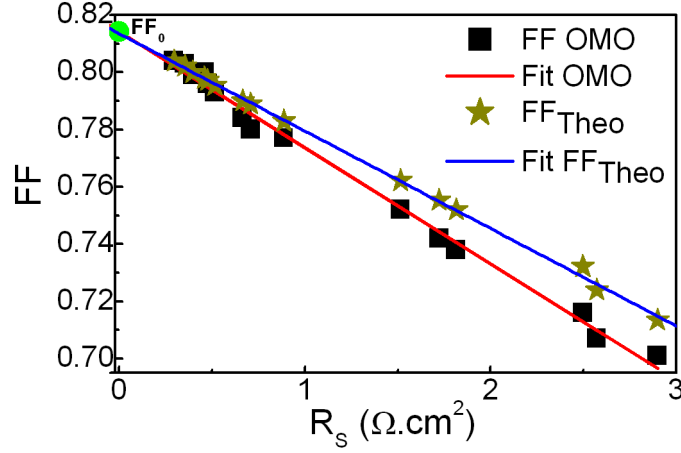
Figure 5.22: *The variation of the measured FF values (square data points) and theoretically calculated FF values (star data points) with respect to the R_S of the fabricated SHJ solar cells with a ZnO:Al/Ag/ZnO:Al multilayer structure for various oxygen flows. The red and blue lines indicate the linear fit of the measured and theoretically calculated data points respectively. A FF_0 as high as 0.814 is obtained by the linear fit extrapolation of the measured data points which is in good agreement with the measured pseudo FF_{pseudo} (0.821) and theoretically calculated $FF_{0\text{-}Theo}$ (0.815) values.*

We have also compared our experimental results with the theoretical model developed by M. A. Green [183]. This model describes the linear relationship of the FF in presence of R_S via:

$$FF = FF_0\left(1 - \frac{R_S}{R_{CH}}\right) \tag{5.3}$$

where the magnitude of the effect of R_S on the FF is found by comparing the values to the characteristic resistance, $R_{CH} = \frac{V_{OC}}{I_{SC}}$ (I_{SC} is short circuit current). In equation 5.3, FF_0 is the ideal FF in absence of the parasitic resistance as closely approximated via:

$$FF_0 = \frac{v_{oc} - \ln(v_{oc} + 0.72)}{v_{oc} + 1} \tag{5.4}$$

where v_{oc} is defined as a normalized voltage via:

$$v_{oc} = \frac{V_{OC}}{n\frac{kT}{q}} \tag{5.5}$$

where n, K, T and q are the ideality factor, the Boltzmann constant, the temperature and the elementary charge, respectively. The semi-empirical limit of $V_{OC} = 700$ mV in equation 5.5 according to Martin Green's formula for J_0 [183] is a useful approximation in the range of E_g as in the c-Si solar cell. From this theoretical relationship, we were able to predict the theoretically calculated FF (FF_{Theo}) values as a function of R_S, as shown in figure 5.22. As can be seen in this figure, the FF_{Theo} values (star data points) are in close proximity with the measured FF values. The difference between the FF_{Theo} and the FF_{OMO} increases with the rise in R_S. This results from the considering a fixed n. An FF_{0_Theo} of 0.815 is obtained by the

linear fit of the FF_{Theo}-R_S data points (blue line) which is well-matched with the measured pseudo FF (0.821) and the FF_0 (0.814) extracted from the linear fit of the measured FF data points (red line). The other parameters, such as the shunt resistance, also affect the FF and need to be considered for a more precise theoretical calculation of the FF [184].

The obtained results indicate that even with the excellent lateral conduction, a hindered vertical transportation of the charge carriers could act as a source of series resistance and reduces the FF values. As the results of this study show, it is possible to almost accurately estimate the change in the FF with change in vertical transportation component of the ZnO:Al layers. A reduction of ~6% in the FF value per unit increase of vertical resistivity was obtained.

5.5 Conclusion on DC sputtered ZnO:Al as an alternative TCO for SHJ solar cells

The TCO plays several important roles in the SHJ solar cell structure such as transferring the collected charge carriers in the emitter into the metal grids and acting as an antireflection coating. In chapter 5, at first, we addressed the importance of the TCO (section 5.1) in the SHJ solar cells. In addition, the disadvantages of the commonly used ITO and the requirement for its replacement were addressed (section 5.1).

Section 5.2 introduced the DC sputtered ZnO:Al as an alternative TCO material. ZnO:Al has two main differences (compared to ITO) including its lower work function (clarified in chapter 4) and its higher resistivity. To address the latter difference, we have investigated the effect of the ZnO:Al deposition parameters including layer thickness, oxygen flow, power density and temperature on the opto-electrical properties of the individual ZnO:Al layers and also the obtained SHJ solar cells.

Our results suggest that since ZnO:Al is a polycrystalline material with the preferred growth direction perpendicular to the substrate, the film thickness has a significant influence on the electrical properties of the ZnO:Al layers and should be considered for layer optimization process. Based on the opto-electrical characterization results, the ZnO:Al optimum thickness should be ~300 nm. Furthermore, our results indicate that by increasing the oxygen partial pressure, the transparency and hence J_{SC} of the obtained SHJ solar cells increase. However, the obtained FF value decreases due to the increased resistivity of the deposited ZnO:Al layers. Therefore, considering a tradeoff between the J_{SC} and the FF, the optimum oxygen partial pressure is found to be ~0.5 sccm. In addition, the effect of the power density in the range of 0.9-1.9 W/cm^2 has been studied and a tradeoff between the FF and the V_{OC} has been observed. Considering the efficiency trend, we found that a deposition at a lower power (~0.9 W/cm^2) is beneficial for the efficiency. Unlike ITO films, the deposition temperature is another important parameter that should be considered for the fabrication of the ZnO:Al layers whose layer conductivity improves at higher deposition temperatures. However, deposition at higher temperatures may degrade the passivation, hence this creates a tradeoff between the FF and the Voc. In the studied temperature range (50-300°C), we did not observe any degradation most likely due to the highly hydrogen diluted silane plasma which was used for fabricating the emitter layers. Section 5.3 summarizes all optimized deposition parameters obtained from the opto-electrical characterization of the individual ZnO:Al layers. Conversion efficiencies as high as 19.2% were obtained by applying all optimized parameters by using a combined μc-Si:H and ZnO:Al layer.

Section 5.4 studied the effect of the vertical conductivity component of the ZnO:Al layers on the electrical properties of the obtained SHJ solar cells and its contribution to the total series resistance. In particular, such one directional transport occurs at the rear TCO, where a TCO layer is inserted to prevent the diffusion of metal atoms into the a-Si:H/c-Si interface and to reduce the plasmonic absorption in the back metal reflector . Therefore, understanding

the effect of the vertical conduction component of ZnO:Al film is important and helps to improve the rear TCO design. To separate the lateral conductivity of the ZnO:Al layers from the vertical component, we fabricated SHJ solar cells by employing ZnO:Al/Ag/ZnO:Al multilayer structures. In such a structure, the vertical transport of charge carriers only takes place inside the ZnO:Al layers since the lateral conduction always occurs inside the Ag layer. Our results show that even with an excellent lateral conduction, a hindered vertical transportation of the charge carriers could act as a source of series resistance which reduces the FF values. A reduction of ~6% in the FF value per unit increase of vertical resistivity is obtained. Furthermore, the obtained experimental trend was verified with the theoretical model developed by Green *et al*.

The results of chapter 5 confirms the potential of DC sputtered ZnO:Al layers with an μc-Si:H emitter for fabricating future SHJ solar cells.

Chapter 6

6 Conclusion and Outlook

The objective of this thesis was to investigate µc-Si:H emitter layers and DC sputtered ZnO:Al TCOs as a novel front contact for SHJ solar cells. The main results and findings of this thesis are summarized as follows:

- Hydrogenated a-Si:H films act as high performance passivation layers, whose passivation quality strongly depends on the PECVD processing parameters. In this thesis, we have investigated the effect of the hydrogen dilution, temperature and power density on the passivation performance of the obtained a-Si:H films. For both polished and unpolished wafers, a hydrogen to silane ratio of 2.5 was found to result in the highest minority carrier lifetimes. At higher hydrogen dilutions, lower lifetime values were measured probably due to the promotion of partial epitaxial growth at the a-Si:H/c-Si interface. Post-deposition annealing significantly improved the lifetime. This improvement depended strongly on the initial passivation quality.

- The effect of the emitter conductivity on the electrical properties of the obtained SHJ solar cells was investigated through a novel approach. We varied the emitter conductivity by taking advantage of an improved conductivity through crystallinity evolution within the µc-Si:H film thickness. This approach allowed us to study the effect of the emitter conductivity without introducing any additional interrelated parameters. Our results show that a highly conductive emitter is extremely necessary to satisfy the required electric field at the emitter/c-Si interface such as to preserve the flat band and to suppress the Schottky barrier at the TCO/emitter interface.

- The implementation of a µc-Si:H emitter layer to satisfy the emitter conductivity requirements has been suggested. (i) Our results indicate that by employing the µc-Si:H layers, (i) the passivation at the a-Si:H/c-Si interface improves, most likely due to the highly hydrogen diluted silane plasma used for the deposition. (ii) Due to the lower absorption coefficient of the µc-Si:H material compared to a-Si:H, parasitic absorption in the emitter is reduced particularly in the blue and green internal wavelength region which in turn results in a gain of ~1.8 mA/cm^2 in J$_{SC}$. (iii) In addition, solar cell precursors can stand higher deposition temperature during ZnO:Al layers fabrication, probably due to the formation of a hydrogen rich sub-layer. The possibility of a higher processing temperature is highly important as the ZnO:Al quality strongly improves at higher temperatures. (iv) Furthermore, our results suggest that, by employing a µc-Si:H emitter layer, the Schottky barrier at the ZnO:Al/emitter junction can effectively be suppressed. Thus, high FF of ~80% can be achieved, as confirmed by our results.

- To successfully utilize the µc-Si:H emitter layers and to keep the emitter absorption as low as possible, a fast nucleation is required. The results suggest that a suitably fast µc-Si:H

nucleation occurs by deposition at low pressures. At these low pressures, the passivation degradation by ion bombardment is reversible and hence it could be used for the emitter deposition, confirmed by the results of this work (chapter 4).

- DC sputtered ZnO:Al as an alternative TCO for SHJ solar cells was investigated. To satisfy the TCO requirements, the effect of the deposition parameters including film (i) thickness, (ii) O_2 partial pressure, (iii) deposition power and (iv) temperature on the opto-electrical properties of the ZnO:Al films and also on SHJ solar cells performance was studied. (i) The results suggest that as the ZnO:Al is a polycrystalline material with preferred growth orientation perpendicular to the substrate, the film thickness is the dominant parameter for satisfying the required lateral conductivity. The main influence of the thickness seems to be its effect on the carrier mobility. We found that a thickness of ~300 nm satisfies the tradeoff between transparency and conductivity for moderate substrate temperatures of 250°C. (ii) Oxygen variation causes the tradeoff between the transparency and conductivity. Our results suggest that the oxygen partial pressure of ~0.5% is the optimum condition. (iii) The deposition power causes a tradeoff between V_{OC} and FF due to defect creation on the one hand and increasing the mobility on the other hand. In this thesis, the optimized deposition power density was found to be ~0.9 W/cm^2 where by this optimization ~40 mV gain in the V_{OC} was achieved. (iv) The deposition at higher temperatures improves both optical and electrical properties of the ZnO:Al layers. Nevertheless, the solar cell precursors should stand the high temperature process during the ZnO:Al layers fabrication step since the hydrogen effusion at the a-Si:H/c-Si interface degrades the passivation. Our results confirm that by fabrication of the µc-Si:H emitter layer, the deposition temperature could be set as high as 300°C. The possibility of this high temperature process is probably due to the formation of a hydrogen rich sub-layer, which possibly forms as a result of hydrogen diffusion into the a-Si:H film within the first few seconds (30 s) of the highly hydrogen diluted silane plasma.

- One of the advantages of the ZnO:Al film is its texturing capability compared to the ITO material. A promising approach for the future of the SHJ solar cells field is the use of thinner wafers to achieve higher V_{OC} values. However, for thinner wafers the light confinement is challenging. Our results show that light trapping can be enhanced by texturing the ZnO:Al films by which a gain of ~1.9 mA/cm^2 in the J_{SC} was achieved after texturing with HF solution.

- The influence of the vertical conductivity component of the ZnO:Al layers on the FF values and its contribution to the total series resistance of the fabricated SHJ solar cells was investigated using ZnO:Al/Ag/ZnO:Al multilayers to separate lateral from vertical conductivity. As the lateral conductivity takes place in the Ag layer, only the vertical transportation of the charge carriers takes place inside the ZnO:Al layers. The results suggest that even with excellent lateral conduction, a hindered vertical transportation of charge carriers could act as a relevant source of series resistance and thus reduces the FF values. A reduction of ~6% in the FF value per unit increase of vertical resistivity was obtained. A good agreement between our obtained experimental results and theoretically calculated values, based on developed theoretical model by M. A. Green concerning the influence of series resistance on the FF, could be shown. From an industrial point of view, understanding the effect of the TCO vertical conductivity component is important since by reducing the wafer thickness, the effect of the rear TCO becomes more significant.

- Finally, by investigating and fine-tuning all the fabrication parameters, a high conversion efficiency of 19.2% (V_{OC}= 0.708 V, FF=0.791, J_{SC}= 34.35 mAcm^{-2}) using ZnO:Al TCO layers on the flat c-Si wafers was obtained. The results of this study show the potential of DC sputtered ZnO:Al layers with an µc-Si:H emitter for replacing the commonly used ITO material for the fabrication of the future generation of SHJ solar cells.

Outlook

This work can be continued in several ways. For this study, we have only used flat c-Si substrates. However, the reflection of a flat c-Si substrate is rather high. Hence, light-trapping approaches have to be applied to reduce the solar cell current losses induced by the reflection. In the case of monocrystalline silicon, a random pyramidal textured surface effectively reduces the reflection as the reflected light has the possibility to refract again. Thus, one of the next steps for this study could be the fabrication of the developed µc-Si:H emitter and ZnO:Al TCO on a textured substrate to further increase the current density. Moreover, as we have shown the texturing capability of the ZnO:Al for light trapping in the SHJ solar cells (section 5.2.1), such light randomization schemes can also be applied on the textured wafer for multi-light trapping in SHJ solar cells.

Recently, the use of thinner wafers has attracted considerable attention due to the lower bulk defect density. However, the use of thinner wafers requires much better light trapping to compensate for the reduced J_{SC}. Hence, the texturing capability of ZnO:Al and the suggested multi-light trapping scheme seems a promising solution to fulfill the abovementioned requirements.

Glossary

A	absorption	%
D	diffusivity	cm^2s^{-1}
D_{it}	surface/interface trap density	cm^{-2}
DB	dangling bond	
E_U	correlation energy	eV
E_V, E_C	valence, conduction band edge	eV
E_i	center of the bandgap	eV
E_t	trap energy level	eV
$E_{F,p\ a\text{-}Si:H}$	p a-Si:H Fermi level	eV
E_{Fn}, E_{Fp}	electron, hole quasi-Fermi level	eV
E_{act}	activation energy	eV
FF	fill factor	%
G	generation rate	$cm^{-3}s^{-1}$
H_{dil}	hydrogen dilution	
I_0	light intensity	$mWcm^{-2}$
JV	current -voltage characteristic	
J_{SC}	short-circuit current density	$mAcm^{-2}$
L_{diff}	diffusion length	cm
N	free carrier density (in TCO)	cm^{-3}
N(E)	density of states	$cm^{-3}eV^{-1}$
N_D, N_A	donor, acceptor density	cm^{-3}
N_S	surface/interface state density	cm^{-2}
N_t	trap density	cm^{-3}
N_{DB}	bulk dangling bond density	cm^{-3}

Q_f	fixed insulator charge density	cm^{-2}
Q_{DB}	interface DB charge density	cm^{-2}
R	reflection	%
R_{bulk}	bulk recombination rate	cm^{-3}s^{-1}
R_{Aug}	Auger recombination rate	cm^{-3}s^{-1}
R_{DB}	dangling bond recombination rate	cm^{-3}s^{-1}
R_{ch}	characteristic resistance	Ω
R_{eff}	effective resistance	Ω
R_s	series resistance	Ω.cm
R_{rad}	radiative recombination rate	cm^{-3}s^{-1}
R_{sq}	sheet resistance	Ω/sq
S	surface recombination velocity	cms^{-1}
SC	silane concentration	%
T	temperature, transmission	
U	interface recombination rate	cm^{-2}s^{-1}
V_{OC}	open-circuit voltage	V
W	wafer thickness	cm
$\Delta E_C, \Delta E_V$	conduction, valence band offset	eV
$\Delta\sigma$	excess photoconductance	Scm^{-1}
$\Delta n, \Delta p$	excess electron, hole density	cm^{-3}
$\Delta n_s, \Delta p_s$	excess surface carrier density	cm^{-3}
$\Delta n_{av}, \Delta p_{av}$	average excess electron, hole density	cm^{-3}
α	absorption coefficient	cm^{-1}
ε_0	vacuum permittivity	AsV^{-1}cm^{-1}
ε_{Si}	relative silicon permittivity	
η	sunlight energy conversion efficiency	%

λ	wavelength	nm
μ	free carrier mobility	$cm^2V^{-1}s^{-1}$
μ_n, μ_p	electron, hole mobility in c-Si	$cm^2V^{-1}s^{-1}$
Φ_L	photon flux density	$cm^{-2}s^{-1}$
Φ_c	Raman crystallinity factor	%
Φ_n, Φ_p	electron, hole quasi-Fermi level	V
ψ_S	surface potential	V
ρ	resistivity	Ωcm
σ	conductivity	Scm^{-1}
σ_n, σ_p	electron, hole capture cross-section	cm^2
σ_n^+, σ_p^-	electron, hole capture cross-section of the charged state	cm^2
σ_n^0, σ_p^0	electron, hole capture cross-section of the neutral state	cm^2
τ_{eff}	effective lifetime	s
τ_{Aug}	Auger lifetime	s
τ_{bulk}	c-Si bulk lifetime	s
τ_{defect}	defect c-Si bulk lifetime	s
τ_{extr}	extrinsic c-Si bulk lifetime	s
τ_{intr}	intrinsic c-Si bulk lifetime	s
τ_{rad}	radiative carrier lifetime	s
μc-Si:H	microcrystalline silicon	
i	intrinsic	
k	Boltzmann constant	
n, p	total electron, hole density	cm^{-3}
n_0, p_0	electron, hole density at thermal equilibrium	cm^{-3}
n_i	intrinsic carrier density	cm^{-3}
n_r	refractive index	

n_s, p_s	surface electron, hole density	cm^{-3}
q	elementary charge	C
$r_n^0, r_p^0, r_n^+, r_p^-$	capture rates of neutral, positively and negatively charged DBs	cm^{-3}s^{-1}
V_{th}	thermal velocity	cm s^{-1}
Ag	silver	
AM	air mass	
a-Si:H	hydrogenated amorphous silicon	
B$_2$H$_6$	Diborane	
BSF	back surface field	
c-Si	crystalline silicon	
CZ	Czochralski	
D^0, D^+, D^-	neutral, positive, negative DB charge condition	
DLTS	deep level transient spectroscopy	
e	electron	
EQE	external quantum efficiency	%
FZ	float zone	
PFF	pseudo fill factor	
h	hole	
HIT	heterojunction with intrinsic thin-layer	
HJ	heterojunction	
HR-TEM	high resolution transmission electron microscopy	
HWCVD	hot wire chemical vapor deposition	
implFF	implied fill factor	%
implV$_{OC}$	implied open-circuit voltage	V
In	indium	

IR	infrared	
IQE	internal quantum efficiency	%
ITO	indium tin oxide	
MIS	metal-insulator-semiconductor	
MPP	maximum power point	
MW-PCD	microwave-detected photoconductance decay	
OMO	oxide/metal/oxide	
PCD	photoconductance decay	
PECVD	plasma enhanced chemical vapor deposition	
PH_3	Phosphine	
PL	photoluminescence	
PV	photovoltaic	
QSSPC	quasi-steady-state photoconductance	
SEM	scanning electron microscope	
Si	silicon	
SiN_x	silicon nitride	
SiO_2	silicon dioxide	
SHJ	silicon heterojunction solar cell	
SRH	Shockley-Read-Hall	
$SunsV_{OC}$	illumination level dependent open-circuit voltage	
TCO	transparent conductive oxide	
TEM	transmission electron microscopy	
XRD	x-ray diffraction	
Zn	zinc	
ZnO:Al	DC sputtered aluminum zinc oxide	

Bibliography

[1]   A. E. Becquerel,   *'Memoire sur les effets electriques produits sous l'inuence des rayons solaires'* Comptes Rendus de lAcademie des Sciences 9, p. 561 (1839).

[2]   D. M. Chapin, C. S. Fuller, and G. L. Pearson,   *'A New Silicon p-n Junction Photocell for Converting Solar Radiation into Electrical Power'* Journal of Applied Physics 25 (5), p. 676 (1954).

[3]   K. Wakisaka, M. Taguchi, T. Sawada, M. Tanaka, T. Matsuyama, T. Matsuoka, S. Tsuda, S. Nakano, Y. Kishi, and Y. Kuwano,   *'More than 16% solar cells with a new HIT (doped a-Si/nondoped a-Si/crystalline Si) structure'* Photovoltaic Specialists Conference 2, p. 887 (1991).

[4]   M. Tanaka, M. Taguchi, T. Matsuyama, T. Sawada, S. Tsuda, S. Nakano, H. Hanafusa, and Y. Kuwano,   *'Development of New a-Si/c-Si Heterojunction Solar Cells: ACJ-HIT (Artificially Constructed Junction-Heterojunction with Intrinsic Thin-Layer)'* Japanese Journal of Applied Physics 31 (Part 1, No. 11), p. 3518 (1992).

[5]   M. Taguchi, A. Terakawa, E. Maruyama, and M. Tanaka,   *'Obtaining a higher Voc in HIT cells'* Progress in Photovoltaics: Research and Applications 13 (6), p. 481 (2005).

[6]   L. Korte and M. Schmidt,   *'Investigation of gap states in phosphorous-doped ultra-thin a-Si:H by near-UV photoelectron spectroscopy'* Journal of Non-Crystalline Solids 354 (19–25), p. 2138 (2008).

[7]   Y. Tsunomura, Y. Yoshimine, M. Taguchi, T. Baba, T. Kinoshita, H. Kanno, H. Sakata, E. Maruyama, and M. Tanaka,   *'Twenty-two percent efficiency HIT solar cell'* Solar Energy Materials and Solar Cells 93 (6-7), p. 670 (2009).

[8]   M. Taguchi, A. Yano, S. Tohoda, K. Matsuyama, Y. Nakamura, T. Nishiwaki, K. Fujita, and E. Maruyama,   *'24.7% Record Efficiency HIT Solar Cell on Thin Silicon Wafer'* Photovoltaics, IEEE Journal of PP (99), p. 1 (2013).

[9]   X. Wen, X. Zeng, W. Liao, Q. Lei, and S. Yin,   *'An approach for improving the carriers transport properties of a-Si:H/c-Si heterojunction solar cells with efficiency of more than 27%'* Solar Energy 96, p. 168 (2013).

[10]   T. Mishima, M. Taguchi, H. Sakata, and E. Maruyama,   *'Development status of high-efficiency HIT solar cells'* Solar Energy Materials and Solar Cells 95 (1), p. 18 (2011).

[11]   M. A. Green,   *'Estimates of te and in prices from direct mining of known ores'* Progress in Photovoltaics: Research and Applications 17 (5), p. 347 (2009).

[12]   M. Omura, A. Tanaka, M. Hirata, N. Inoue, T. Ueno, T. Homma, and K. Sekizawa, *'Testicular Toxicity Evaluation of Indium-Tin Oxide'* Journal of Occupational Health 44 (2), p. 105 (2002).

[13]   H. Fujiwara and J.A. Woollam.,   *'Spectroscopic Ellipsometry: Principles and Applications'* John Wiley & Sons (2007).

[14]   C. R. Wronski, B. Abeles, and G. D. Cody,   *'The influence of carrier generation and collection on short-circuit currents in amorphous silicon solar cells'* Solar Cells 2 (3), p. 245 (1980).

15   M. Vanecek, J. Kocka, J. Stuchlik, and A. Triska, *'Direct measurement of the gap states and band tail absorption by constant photocurrent method in amorphous silicon'* Solid State Communications 39 (11), p. 1199 (1981).

16   A. V. Shah, H. Schade, M. Vanecek, J. Meier, E. Vallat-Sauvain, N. Wyrsch, U. Kroll, C. Droz, and J. Bailat, *'Thin-film silicon solar cell technology'* Progress in Photovoltaics: Research and Applications 12 (2-3), p. 113 (2004).

17   S. Usui and M. Kikuchi, *'Properties of heavily doped GD-Si with low resistivity'* Journal of Non-Crystalline Solids 34 (1), p. 1 (1979).

18   E. Vallat-Sauvain, U. Kroll, J. Meier, A. Shah, and J. Pohl, *'Evolution of the microstructure in microcrystalline silicon prepared by very high frequency glow-discharge using hydrogen dilution'* Journal of Applied Physics 87 (6), p. 3137 (2000).

19   L. Houben, M. Luysberg, P. Hapke, R. Carius, F. Finger, and H. Wagner, *'Structural properties of microcrystalline silicon in the transition from highly crystalline to amorphous growth'* Philosophical Magazine A 77, p. 1447 (1998).

20   C. V. Raman and K. S. Krishnan, *'A New Type of Secondary Radiation'* Nature 121, p. 501 (1928).

21   F. Bechstedt, *'Principles of surface physics'* Springer, Berlin (2003).

22   S. De Wolf, B. Demaurex, A. Descoeudres, and C. Ballif, *'Very fast light-induced degradation of a-Si:H/c-Si(100) interfaces'* Physical Review B 83 (23), p. 233301 (2011).

23   I. Moreno and C. C. Sun, *'Modeling the radiation pattern of LEDs'* Optics Express 16 (3), p. 1808 (2008).

24   G. P. Karman, G. S. McDonald, G. H. C. New, and J. P. Woerdman, *'Laser optics: Fractal modes in unstable resonators'* Nature 402, p. 138 (1999).

25   J. Graeme, *'Photodiode Amplifiers: OP AMP Solutions'* McGraw-Hill, USA (1996).

26   W. G.J.H.M. van Sark, L. Korte, and F. Roca, *'Physics and technology of amorphous-crystalline heterostructure silicon solar cells'* Springer, Berlin (2012).

27   R. A. Sinton, Y. Kwark, J. Y. Gan, and R. M. Swanson, *'27.5-percent silicon concentrator solar cells'* Electron Device Letters, IEEE 7 (10), p. 567 (1986).

28   J. Zhao, A. Wang, and M. A. Green, *'24.5% efficiency PERT silicon solar cells on SEH MCZ substrates and cell performance on other SEH CZ and FZ substrates'* Solar Energy Materials and Solar Cells 66 (1–4), p. 27 (2001).

29   M. Mews, T. F. Schulze, N. Mingirulli, and L. Korte, *'Hydrogen plasma treatments for passivation of amorphous-crystalline silicon-heterojunctions on surfaces promoting epitaxy'* Applied Physics Letters 102 (12), p. 122106 (2013).

30   C. Kittel, *'Introduction to Solid State Physics'* Wiley, New York (2004).

31   S. K. Ghandhi, *'VLSI fabrication principles: Silicon and Gallium Arsenide'* John Wiley & Sons, New York (1982).

32   J. Zhao, A. Wang, M. A. Green, and F. Ferrazza, *'19.8% efficient honeycomb textured multicrystalline and 24.4% monocrystalline silicon solar cells'* Applied Physics Letters 73 (14), p. 1991 (1998).

33   M. A. Green, *'The path to 25% silicon solar cell efficiency: History of silicon cell evolution'* Progress in Photovoltaics: Research and Applications 17 (3), p. 183 (2009).

34   M. A. Green, J. Zhao, A. Wang, P. J. Reece, and M. Gal, *'Efficient silicon light-emitting diodes'* Nature 412, p. 805 (2001).

35   A. G. Aberle and R. Hezel, *'Progress in Low-temperature Surface Passivation of Silicon Solar Cells using Remote-plasma Silicon Nitride'* Progress in Photovoltaics: Research and Applications 5 (1), p. 29 (1997).

36   B. E. Deal and A. S. Grove, *'General Relationship for the Thermal Oxidation of Silicon'* Journal of Applied Physics 36 (12), p. 3770 (1965).

37   W. A. Lanford and M. J. Rand, *'The hydrogen content of plasma‐deposited silicon nitride'* Journal of Applied Physics 49 (4), p. 2473 (1978).

38   Z. Chen, Peyman Sana, J. Salami, and A. Rohatgi, *'A novel and effective PECVD SiO2/SiN antireflection coating for Si solar cells'* Electron Devices, IEEE Transactions on 40 (6), p. 1161 (1993).

39   R. Hezel and K. Jaeger, *'Low Temperature Surface Passivation of Silicon for Solar Cells'* Journal of The Electrochemical Society 136 (2), p. 518 (1989).

40   B. Hoex, S. B. S. Heil, E. Langereis, M. C. M. van de Sanden, and W. M. M. Kessels, *'Ultralow surface recombination of c-Si substrates passivated by plasma-assisted atomic layer deposited Al2O3'* Applied Physics Letters 89 (4), p. 042112 (2006).

41   J. I. Pankove and M. L. Tarng, *'Amorphous silicon as a passivant for crystalline silicon'* Applied Physics Letters 34 (2), p. 156 (1979).

42   W. E. Spear and P. G. Le Comber, *'Substitutional doping of amorphous silicon'* Solid State Communications 17 (9), p. 1193 (1975).

43   M. C. Schubert, J. Isenberg, and W. Warta, *'Spatially resolved lifetime imaging of silicon wafers by measurement of infrared emission'* Journal of Applied Physics 94 (6), p. 4139 (2003).

44   M. Tajima and Y. Okada, *'Characterization of deep levels in LEC GaAs crystals by the photoluminescence technique'* Physica B+C 116 (1–3), p. 404 (1983).

45   C. V. Dodd, C. D. Cox, and W. E. Deeds, *'Experimental Verification of Eddy-Current Flaw Theory'* Plenum Press, New Yourk (1985).

46   R. A. Sinton and A. Cuevas, *'Contactless determination of current–voltage characteristics and minority carrier lifetimes in semiconductors from quasi steady state photoconductance data'* Applied Physics Letters 69 (17), p. 2510 (1996).

47   D. K. Schroder, *'Semiconductor Material and Device Characterization'* John Wiley & Sons, New Jersey (2006).

48   H. Nagel, C. Berge, and A. G. Aberle, *'Generalized analysis of quasi-steady-state and quasi-transient measurements of carrier lifetimes in semiconductors'* Journal of Applied Physics 86 (11), p. 6218 (1999).

49   K.R. McIntosh and R.A. Sinton, *'Uncertainty in Photoconductance Lifetime Measurements that Use an Inductive-Coil Detector'* 23rd European Photovoltaic Solar Energy Conference and Exhibition, Valencia, Spain, p. 77 (2008).

50   S. Olibet, E. Vallat-Sauvain, and C. Ballif, *'Model for a-Si:H/c-Si interface recombination based on the amphoteric nature of silicon dangling bonds'* Physical Review B 76 (3), p. 035326 (2007).

51   S. M. Sze, *'Semiconductor devices, physics and technology'* Wiley, New York (1985).

52   J. G. Simmons and G. W. Taylor, *'Nonequilibrium Steady-State Statistics and Associated Effects for Insulators and Semiconductors Containing an Arbitrary Distribution of Traps'* Physical Review B 4 (2), p. 502 (1971).

53   J. Hubin, A. V. Shah, and E. Sauvain, *'Effects of dangling bonds on the recombination function in amorphous semiconductors'* Philosophical Magazine Letters 66, p. 115 (1992).

54   S. Olibet, *'Properties of interfaces in amorphous/crystalline silicon heterojunctions'* Ph.D. thesis, University of Neuchatel (2009).

55   A. G. Aberle, S. Glunz, and W. Warta, *'Impact of illumination level and oxide parameters on Shockley–Read–Hall recombination at the Si SiO2 interface'* Journal of Applied Physics 71 (9), p. 4422 (1992).

56   J. Schmidt, F. M. Schuurmans, W. C. Sinke, S. W. Glunz, and A. G. Aberle, *'Observation of multiple defect states at silicon–silicon nitride interfaces fabricated by*

low-frequency plasma-enhanced chemical vapor deposition' Applied Physics Letters 71 (2), p. 252 (1997).

57   B. Bahardoust, A. Chutinan, K. Leong, A. B. Gougam, D. Yeghikyan, T. Kosteski, N. P. Kherani, and S. Zukotynski, *'Passivation study of the amorphous–crystalline silicon interface formed using DC saddle-field glow discharge'* physica status solidi (a) 207 (3), p. 539 (2010).

58   M. Schmidt, L. Korte, A. Laades, R. Stangl, Ch Schubert, H. Angermann, E. Conrad, and K. v Maydell, *'Physical aspects of a-Si:H/c-Si hetero-junction solar cells'* Thin Solid Films 515 (19), p. 7475 (2007).

59   Y. J. Song, M. R. Park, E. Guliants, and W. A. Anderson, *'Influence of defects and band offsets on carrier transport mechanisms in amorphous silicon/crystalline silicon heterojunction solar cells'* Solar Energy Materials and Solar Cells 64 (3), p. 225 (2000).

60   Ana Kanevce and Wyatt K. Metzger, *'The role of amorphous silicon and tunneling in heterojunction with intrinsic thin layer (HIT) solar cells'* Journal of Applied Physics 105 (9) (2009).

61   A. G. Aberle, *'Crystalline Silicon Solar cells: Advanced Surface Passivation and Analysis'* Center for Photovoltaic Engineering, University of New South Wales, Sydney (1999).

62   I. Martin, M. Vetter, A. Orpella, J. Puigdollers, A. Cuevas, and R. Alcubilla, *'Surface passivation of p-type crystalline Si by plasma enhanced chemical vapor deposited amorphous SiCx:H films'* Applied Physics Letters 79 (14), p. 2199 (2001).

63   Mark J. Kerr and Andres Cuevas, *'General parameterization of Auger recombination in crystalline silicon'* Journal of Applied Physics 91 (4), p. 2473 (2002).

64   H. Schlangenotto, H. Maeder, and W. Gerlach, *'Temperature dependence of the radiative recombination coefficient in silicon'* physica status solidi (a) 21 (1), p. 357 (1974).

65   A.H. Mahan, B.P. Nelson, S. Salamon, and R.S. Crandall, *'Deposition of Device Quality, Low H Content a-Si:H by the Hot Wire Technique'* Journal of Non-Crystalline Solids 137-138, p. 657 (1991).

66   H. M. Branz, C. W. Teplin, D. L. Young, M. R. Page, E. Iwaniczko, L. Roybal, R. Bauer, A. H. Mahan, Y. Xu, P. Stradins, T. Wang, and Q. Wang, *'Recent advances in hot-wire CVD R&D at NREL: From 18% silicon heterojunction cells to silicon epitaxy at glass-compatible temperatures'* Thin Solid Films 516 (5), p. 743 (2008).

67   R. A. Street, *'Hydrogen chemical potential and structure of a-Si:H'* Physical Review B 43 (3), p. 2454 (1991).

68   A. Descoeudres, L. Barraud, R. Bartlome, G. Choong, S. De Wolf, F. Zicarelli, and C. Ballif, *'The silane depletion fraction as an indicator for the amorphous/crystalline silicon interface passivation quality'* Applied Physics Letters 97 (18), p. 183505 (2010).

69   R.A. Sinton and D. Macdonald, (2006).

70   S. De Wolf and M. Kondo, *'Abruptness of a-Si:H/c-Si interface revealed by carrier lifetime measurements'* Applied Physics Letters 90 (4), p. 042111 (2007).

71   T. F. Schulze, H. N. Beushausen, C. Leendertz, A. Dobrich, B. Rech, and L. Korte, *'Interplay of amorphous silicon disorder and hydrogen content with interface defects in amorphous/crystalline silicon heterojunctions'* Applied Physics Letters 96 (25), p. 252102 (2010).

72   K. Nomoto, Y. Urano, J. L. Guizot, G. Ganguly, and A. Matsuda, *'Role of Hydrogen Atoms in the Formation Process of Hydrogenated Microcrystalline Silicon'* Japanese Journal of Applied Physics 29 (Part 2, No. 8), p. L1372 (1990).

73   Yanfa Yan, M. Page, T. H. Wang, M. M. Al-Jassim, Howard M. Branz, and Qi Wang, *'Atomic structure and electronic properties of c-Si/a-Si:H heterointerfaces'* Applied Physics Letters 88 (12), p. 121925 (2006).

74   Hiroyuki Fujiwara and Michio Kondo, *'Impact of epitaxial growth at the heterointerface of a-Si:H/c-Si solar cells'* Applied Physics Letters 90 (1), p. 013503 (2007).

75   T. H. Wang, E. Iwaniczko, M. R. Page, D. H. Levi, Y. Yan, H. M. Branz, and Q. Wang, *'Effect of emitter deposition temperature on surface passivation in hot-wire chemical vapor deposited silicon heterojunction solar cells'* Thin Solid Films 501 (1-2), p. 284 (2006).

76   M. Jeon, S. Yoshiba, and K. Kamisako, *'Hydrogenated amorphous silicon film as intrinsic passivation layer deposited at various temperatures using RF remote-PECVD technique'* Current Applied Physics 10 (2), p. S237 (2010).

77   H. C. Neitzert, W. Hirsch, and M. Kunst, *'Structural changes of a-Si:H films on crystalline silicon substrates during deposition'* Physical Review B 47 (7), p. 4080 (1993).

78   O. Madani Ghahfarokhi, K. von Maydell, and C. Agert, *'Study of Surface Passivation of CZ c-Si by PECVD a-Si:H Films; A Comparison Between Quasi-Steady-State and Transient Photoconductance Decay Measurement'* in Proceedings of MRS Spring meeting, San Francisco 1536 (2013).

79   W. Wanlu and L. Kejun, *'Studies of some properties of mechanical stress in a-Si:H, a-SiNx:H and a-Si:H/a-SiNx:H heterojunction films'* Thin Solid Films 165 (1), p. 173 (1988).

80   M. Z. Burrows, U. K. Das, R. L. Opila, S. De Wolf, and R. W. Birkmire, *'Role of hydrogen bonding environment in a-Si:H films for c-Si surface passivation'* Journal of Vacuum Science & Technology A 26 (4), p. 683 (2008).

81   Akihisa Matsuda, Madoka Takai, Tomonori Nishimoto, and Michio Kondo, *'Control of plasma chemistry for preparing highly stabilized amorphous silicon at high growth rate'* Solar Energy Materials and Solar Cells 78 (1-4), p. 3 (2003).

82   D. K. Biegelsen, R. A. Street, C. C. Tsai, and J. C. Knights, *'Hydrogen evolution and defect creation in amorphous Si: H alloys'* Physical Review B 20 (12), p. 4839 (1979).

83   C.S. Liu, C.Y. Wu, I.W. Chen, and L.S. Hong, *'High Rate Deposition of a-Si:H Thin Layers for n-Type c-Si Surface Passivation'* 26th European Photovoltaic Solar Energy Conference and Exhibition, Hamburg, Germany, p. 2198 (2011).

84   A. Descoeudres, L. Barraud, Stefaan De Wolf, B. Strahm, D. Lachenal, C. Guerin, Z. C. Holman, F. Zicarelli, B. Demaurex, J. Seif, J. Holovsky, and C. Ballif, *'Improved amorphous/crystalline silicon interface passivation by hydrogen plasma treatment'* Applied Physics Letters 99 (12), p. 123506 (2011).

85   C. Leendertz, R. Stangl, T. F. Schulze, M. Schmidt, and L. Korte, *'A recombination model for a-Si:H/c-Si heterostructures'* physica status solidi (c) 7 (3-4), p. 1005 (2010).

86   R. Meaudre and M. Meaudre, *'Method for the determination of the capture cross sections of electrons from space-charge-limited conduction in the dark and under illumination in amorphous semiconductors'* Applied Physics Letters 85 (2), p. 245 (2004).

87   S. W. Glunz, D. Biro, S. Rein, and W. Warta, *'Field-effect passivation of the SiO2Si interface'* Journal of Applied Physics 86 (1), p. 683 (1999).

88   D. Macdonald and L. J. Geerligs, *'Recombination activity of interstitial iron and other transition metal point defects in p- and n-type crystalline silicon'* Applied Physics Letters 85 (18), p. 4061 (2004).

89   J. Schmidt and A. Cuevas, *'Electronic properties of light-induced recombination centers in boron-doped Czochralski silicon'* Journal of Applied Physics 86 (6), p. 3175 (1999).

90   J. Lagowski, P. Edelman, A. M. Kontkiewicz, O. Milic, W. Henley, M. Dexter, L. Jastrzebski, and A. M. Hoff, *'Iron detection in the part per quadrillion range in silicon using surface photovoltage and photodissociation of iron-boron pairs'* Applied Physics Letters 63 (22), p. 3043 (1993).

91   L. Korte and M. Schmidt, *'Doping type and thickness dependence of band offsets at the amorphous/crystalline silicon heterojunction'* Journal of Applied Physics 109 (6), p. 063714 (2011).

92   Stefean De Wolf, Antoine Descoeudres, C. Holman Zachary, and Christophe Ballif, *'High-efficiency Silicon Heterojunction Solar Cells: A Review'* Green 2, p. 7 (2012).

93   Z. C. Holman, A. Descoeudres, L. Barraud, F. Z. Fernandez, J. P. Seif, S. De Wolf, and C. Ballif, *'Current Losses at the Front of Silicon Heterojunction Solar Cells'* IEEE Journal of Photovoltaics 2 (1), p. 7 (2012).

94   D.E. Kane and R.M. Swanson., *'Measurement of the emitter saturation current by a contactless photoconductivity decay method.'* 18th IEEE Photovoltaic Specialists Conference, Las Vegas, USA, p. 578 (1985).

95   C. Leendertz, N. Mingirulli, T. F. Schulze, J. P. Kleider, B. Rech, and L. Korte, *'Discerning passivation mechanisms at a-Si:H/c-Si interfaces by means of photoconductance measurements'* Applied Physics Letters 98 (20), p. 202108 (2011).

96   M. W. M. van Cleef, R. E. I. Schropp, and F. A. Rubinelli, *'Significance of tunneling in p-amorphous silicon carbide n-crystalline silicon heterojunction solar cells'* Applied Physics Letters 73 (18), p. 2609 (1998).

97   R. Varache, J. P. Kleider, M. E. Gueunier-Farret, and L. Korte, *'Silicon heterojunction solar cells: Optimization of emitter and contact properties from analytical calculation and numerical simulation'* Materials Science and Engineering: B 178 (9), p. 593 (2013).

98   O. Sergeev, T. Bienert, C. Feser, K. Grunewald, A. Neumuller, R. E. Nowak, K. Kellermann, J. Surig-Morieng, K. von Maydell, and C. Agert, *'Post-Deposition Optimisation of LPCVD-Grown ZnO:B as Front TCO in Silicon Thin-Film Solar Cells'* 27th European Photovoltaic Solar Energy Conference Exhibition, Frankfurt, Germany, p. 2148 (2012).

99   I. Santos, P. Castrillo, W. Windl, D. A. Drabold, L. Pelaz, and L. A. Marques, *'Self-trapping in B-doped amorphous Si: Intrinsic origin of low acceptor efficiency'* Physical Review B 81 (3), p. 033203 (2010).

100   S. Mirabella, D. De Salvador, E. Napolitani, E. Bruno, and F. Priolo, *'Mechanisms of boron diffusion in silicon and germanium'* Journal of Applied Physics 113 (3), p. 031101 (2013).

101   R. E. Hollingsworth and P. K. Bhat, *'Doped microcrystalline silicon growth by high frequency plasmas'* Applied Physics Letters 64 (5), p. 616 (1994).

102   Z. Wu, J. Sun, Q. Lei, Y. Zhao, X. Geng, and J. Xi, *'Analysis on pressure dependence of microcrystalline silicon by optical emission spectroscopy'* Physica E: Low-dimensional Systems and Nanostructures 33 (1), p. 125 (2006).

103   A. V. Shah, J. Meier, E. Vallat-Sauvain, N. Wyrsch, U. Kroll, C. Droz, and U. Graf, *'Material and solar cell research in microcrystalline silicon'* Solar Energy Materials and Solar Cells 78 (1–4), p. 469 (2003).

104   S. Klein, T. Repmann, and T. Brammer, *'Microcrystalline silicon films and solar cells deposited by PECVD and HWCVD'* Solar Energy 77 (6), p. 893 (2004).

105 O. Madani Ghahfarokhi, P. Klement, T. Kilper, K. von Maydell, and C. Agert, *'Deposition of Hydrogenated Microcrystalline Silicone at the Edge of Overcoming Hydrogen Etching and the Role of Hydrogen Atoms in the Growth'* in Proceedings of the 27th European Photovoltaic Solar Energy Conference and Exhibition, Frankfurt, Germany, p. 2570 (2012).

106 K. Winz, B. Rech, T. H. Eickhoff, C. Beneking, C. M. Fortmann, P. Hapke, and H. Wagner, *'Optoelectronic Properties of Thin Amorphous and Micro-Crystalline p-Type Films Developed for Amorphous Silicon-Based Solar Cells'* MRS Online Proceedings Library 420 (1996).

107 P. Chang, F. Tsai, C. Lu, C. Yeh, N. Wang, and M. Houng, *'Improvement of AZO/p-a-SiC:H contact by the p-μc-Si:H insertion layer and its application to a-Si:H solar cells'* Solid-State Electronics 72, p. 48 (2012).

108 F. Claeyssens, C. L. Freeman, N. L. Allan, Y. Sun, M. N. R. Ashfold, and J. H. Harding, *'Growth of ZnO thin films-experiment and theory'* Journal of Materials Chemistry 15 (1), p. 139 (2005).

109 U. Kroll, J. Meier, A. Shah, S. Mikhailov, and J. Weber, *'Hydrogen in amorphous and microcrystalline silicon films prepared by hydrogen dilution'* Journal of Applied Physics 80 (9), p. 4971 (1996).

110 J. K. Rath, L. A. Klerk, A. Gordijn, and R. E. I. Schropp, *'Mechanism of hydrogen interaction with the growing silicon film'* Solar Energy Materials and Solar Cells 90 (18-19), p. 3385 (2006).

111 F. Kail, A. Fontcuberta I Morral, A. Hadjadj, P. Roca I Cabarrocas, and A. Beorchia, *'Hydrogen-plasma etching of hydrogenated amorphous silicon: a study by a combination of spectroscopic ellipsometry and trap-limited diffusion model'* Philosophical Magazine 84 (6), p. 595 (2004).

112 J. Geissbuhler, S. De Wolf, B. Demaurex, J. P. Seif, D. T. L. Alexander, L. Barraud, and C. Ballif, *'Amorphous/crystalline silicon interface defects induced by hydrogen plasma treatments'* Applied Physics Letters 102 (23), p. 231604 (2013).

113 A. Klein, C. Korber, A. Wachau, F. Sauberlich, Y. Gassenbauer, S. P. Harvey, D. E. Proffit, and T. O. Mason, *'Transparent Conducting Oxides for Photovoltaics: Manipulation of Fermi Level, Work Function and Energy Band Alignment'* Materials 3 (11), p. 4892 (2010).

114 K. Itoh, H. Matsumoto, T. Kobata, A. Fujishima, O. Nakamura, and K. Fukui, *'Determining height of a leaky Schottky barrier existing in the junction between SnO2 and a highly doped p-type amorphous SiC by using the pulsed laser-induced transient photopotential technique'* Applied Physics Letters 51 (21), p. 1685 (1987).

115 M. Bivour, C. Reichel, M. Hermle, and S. W. Glunz, *'Improving the a-Si:H(p) rear emitter contact of n-type silicon solar cells'* Solar Energy Materials and Solar Cells 106 (0), p. 11 (2012).

116 M. Rahmouni, A. Datta, P. Chatterjee, J. Damon-Lacoste, C. Ballif, and P. Roca i Cabarrocas, *'Carrier transport and sensitivity issues in heterojunction with intrinsic thin layer solar cells on N-type crystalline silicon: A computer simulation study'* Journal of Applied Physics 107 (5), p. 054521 (2010).

117 E. Centurioni and D. Iencinella, *'Role of front contact work function on amorphous silicon/crystalline silicon heterojunction solar cell performance'* IEEE Electron Device Letters 24 (3), p. 177 (2003).

118 Tadatsugu Minami, Toshihiro Miyata, and Takashi Yamamoto, *'Work function of transparent conducting multicomponent oxide thin films prepared by magnetron sputtering'* Surface and Coatings Technology 108-109, p. 583 (1998).

[119] Hideharu Matsuura, Tetsuhiro Okuno, Hideyo Okushi, and Kazunobu Tanaka, *'Electrical properties of n-amorphous/p-crystalline silicon heterojunctions'* Journal of Applied Physics 55 (4), p. 1012 (1984).

[120] F. J. Haug, R. Biron, G. Kratzer, F. Leresche, J. Besuchet, C. Ballif, M. Dissel, S. Kretschmer, W. Soppe, P. Lippens, and K. Leitner, *'Improvement of the open circuit voltage by modifying the transparent indium–tin oxide front electrode in amorphous n–i–p solar cells'* Progress in Photovoltaics: Research and Applications 20 (6), p. 727 (2011).

[121] I. Ohdomari and K. N. Tu, *'Parallel silicide contacts'* Journal of Applied Physics 51 (7), p. 3735 (1980).

[122] M. H. Vishkasougheh and B. Tunaboylu, *'Simulation of high efficiency silicon solar cells with a hetero-junction microcrystalline intrinsic thin layer'* The III. International Conference on Nuclear and Renewable Energy Resources NuRER 2012, p. 141 (2012).

[123] R. A. Sinton and A. Cuevas, *'A quasi-steady-state open-circuit voltage method for solar cell characterization'* in: Proceedings of the 16th European Photovoltaic Solar Energy Conference and Exhibition, Glasgow, Scotland, p. 1152 (2000).

[124] S. W. Glunz, J. Nekarda, H. Mackel, and A. Cuevas, *'Analyzing back contacts of silicon solar cells by Suns-Voc-measurement at high illumination densities'* in Proceedings of 22nd European Photovoltaic Solar Energy Conference and Exhibition, Milan, Italy, p. 849 (2007).

[125] O. Madani Ghahfarokhi, K. Chakanga, K. Von Maydell, and C. Agert, *'DC sputtered ZnO:Al as transparent conductive oxide for heterojunction solar cells with µc-Si:H emitter'* Submitted to Progress in Photovoltaics: Research and Applications

[126] T. F. Schulze, L. Korte, F. Ruske, and B. Rech, *'Band lineup in amorphous/crystalline silicon heterojunctions and the impact of hydrogen microstructure and topological disorder'* Physical Review B 83 (16), p. 165314 (2011).

[127] K. Ellmer and R. Mientus, *'Carrier transport in polycrystalline transparent conductive oxides: A comparative study of zinc oxide and indium oxide'* Thin Solid Films 516 (14), p. 4620 (2008).

[128] V. A. Dao, H. Choi, J. Heo, H. Park, K. Yoon, Y. Lee, Y. Kim, N. Lakshminarayan, and J. Yi, *'rf-Magnetron sputtered ITO thin films for improved heterojunction solar cell applications'* Current Applied Physics 10 (3, Supplement), p. S506 (2010).

[129] T. Koida, H. Sai, and M. Kondo, *'Application of hydrogen-doped In2O3 transparent conductive oxide to thin-film microcrystalline Si solar cells'* Thin Solid Films 518 (11), p. 2930 (2010).

[130] I. Hamberg and C. G. Granqvist, *'Evaporated Sn-doped In[sub 2]O[sub 3] films: Basic optical properties and applications to energy-efficient windows'* Journal of Applied Physics 60 (11), p. R123 (1986).

[131] T. Koida, H. Fujiwara, and M. Kondo, *'Reduction of Optical Loss in Hydrogenated Amorphous Silicon/Crystalline Silicon Heterojunction Solar Cells by High-Mobility Hydrogen-Doped In2O3 Transparent Conductive Oxide'* Applied Physics Express 1 (4), p. 041501 (2008).

[132] A. Kanevce and W. K. Metzger, *'The role of amorphous silicon and tunneling in heterojunction with intrinsic thin layer (HIT) solar cells'* Journal of Applied Physics 105 (9) (2009).

[133] A. Salomon, G. Courtois, C. Charpentier, M. Labrune, P. Prod'Homme, L. Francke, and P. Roca i Cabarrocas, *'Effect of annealing on silicon heterojunction solar cells with textured ZnO:Al as transparent conductive oxide'* EPJ Photovolt. 3, p. 35002 (2012).

134 J. Hupkes, B. Rech, O. Kluth, T. Repmann, B. Zwaygardt, J. Müller, R. Drese, and M. Wuttig, *'Surface textured MF-sputtered ZnO films for microcrystalline silicon-based thin-film solar cells'* Solar Energy Materials and Solar Cells 90 (18-19), p. 3054 (2006).

135 H. Zhu, J. Hupkes, E. Bunte, J. Owen, and S. M. Huang, *'Novel etching method on high rate ZnO:Al thin films reactively sputtered from dual tube metallic targets for silicon-based solar cells'* Solar Energy Materials and Solar Cells 95 (3), p. 964 (2011).

136 C. Charpentier, P. Prodhomme, I. Maurin, M. Chaigneau, and P. Roca i Cabarrocas, *'X-Ray diffraction and Raman spectroscopy for a better understanding of ZnO:Al growth process'* EPJ Photovolt. 2, p. 25002 (2011).

137 Y. R. Ryu, W. J. Kim, and H. W. White, *'Fabrication of homostructural ZnO p-n junctions'* Journal of Crystal Growth 219 (4), p. 419 (2000).

138 L. Korte, E. Conrad, H. Angermann, R. Stangl, and M. Schmidt, *'Advances in a-Si:H/c-Si heterojunction solar cell fabrication and characterization'* Solar Energy Materials and Solar Cells 93 (6-7), p. 905 (2009).

139 L. Korte, E. Conrad, H. Angermann, R. Stangl, and M. Schmidt, *'Overview on a Si H c Si heterojunction solar cells physics and technology'* 22nd European Photovoltaic Solar Energy Conference, Milan, Italy, p. 859 (2007).

140 A. Favier, D. Munoz, S. Martin de Nicolas, and P. J. Ribeyron, *'Boron-doped zinc oxide layers grown by metal-organic CVD for silicon heterojunction solar cells applications'* Solar Energy Materials and Solar Cells 95 (4), p. 1057 (2011).

141 G. Choong, P. Bole, L. Barraud, F. Zicarelli, A. Descoeudres, S. De Wolf, and C. Ballif, *'TRANSPARENT CONDUCTIVE OXIDES FOR SILICON HETEROJUNCTION SOLAR CELLS'* 25th European Photovoltaic Solar Energy Conference and Exhibition, Valencia, Spain, p. 2505 (2010).

142 F. Ruske, C. Jacobs, V. Sittinger, B. Szyszka, and W. Werner, *'Large area ZnO:Al films with tailored light scattering properties for photovoltaic applications'* Thin Solid Films 515 (24), p. 8695 (2007).

143 B. Y. Oh, M. C. Jeong, T. H. Moon, W. Lee, J. M. Myoung, J. Y. Hwang, and D. S. Seo, *'Transparent conductive Al-doped ZnO films for liquid crystal displays'* Journal of Applied Physics 99 (12), p. 124505 (2006).

144 H. Angermann, E. Conrad, L. Korte, J. Rappich, T. F. Schulze, and M. Schmidt, *'Passivation of textured substrates for a-Si:H/c-Si hetero-junction solar cells: Effect of wet-chemical smoothing and intrinsic a-Si:H interlayer'* Materials Science and Engineering: B 159-160 (0), p. 219 (2009).

145 J. M. Myoung, W. H. Yoon, D. H. Lee, I. Yun, S. H. Bae, and S. Y. Lee, *'Effects of Thickness Variation on Properties of ZnO Thin Films Grown by Pulsed Laser Deposition'* Japanese Journal of Applied Physics 41, p. 28 (2002).

146 T. L. Yang, D. H. Zhang, J. Ma, H. L. Ma, and Y. Chen, *'Transparent conducting ZnO:Al films deposited on organic substrates deposited by r.f. magnetron-sputtering'* Thin Solid Films 326 (1-2), p. 60 (1998).

147 S. S. Lin, J. L. Huang, and P. Sajgalik, *'Effects of substrate temperature on the properties of heavily Al-doped ZnO films by simultaneous r.f. and d.c. magnetron sputtering'* Surface and Coatings Technology 190 (1), p. 39 (2005).

148 M. V. Ponomarev, K. Sharma, M. A. Verheijen, M. C. M. van de Sanden, and M. Creatore, *'Improved conductivity of aluminum-doped ZnO: The effect of hydrogen diffusion from a hydrogenated amorphous silicon capping layer'* Journal of Applied Physics 111 (6), p. 063715 (2012).

149 P. Campbell and M. A. Green, *'Light trapping properties of pyramidally textured surfaces'* Journal of Applied Physics 62 (1), p. 243 (1987).

[150] E. Yablonovitch and G. D. Cody, *'Intensity enhancement in textured optical sheets for solar cells'* Electron Devices, IEEE Transactions on 29 (2), p. 300 (1982).

[151] E. Yablonovitch, *'Statistical ray optics'* Journal of the Optical Society of America 72 (7), p. 899 (1982).

[152] A. Janotti and C. G. Van de Walle, *'Oxygen vacancies in ZnO'* Applied Physics Letters 87 (12), p. 122102 (2005).

[153] Rafael Jaramillo and Shriram Ramanathan, *'Kelvin force microscopy studies of work function of transparent conducting ZnO:Al electrodes synthesized under varying oxygen pressures'* Solar Energy Materials and Solar Cells 95 (2), p. 602 (2011).

[154] Y. Hu, Y. Q. Chen, Y. C. Wu, M. J. Wang, G. J. Fang, C. Q. He, and S. J. Wang, *'Structural, defect and optical properties of ZnO films grown under various O2/Ar gas ratios'* Applied Surface Science 255 (22), p. 9279 (2009).

[155] B. Szyszka, *'Transparent and conductive aluminum doped zinc oxide films prepared by mid-frequency reactive magnetron sputtering'* Thin Solid Films 351 (1-2), p. 164 (1999).

[156] J. F. Scott, *'UV Resonant Raman Scattering in ZnO'* Physical Review B 2 (4), p. 1209 (1970).

[157] R. Hong, H. Qi, J. Huang, H. He, Z. Fan, and J. Shao, *'Influence of oxygen partial pressure on the structure and photoluminescence of direct current reactive magnetron sputtering ZnO thin films'* Thin Solid Films 473 (1), p. 58 (2005).

[158] k. Ellmer, *'Magnetron sputtering of transparent conductive zinc oxide: relation between the sputtering parameters and the electronic properties'* Journal of Physics D: Applied Physics 33 (4), p. R17 (2000).

[159] K. Ellmer, F. Kudella, R. Mientus, R. Schieck, and S. Fiechter, *'Influence of discharge parameters on the layer properties of reactive magnetron sputtered ZnO:Al films'* Thin Solid Films 247 (1), p. 15 (1994).

[160] H. Zhu, J. Hüpkes, E. Bunte, and S. M. Huang, *'Oxygen influence on sputtered high rate ZnO:Al films from dual rotatable ceramic targets'* Applied Surface Science 256 (14), p. 4601 (2010).

[161] K. Tominaga, K. Kuroda, and O. Tada, *'Radiation Effect due to Energetic Oxygen Atoms on Conductive Al-Doped ZnO Films'* Japanese Journal of Applied Physics 27, p. 1176 (1988).

[162] Richard L. Petritz, *'Theory of Photoconductivity in Semiconductor Films'* Physical Review 104 (6), p. 1508 (1956).

[163] H. Zhu, J. Hupkes, E. Bunte, and S. M. Huang, *'Oxygen influence on sputtered high rate ZnO:Al films from dual rotatable ceramic targets'* Applied Surface Science 256 (14), p. 4601 (2010).

[164] B. Demaurex, S. De Wolf, A. Descoeudres, Z. C. Holman, and C. Ballif, *'Damage at hydrogenated amorphous/crystalline silicon interfaces by indium tin oxide overlayer sputtering'* Applied Physics Letters 101 (17), p. 171604 (2012).

[165] D. Zhang, A. Tavakoliyaraki, Y. Wu, R. A. C. M. M. van Swaaij, and M. Zeman, *'Influence of ITO deposition and post annealing on HIT solar cell structures'* Energy Procedia 8, p. 207 (2011).

[166] S. Y. Kuo, K. C. Liu, F. I. Lai, J. F. Yang, W. C. Chen, M. Y. Hsieh, H. I. Lin, and W. T. Lin, *'Effects of RF power on the structural, optical and electrical properties of Al-doped zinc oxide films'* Microelectronics Reliability 50 (5), p. 730 (2010).

[167] T. Minami, H. Sato, H. Imamoto, and S. Takata, *'Substrate Temperature Dependence of Transparent Conducting Al-Doped ZnO Thin Films Prepared by Magnetron Sputtering'* Japanese Journal of Applied Physics 31 (Part 2, No. 3A), p. L257 (1991).

[168] O. Madani Ghahfarokhi, K Von Maydell, and C. Agert, *'Enhanced passivation at amorphous/crystalline silicon interface and suppressed Schottky barrier by deposition of microcrystalline silicon emitter layer in siliconheterojunction solar cells'* Applied Physics Letters 104 (11), p. 113901 (2014).

[169] M. S. Jeon and K. Kamisako, *'Hydrogenated Amorphous Silicon Thin Films as Passivation Layers Deposited by Microwave Remote-PECVD for Heterojunction Solar Cells '* Transactions on electrical and electronic materials 10 (3), p. 75 (2009).

[170] H. Han, N. D. Theodore, and T. L. Alford, *'Improved conductivity and mechanism of carrier transport in zinc oxide with embedded silver layer'* Journal of Applied Physics 103 (1), p. 013708 (2008).

[171] D. R. Sahu, Shin-Yuan Lin, and Jow-Lay Huang, *'ZnO/Ag/ZnO multilayer films for the application of a very low resistance transparent electrode'* Applied Surface Science 252 (20), p. 7509 (2006).

[172] I. Crupi, S. Boscarino, V. Strano, S. Mirabella, F. Simone, and A. Terrasi, *'Optimization of ZnO:Al/Ag/ZnO:Al structures for ultra-thin high-performance transparent conductive electrodes'* Thin Solid Films 520 (13), p. 4432 (2012).

[173] C. Guillen and J. Herrero, *'TCO/metal/TCO structures for energy and flexible electronics'* Thin Solid Films 520 (1), p. 1 (2011).

[174] E. J. J. Martin, M. Yan, M. Lane, J. Ireland, C. R. Kannewurf, and R. P. H. Chang, *'Properties of multilayer transparent conducting oxide films'* Thin Solid Films 461 (2), p. 309 (2004).

[175] A. P. Roth, J. B. Webb, and D. F. Williams, *'Band-gap narrowing in heavily defect-doped ZnO'* Physical Review B 25 (12), p. 7836 (1982).

[176] H. Han, J. W. Mayer, and T. L. Alford, *'Band gap shift in the indium-tin-oxide films on polyethylene napthalate after thermal annealing in air'* Journal of Applied Physics 100 (8), p. 083715 (2006).

[177] E. Burstein, *'Anomalous Optical Absorption Limit in InSb'* Physical Review 93 (3), p. 632 (1954).

[178] T. S. Moss, *'The Interpretation of the Properties of Indium Antimonide'* Proceedings of the Physical Society. Section B 67 (10), p. 775 (1954).

[179] K. J. Kim and Y. R. Park, *'Large and abrupt optical band gap variation in In-doped ZnO'* Applied Physics Letters 78 (4), p. 475 (2001).

[180] B. E. Sernelius, K. F. Berggren, Z. C. Jin, I. Hamberg, and C. G. Granqvist, *'Band-gap tailoring of ZnO by means of heavy Al doping'* Physical Review B 37 (17), p. 10244 (1988).

[181] S. H. Mohamed, *'Effects of Ag layer and ZnO top layer thicknesses on the physical properties of ZnO/Ag/Zno multilayer system'* Journal of Physics and Chemistry of Solids 69 (10), p. 2378 (2008).

[182] S. Y. Chou and W. Ding, *'Ultrathin, high-efficiency, broad-band, omni-acceptance, organic solar cells enhanced by plasmonic cavity with subwavelength hole array'* Optics Express 21 (S1), p. A60 (2013).

[183] M. A. Green, *'Solar cells: Operating principles, technology, and system applications'* University of New South Wales, Prentice-Hall, Englewood Cliffs, New Jersey (1982).

[184] S. Y. Lee, H. Choi, H. Li, K. Ji, S. Nam, J. Choi, S. W. Ahn, H. M. Lee, and B. Park, *'Analysis of a-Si:H/TCO contact resistance for the Si heterojunction back-contact solar cell'* Solar Energy Materials and Solar Cells, p. 412 (2013).

Acknowledgments

First of all, I wish to express my sincere gratitude to the promoters of my PhD Prof. Carsten Agert and Dr. Karsten von Maydell.

I would like to thank Prof. Carsten Agert for giving me the opportunity to join Next-Energy Company and work on this exciting topic. I would like to thank you for all the scientific inputs and proofreading my manuscripts and my PhD thesis. You have always been a source of energy and enthusiasm for me.

I am deeply grateful to my supervisor Dr. Karsten von Maydell. I appreciate all the fruitful discussions we had together which has always been inspiring me. I would like to thank you for the time you spent to proofread my thesis and manuscripts and for all the valuable suggestions and scientific discussions.

I would like to thank Prof. Jürgen Parisi for co-supervising my work and the productive meetings we had together.

I gratefully acknowledge Dr. Lars Korte for fruitful discussions and excellent complementary inputs on my PhD project. I would like to thank you for reading this work and your valuable comments and suggestions.

Furthermore, I would like to thank Oleg Sergeev, Jens Suerig-Morieng, Martin Kellermann, Hartmut Koesters, Thomas Faasch and Tim Glaser for their assistance regarding the technical maintenance support.

I would like to thank my office mates: Martin Theuring and Alex Neumueller, and my colleagues: Kambulakwao Chakanga, Ortwin Siepmann, Stefan Geissendoerfer, Clemens Feser, Benedikt Hanke, Martin Vehse, Cordula Walder, Thilo Kilper, Peter Klement, Volker Steenhoff, Regina Nowak, Nies Reininghaus, Gabriele Janson, Tim Moeller, Ulf Kirstein and Pramod Rajanna.

Last but certainly not the least, my deepest gratitude goes to my family. I would like to thank my family: my father Homayoun, my mother Maryam and my sister Arezou. I am grateful for your endless support, understanding and encouragement for all the years of my studies. Furthermore, I wish to express my appreciation to my extended family for their understanding and encouragement.

Finally and most importantly, my heartfelt thanks go to my lovely fiancé Sepideh whose love and patience has always motivated me and made it possible to accomplish this work. I do not know how to thank her for her unconditional support.

Omid Madani Ghahfarokhi

Oldenburg, 21 Feb 2014

List of publications

O. Madani Ghahfarokhi, K. von Maydell and C. Agert, **"**Enhanced passivation at amorphous/crystalline silicon interface and suppressed Schottky barrier by deposition of microcrystalline silicon emitter layer in silicon heterojunction solar cells**",** Appl. Phys. Lett. 104, 113901 (2014).

O. Madani Ghahfarokhi, P. Mulbagal Rajanna, O. Sergeev, K. von Maydell and C. Agert, "Effect of the vertical transportation component of the TCO layer on the electrical properties of silicon heterojunction solar cells", IEEE J. Photovoltaics 4, (2014).

O. Madani Ghahfarokhi, K. Chakanga, O. Sergeev, K. von Maydell and C. Agert, **"**Investigation of AZO as transparent conductive oxide for heterojunction solar cells**",** 28th EU-PVSEC, pp. 1928-1931 (2013).

O. Madani Ghahfarokhi, K. Chakanga, K. von Maydell and C. Agert, **"**DC sputtered ZnO:Al as transparent conductive oxide for heterojunction solar cells with μc-Si:H emitter**"**, Submitted to Prog. Photovolt. Res. Appl.

O. Madani Ghahfarokhi, K. von Maydell and C. Agert, "Study of surface passivation of CZ c-Si by PECVD a-Si:H Films; a comparison between quasi-steady-state and transient photoconductance decay measurement", MRS 1536, pp. 187-192 (2013).

O. Madani Ghahfarokhi, P. Klement, T. Kilper, K. von Maydell and C. Agert, "Deposition of hydrogenated microcrystalline silicon at the edge of overcoming hydrogen etching and the role of hydrogen atoms in the growth", 27th EU-PVSEC, pp. 2570-2572 (2012).

Other papers not included in this thesis:

M. Python, O. Madani, D. Dominé, F. Meillaud, E. Vallat-Sauvain and C. Ballif, "Influence of the substrate geometrical parameters on microcrystalline silicon growth for thin film solar cells", Sol. Energy Mater. Sol. Cells 93, pp. 1714-1720 (2009).

A.V. Shah, F. Sculati-Meillaud, Z.J. Berényi, O.M. Ghahfarokhi and R. Kumar, "Diagnostics of thin-film silicon solar cells and solar panels/modules with variable intensity measurements (VIM)", Sol. Energy Mater. Sol. Cells 95, pp. 398-403 (2011).

Curriculum vitae

Biography

Omid Madani Ghahfarokhi

17th May 1983 , Tehran, Iran

Education

M.Sc. in Micro- and Nanotechnology

IMT, University of Neuchâtel, Switzerland, Sep. 2007-Dec. 2008

Master thesis: Development of large area sun simulator for thin film PV modules

B.S. in Electrical Engineering-Electronic

Department of Electrical and Computer Engineering, Zanjan State University, Zanjan, Iran, Sep. 2001-Jun. 2006

Bachelor thesis: Study of power, control system and detective instruments in cement factories

Work Experience

Research assistant: Developing new TCO and emitter for silicon heterojunction solar cells / EWE Research Center for Energy Technology (Next-Energy), Oldenburg, Germany / Feb. 2011-present

Research assistant: Synthesis and classification of different hydrogenated amorphous silicon materials in various deposition conditions to obtain more stable single and multi-junction amorphous silicon solar cells / PV-LAB, Ecole Polytechnique Federale de Lausanne (EPFL) Neuchatel, Switzerland / Mar. 2009-Dec. 2009

Research assistant: Development of surface diffusion for the 3D modeling of microcrystalline silicon growth / PV-LAB, IMT, University of Neuchatel, Switzerland / Jan. 2008-Jun. 2008

Project engineer: Programming simatic S7 PLC / Member of installation and commissioning group, Padena Semirom Co., Tehran/Saveh, Iran / Jul. 2006-Jul. 2007

Erklärung

Hiermit bestätige ich, dass ich die vorliegende Arbeit selbstständig verfasst und keine anderen als die angegebenen Quellen und Hilfsmittel verwendet habe.

Oldenburg,

Omid Madani Ghahfarokhi